

CHARACTERIZATION OF IN VITRO EPILEPTIFORM ACTIVITY AND PROPAGATION
IN THE IN UTERO IRRADIATED RAT MODEL

By

JOHN NICHOLAS GRIMES

A DISSERTATION PRESENTED TO THE GRADUATE SCHOOL
OF THE UNIVERSITY OF FLORIDA IN PARTIAL FULFILLMENT
OF THE REQUIREMENTS FOR THE DEGREE OF
DOCTOR OF PHILOSOPHY

UNIVERSITY OF FLORIDA

2011

© 2011 John Nicholas Grimes

To my parents, Tom and LeVinuia Grimes

ACKNOWLEDGMENTS

I would like to take a moment to give special thanks to the people and entities that have provided the support necessary for this work to come to fruition. I thank Dr. Tom DeMarse, my committee chair for his inspiration and advice. I thank the other members on my committee, Dr. Benjamin Keselowsky, Dr. Bill Ogle, and Dr. Eric Laywell for their feedback and guidance. I thank Dr. Huan-Xin Chen and Dr. Steven Roper for providing the tissue on which these experiments were performed. I thank Dr. Roman Garnett for his insights and help with various statistical tests. I give thanks to the J. Crayton Pruitt Family and the University of Florida Alumni Foundation and for their generosity, which has enabled me to pursue my graduate studies.

I would also like to thank my close friends and family. I give special thanks to Pam Anderson who has motivated and given support during this difficult time. Finally, I give my greatest thanks to my loving parents: my dad, Tom, and my mom, LeViniua, who passed away unexpectedly before this work was completed.

TABLE OF CONTENTS

	<u>page</u>
ACKNOWLEDGMENTS.....	4
LIST OF TABLES.....	8
LIST OF FIGURES.....	10
LIST OF ABBREVIATIONS.....	13
ABSTRACT.....	15
CHAPTER	
1 INTRODUCTION AND BACKGROUND.....	17
Introduction.....	17
Causes of Epilepsy.....	18
Cortex Anatomy and Physiology.....	18
Cortical Dysplasia and Epilepsy.....	20
Models of Epilepsy.....	21
Animal selection.....	22
Epilepsy induction protocols.....	23
Animal models of cortical dysplasia.....	23
The <i>in utero</i> irradiated rat model of cortical dysplasia.....	25
<i>in vitro</i> Techniques.....	29
Whole-cell patch recording.....	29
Optical imaging with voltage and calcium sensitive dyes.....	30
Microelectrode arrays.....	31
Previous Work and Literature Review.....	32
Normally Laminated Slices.....	33
Salient anatomical structures and physiological properties.....	33
Initiation of epileptiform events.....	36
Propagation of epileptiform activity.....	38
Event termination.....	43
<i>In Utero</i> Irradiated Induced Dysplastic Slices.....	45
<i>In vivo</i> EEG.....	45
<i>In vitro</i> epileptiform waveforms.....	47
Neuron distributions.....	48
Functional differences of neurons in radiation induced dysplastic cortex...	49
Objectives and Central Hypothesis.....	51

2	EXPERIMENT AND METRICS.....	54
	Experimental Protocol.....	54
	Animals and Irradiation Protocol.....	54
	Brain Slice Preparation.....	54
	Recording.....	56
	Post Processing and Data Analysis.....	56
	Definition of Metrics	57
	Verification of Slice Stationarity	58
	Classical and Non-Spatial Metrics	61
	Ictal events per recording time	61
	Average event length	62
	Distribution of event lengths.....	62
	Average burst integral.....	62
	Average inter-event interval	63
	Distribution of inter-event intervals.....	63
	Recovery ratio	64
	Number of local field potentials per epileptic event.....	64
	Spatial Metrics.....	64
	Initiation site.....	65
	Ictal wave propagation speeds and pattern	65
	Termination site	66
	New Metrics.....	66
	Overview of Granger Causality	66
	Pairwise Granger Causality.....	67
	Conditional Granger Causality	71
3	VERIFICATION OF SLICE STABILITY.....	78
	Control Slice Stability.....	78
	Low Dose Slice Stability.....	80
	High Dose Slice Stability.....	81
	Stability Conclusions.....	82
4	CLASSICAL AND SPATIAL RESULTS AND ANALYSIS	98
	Results of Classical Analysis Techniques.....	98
	Ictal Events per Recording Time	98
	Average Event Length.....	99
	Distribution of Event Lengths.....	99
	Average Inter-Event-Interval.....	101
	Distribution of Inter-Event Intervals	101
	Recovery Ratio.....	103
	Number of Field Potentials per Epileptic Event	104
	Summary of Classical Analysis	105
	Results of Spatial Analysis Techniques	106

Initiation Site.....	106
Propagation.....	107
Wave speed.....	108
Propagation pattern.....	109
Termination Site.....	110
Summary of Spatial Metrics.....	112
5 GRANGER CAUSALITY RESULTS AND ANALYSIS.....	131
Results From Pairwise Granger Causality Analysis.....	131
Analysis Methods.....	131
PWGC Mean Values and Distributions.....	132
Mean PWGC Values by Cell Layer.....	133
PWGC Changes Over Time.....	136
Initiation Site vs. PWGC Source Focus.....	137
Results From Conditional Granger Causality Analysis.....	138
Analysis Methods.....	138
CGC Mean Values and Distributions.....	139
Mean CGC Values by Cell Layer.....	140
CGC Changes Over Time.....	141
Initiation Site vs. CGC Source Focus.....	142
Summary of Granger Causality Analysis.....	143
6 CONCLUSIONS.....	154
Conclusions.....	154
Future Work.....	155
LIST OF REFERENCES.....	157
BIOGRAPHICAL SKETCH.....	174

LIST OF TABLES

<u>Table</u>	<u>page</u>
4-1 Ictal duration mean, standard deviation, and 95% confidence interval	113
4-2 Inter-event interval mean, standard deviation, and 95% confidence interval....	113
4-3 Recovery ratio mean and standard deviation	113
4-4 Positive extrema rate mean and standard deviation	113
4-5 Negative extrema rate mean and standard deviation	113
4-6 Total extrema rate mean and standard deviation	113
4-7 Results of two-sample t-tests on measured extrema rate means	114
4-8 Mean horizontal and vertical wave speeds through tissue	114
4-9 Results of two-sample Kolmogorov-Smirnov tests on wave propagation speeds between groups	114
4-10 Mean horizontal propagation speed through cell layers	114
4-11 Results of intra-group two-sample Kolmogorov-Smirnov tests on horizontal wave propagation speeds between cell layers	114
4-12 Results of inter-group two-sample Kolmogorov-Smirnov tests on horizontal wave propagation speeds between cell layers	115
5-1 Mean pairwise Granger Causality values of each group	144
5-2 Results of two-sample Kolmogorov-Smirnov tests on pairwise Granger Causality distributions between groups	144
5-3 Mean PWGC in each cell layer	144
5-4 Results of two-sample Kolmogorov-Smirnov tests on pairwise Granger Causality distributions between cell layers	144
5-5 Mean conditional Granger Causality values of each group	145
5-6 Results of two-sample Kolmogorov-Smirnov tests on conditional Granger Causality values between groups	145
5-7 Mean CGC in each cell layer	145

5-8 Results of two-sample Kolmogorov-Smirnov tests on conditional Granger
Causality values between cell layers 145

LIST OF FIGURES

<u>Figure</u>	<u>page</u>
1-1 Data collected in the DeMarse lab from acute rat cortical slices treated with 4-AP (140 μ M) and KCl (7.5 mM) using 60-channel 3D MEAs.....	52
1-2 An acute rat hippocampal slice with CA1 and the dentate gyrus placed over the electrodes of an Ayanda Biosystems MEA60 200 3D.	53
2-1 Visual representation of the automated post-processing algorithm. Here four seconds from one channel of raw data in which an ictal event occurred is plotted.....	74
2-2 Concentration of solutes in the recording chamber vs. time.	75
2-3 Example of an erroneous direct causal connection generated by Pairwise Granger Causality on a network in which a mediated connection exists.	76
2-4 Example of erroneously increasing connection weights generated by PWGC in which a series of mediated connections exists	77
3-1 Ictal event number vs. ictal event start time for a normally laminated slice used to verify activity stability.	84
3-2 Control slice demonstrating three linear phases.....	85
3-3 Ictal event duration vs. ictal event number. Data are from the same recording used to generate Figure 3-2, which appeared to have three distinct activity phases	86
3-4 Ictal event duration vs. ictal event start time, verifying epileptiform activity was stable over the course of the recording period.....	87
3-5 Ictal event duration vs. ictal event number for the same normally laminated slice data used in Figure 3-1.....	88
3-6 Ictal event duration vs. ictal event start time number for the same normally laminated slice data used in Figure 3-1 and Figure 3-5.....	89
3-7 Plot of ictal event number vs. ictal event start time for a control slice subject illustrating stair-step pattern.	90
3-8 Ictal event durations vs. ictal event number for a control subject. Data used are the same used to generate Figure 3-7.	91
3-9 Ictal event duration vs. ictal event start time for a control subject. Data are from the same subject used to generate Figure 3-7 and Figure 3-8	92

3-10	Plot of ictal event number vs. ictal event start time for a low dose irradiated subject illustrating characteristic pronounced stair-step pattern.	93
3-11	Ictal event durations vs. ictal event number for a low dose irradiated subject. Data used are the same used to generate Figure 3-10.	94
3-12	Ictal event duration vs. ictal event start time for a low dose irradiated subject. Data are from the same subject used to generate Figure 3-10 and Figure 3-11.	95
3-13	Characteristic stability plots for the high dose subject exhibiting a simple linear trend.....	96
3-14	Characteristic stability plots for high dose subject exhibiting the stair-step trend.	97
4-1	Histograms of event duration normalized by number of events. For readability, events over 10 s in length have been omitted.	116
4-2	Log-normal fits of the event durations for each group.	117
4-3	Histograms of inter-event intervals normalized by number of event intervals. For readability, intervals over 50 s in length have been omitted.....	118
4-4	Exponential fit of the inter-event intervals for each group.....	119
4-5	Recovery scatter plots. The recovery scatter plot is a plot of inter-event intervals vs. time.....	120
4-6	Histograms of recovery ratio for subjects. Recovery ratios larger than 20 were omitted for visual readability.	121
4-7	Histograms of positive extrema rates in control, low dose, and high dose groups.	122
4-8	Histograms of negative extrema rates in control, low dose, and high dose groups.	123
4-9	Histograms of all extrema rates in control, low dose, and high dose groups. ...	124
4-10	Normal fits of the positive, negative, and total extrema rates for each group. ...	125
4-11	Analysis plots for a control subject displaying a strongly dominant initiation focus.....	126
4-12	Analysis plots for a control subject without a dominant initiation focus.....	127
4-13	Wave propagation analysis plots.....	128

4-14	Analysis plots for a control subject displaying a dominant termination focus....	129
4-15	Analysis plots for a control subject displaying diffuse termination locations.	130
5-1	Probability density estimates of pairwise Granger Causality values by group. .	146
5-2	Probability density estimates of pairwise Granger source and sink values among groups by cell layer.....	147
5-3	Comparison between initiation focus and PWGC source.	148
5-4	PWGC driving region over time.	149
5-5	Probability density estimates of conditional Granger Causality values by group.	150
5-6	CGC Source and Sink values by layer.	151
5-7	Comparison between initiation focus and CGC source.	152
5-8	CGC driving region over time.	153

LIST OF ABBREVIATIONS

4-AP	4-aminopyridine
µm	micrometer
ACSF	Artificial Cerebrospinal Fluid
AED	Antiepileptic Drugs
AR	Autoregressive
BMI	bicuculline methiodide
CCD	charged coupled device
CD	Cortical Dysplasia
CGC	Conditional Granger Causality
cGy	centigray
DNA	Deoxyribonucleic acid
E#	Embryonic Day #
EEG	Electroencephalogram
EPSC	Excitatory Post Synaptic Current
EPSP	Excitatory Post Synaptic Potential
GABA	gamma-aminobutyric acid
GC	Granger Causality
IB	Intrinsically Bursting neuron
IBI	Inter-Burst Interval or Inter-Event Interval
IGER	Ihara's Genetically Epileptic Rat
IPSC	Inhibitory Post Synaptic Current
IPSP	Inhibitory Post Synaptic Potential
LFP	Local Field Potential
MAM	methylazoxymethanol

MCD	Malformations of Cortical Development
MEA	Micro- or Multi- electrode Array
mM	millimolar
MRI	Magnetic Resonance Imaging
ms	millisecond
mV	millivolt
MVAR	Multivariate Autoregressive
NFP	Negative Field Potential
NFP/EE	Negative Field Potentials per Epileptic Event
P#	Postnatal Day #
PFP	Positive Field Potential
PFP/EE	Positive Field Potentials per Epileptic Event
PET	Positron Emission Tomography
PS	Population Spikes
PWGC	Pairwise Granger Causality
RS	Regularly Spiking neuron
SVAR	Single variate autoregressive
<i>tish</i>	telencephalic internal structural heterotopia

Abstract of Dissertation Presented to the Graduate School
of the University of Florida in Partial Fulfillment of the
Requirements for the Degree of Doctor of Philosophy

CHARACTERIZATION OF IN VITRO EPILEPTIFORM ACTIVITY AND PROPAGATION
IN THE IN UTERO IRRADIATED RAT MODEL

By

John Nicholas Grimes

May 2011

Chair: Thomas B. DeMarse
Major: Biomedical Engineering

Epilepsy, one of the most common serious neurological conditions, is characterized by spontaneous recurrent seizures, the catastrophic synchronization of brain activity. While anti-epileptic drugs are used as the first-line treatment, they fail in approximately 20 – 30% of patients. Further, this failure rate is dependent on the type of epilepsy and its cause. Malformations of the cortex have been highly correlated with epilepsy, with an estimated 75% of patients having a cortical malformation presenting with epilepsy at some point. Further, cortical malformations are typically less responsive to drug therapies. Although estimated to only exist in 14% of epilepsy patients, cortical malformations account for between 25 – 40% of all medically intractable childhood epilepsies.

While the normally laminated cortex has been studied for over 100 years, only more recently has attention been devoted to the malformed cortex. In order to study the role that cortical malformations play in epileptogenesis, animal models of cortical dysplasia, such as the *in utero* irradiated rat model, have been employed by researchers. Unfortunately, the bulk of this work has been focused on histological and

intrinsic neuron property differences with little consideration given to the emergent network properties in dysplastic slices.

In this work I utilized the *in utero* irradiated rat model to induce cortical dysplasia and compared electrophysiological differences between normal and dysplastic cortex using microelectrode arrays (MEAs). Several metrics were used in the analysis and were categorized as classic, spatial, and novel. Classic metrics were those used by previous researchers to compare epileptiform activity in dysplastic and normally laminated cortices and included ictal event lengths, ictal event distributions, and number of field potentials per ictal event. Spatial metrics were those used by previous researchers to analyze normally laminated cortical slices but have not been applied to dysplastic slices or used to compare the two. New metrics consisted of the application of Granger Causality methods to the data, which have been used previously in neuroscience, but not to compare functional differences between normal and dysplastic tissue.

Results supported and expanded upon previous counter-intuitive and anecdotal evidence that low dose irradiated subjects are functionally more dissimilar from controls than high dose irradiated subjects. This was evidenced by key classic and spatial metrics, such as mean number of ictal events per recording time, mean event length, mean inter-event interval, bias in LFP extrema peaks during events, and wave speed propagation through cortical layers. Surprisingly, and of most potential clinical relevance, results from novel application of Granger Causality analysis to *in vitro* slice suggests that localized areas drive ictal activity when a dominant initiation site is absent and do not coincide with dominant initiation sites when present.

CHAPTER 1 INTRODUCTION AND BACKGROUND

Introduction

Epilepsy is a chronic neurological condition characterized by spontaneous, recurrent seizures, the catastrophic synchronization of brain activity. One of the common serious brain disorders (Hirtz et al., 2007), epilepsy is estimated to afflict nearly 1% of the population, including over 2.3 million Americans (Begley et al., 2000; Garnett, 2000) and approximately 50 million people worldwide (Scott et al., 2001).

Anti-epileptic drugs (AEDs), such as carbamazepine and phenytoin, serve as the first-line treatment of epilepsy (Chisholm and WHO-CHOICE, 2005). In most cases, these pharmacological agents are able to reduce both the frequency and severity of seizure events. Unfortunately, between 20-30% of patients are unresponsive to pharmacological treatment. (Leppik, 1992; Kwan and Brodie, 2000; French et al., 2004). Additionally, a significant portion of patients who do respond to AEDs suffer from intolerable side effects, such as cognitive problems, liver toxicities, severe rash, and low white blood cell or platelet counts (Greenwood, 2000; French et al., 2004). In severe cases of intractable, pharmacologically unresponsive or intolerable epilepsy, additional treatments are employed. These treatments include highly restrictive ketogenic diets, electrical stimulation of the nervous system, and surgery to remove epileptogenic portions of the brain.

The success rate of these treatments is heavily dependent on the type of epilepsy, its cause, and region of the brain in which the seizures originate. For instance, epilepsies originating in the neocortex, or outer layer of tissue surrounding the brain, are typically the least responsive to pharmacological agents and even surgical

outcomes are far less favorable than other types of epilepsy. Post-surgical seizure-free rates for patients with neocortical epilepsy range between 20 and 40%, compared to between 70 and 80% for epilepsies that have a clearly defined lesion causing the seizures (Aykut-Bingol et al., 1998; Mosewich et al., 2000; Sisodiya, 2000).

Causes of Epilepsy

Approximately 70% of epilepsy cases are classified as idiopathic or cryptogenic, meaning the cause is not known (Hauser and Hesdorffer, 1990). The remaining cases are caused by a number of factors, both exogenous and endogenous. Exogenous causes include brain trauma, hypoxia, exposure to certain toxins, and infection. Endogenous causes include congenital conditions like Down's or Angelman's syndrome, brain tumors, and genetic factors.

Cortex Anatomy and Physiology

In order to better understand previous experiments and interpret their findings on activity propagation, a brief overview of cortex anatomy and physiology is first required. For a more in-depth description of the human cortex, see Nieuwenhuys et al. (2008). For the rat cortex, see Kolb and Tees (1990).

The cerebral cortex is the outer most tissue surrounding the cerebrum and is classified into three regions based upon the number of layers formed by cytoarchitecture, or distribution of neuron cell bodies: the archicortex, the paleocortex, and the neocortex. The archicortex includes the hippocampal formation and is comprised of three distinct cell layers. The paleocortex includes the olfaction, entorhinal, and periamygdaloid cortices and varies between three to five cell layers. The paleocortex and archicortex together are referred to as the allocortex. The third region, which accounts for approximately 90% of the cerebral cortex, is classified as

neocortex or isocortex. The neocortex is evolutionarily the youngest portion of the mammalian brain and is the location where higher brain functions, such as spatial reasoning, language processing, and conscious thought, arise. Two main structural features are present throughout the neocortex (Lynch, 1997; Nieuwenhuys et al., 2008).

The primary structural and most visible feature of the neocortex is its laminar organization. First reported by Brodmann (Brodmann, 1909) in his seminal work, *Vergleichende Lokalisationslehre der Grosshirnrinde in ihren Prinzipien dargestellt auf Grund des Zellenbaues*, six distinct horizontal cytoarchitectural layers of cells are present throughout the entire neocortex. These six cell layers are denoted by Roman numerals, with layer I denoting the outermost layer and layer VI denoting the basal layer. Although a number of neuron types are present, the pyramidal cell is by far the most common and is almost the sole output pathway for information out of the cerebral cortex, with other cell types serving as interneurons. Further, pyramidal neurons within the cortex project to specific locations depending on which layer the cell body resides. Typically, cell bodies in layers II and III have axons that either terminate on cortical cells in the same hemisphere or run through the corpus callosum and synapse on neurons in the opposite hemisphere. Layer V neurons project to subcortical structures. Finally, layer VI neurons terminate on multiple areas, such as the thalamic nuclei or other cortical regions.

The second structural feature of the neocortex is its columnar organization. Across the neocortex, neurons are grouped together into modular and repeating vertical columns that run perpendicular to the surface and span cell layers II – VI (Mountcastle,

1978). Mountcastle, who studied the somatosensory cortex of behaving cats and monkeys, first observed these cortical columns. He discovered that a small area of cortex received information from one location, such as a finger, while a nearby area of cortex received information from a different area, such as the palm. Further, it was shown that different columns that received information from the same location were responsible for processing different sensory submodalities, such as light touch on the skin or heavy pressure on deeper tissues.

Cortical Dysplasia and Epilepsy

Cortical dysplasia refers to abnormal deviations in the structure of the cortex. First examined as a causative factor of epilepsy by Taylor et al. (Taylor et al., 1971), a strong correlation between cortical dysplasia (CD) and epilepsy has been found. Both during and after embryological development, a number of factors such as genetic mutations (Granata et al., 1997; Fox et al., 1998; Gleeson et al., 1998; Kato et al., 1999), *in utero* injuries (Palmini et al., 1994; Roper et al., 1995; Roper et al., 1997; Roper, 1998; Kondo et al., 2001), and postnatal insults (Sarnat, 1987; Lombroso, 2000) can lead to malformations of cortical development (MCD). These malformations interrupt the regular laminar and/or columnar structure of the cortex and have been classified extensively using different schemes, such as the timing of the insult leading to the malformation (Barkovich et al., 2001; Leventer et al., 2008; Abdel Razek et al., 2009) and causative genes leading to the malformation (Barkovich, 2005). Depending on the cause, malformations may focal, or localized to one small area of the cortex; multi-focal; or generalized throughout the entire cortex (Barkovich et al., 1996).

Although cortical dysplasia alone does not assure epilepsy and animal models of cortical malformations, such as the reeler mouse, that neither present nor display an

increased propensity for seizures exist (Schwartzkroin and Walsh, 2000), it is estimated that a striking 75% of patients having a cortical malformation will have epilepsy (Leventer et al., 1999) and that a cortical malformation is present in at least 14% of all epilepsy cases (Meencke and Veith, 1992; Walsh, 1999). Further, epilepsies occurring in the presence of cortical malformations tend to respond poorly or not at all to AEDs and other therapies. An estimated 25% to 40% of all intractable or medically resistant childhood epilepsies are due to a cortical malformation (Hardiman et al., 1988; Farrell et al., 1992; Guerrini et al., 2002; Barkovich, 2005). Finally, full removal of the dysplastic tissue is the only predictive factor for seizure-free surgical outcomes for these epilepsies (Krsek et al., 2009) and differs from other forms of epilepsy, which are highly correlated to demographics, risk factors, and natural histories (Seino et al., 2000). The need to fully resect affected tissue for the best surgical outcomes becomes exceedingly problematic in cases where the dysplasia has multiple focal points, is generalized, or involves tissue in necessary areas, such as the motor cortex.

Models of Epilepsy

The exact mechanisms by which cortical dysplasia contributes to or causes epilepsy and other neurological problems remain unknown. Advanced imaging techniques, such as magnetic resonance imaging (MRI) and positron emission tomography (PET), and electrophysiological recordings, such as EEG, subdural electrodes, and microwire arrays, are used to localize cortical malformations and seizure origin in patients. While beneficial, these techniques are limited in their utility to elucidate the underlying mechanisms and more invasive methods must be employed.

Due to patient safety and ethical concerns, animal models are frequently employed by researchers to study the underlying causes of human epilepsy and

epileptogenesis, the processes by which a normal brain develops epilepsy (McNamara et al., 2006). A large number of animals, from drosophila to non-human primates, and epilepsy inducing protocols, such as electrical stimulation (kindling) (McIntyre, 2006) or injection of kanic acid (Dudek et al., 2006), have been chosen to investigate the mechanisms underlying epilepsy and to ascertain the safety and effectiveness of AEDs and other treatments prior to use in human subjects. In the last decade, at least two books, *Models of Seizure and Epilepsy* (2006) and *Animal Models of Epilepsy* (2009), and two detailed reviews on animal models of epilepsy have been published. Sarkisian (Sarkisian, 2001) presented a general overview of various epilepsy types and animal models used to study them, while Wong (Wong, 2009) focused specifically on animal models of focal cortical dysplasia and tuberous sclerosis complex. In the following sections, I give a brief overview of the animal selection and epilepsy induction protocol used in this study and refer more detailed discussion to these reviews.

Animal selection

Although a wide range of animals are used to model human epilepsy, research has been focused on mammals due to the structural similarities found across all placental mammal brains (Kolb and Tees, 1990). Due to its small size and ease of being housed and trained, the rat has been the principle choice of all mammals used and is by far the best studied. This has produced a rich corpus of information about the rat nervous system, including in-depth atlases (Zilles, 1985; Paxinos and Watson, 1997; Swanson, 1998; Paxinos et al., 1999; Ashwell and Paxinos, 2008; Altman and Bayer, 1995; Foster, 1998; Cooley, 2005), comprehensive books (Kolb and Tees, 1990; Paxinos, 2004), and countless peer reviewed publications either focusing specifically on the neurobiology of the rat or utilizing a rat model for neuroscience research.

Epilepsy induction protocols

In addition to animal selection, a valid epilepsy induction protocol must produce epileptogenesis whose presentation and underlying mechanisms most closely match the specific class of human epilepsy being studied is necessary. Since Goddard first published the effect of low intensity electrical stimulation, or kindling, on the rat brain (Goddard, 1967), a number of *in vivo* protocols that induce epilepsy in the rat and/or produce hyperexcitability or decrease inhibition *in vitro* have been identified. However, there is a fundamental difference between seizure models and epilepsy models. While a seizure is defined as a catastrophic neurological event due to the synchronization of brain activity, epilepsy is defined as a chronic condition marked by multiple recurrent seizures (Fisher et al., 2005). Thus, a protocol that produces an isolated seizure event, such as the administration of the neurotoxin, flurothyl, but does not cause recurrent seizures is not a viable model of epilepsy (Engel, 1992; Mody and Schwartzkroin, 1997).

Animal models of cortical dysplasia

Since cortical malformations are associated with epilepsies that are notoriously pharmacologically and surgically resistant, a number of animal model are aimed at inducing cortical dysplasia to examine the correlation with epilepsy. Many of these models have been described by previous researchers and can be categorized based upon when the protocol initiates the malformation: genetic, *in utero* insults, and neonatal manipulations (Schwartzkroin and Walsh, 2000; Najm et al., 2007).

Although the number of genetic based models that accurately mimic human cortical dysplasia is limited, a few popular ones do exist. These include the telencephalic internal structural heterotopia (*tish*) rat, the p35 knockout mouse, and

Ihara's genetically epileptic rats (IGERs) (Schwartzkroin and Walsh, 2000). *Tish* rats display a characteristic "double cortex", or band heterotopia, and a layer of gray matter below the normal gray matter in the frontal and parietal cortices (Lee et al., 1997). Some of these rats exhibit spontaneous seizures. The *p35* gene is key in the development of normal cortical structure. Loss of this gene causes the cortical structure to be inverted, which is similar to that of the *reeler* mouse (Chae et al., 1997) but caused by a different mechanism. Additionally, while the *reeler* mouse does not exhibit seizures or an increased propensity for seizures, one study has shown that a quarter of *p35* knockout mice exhibit seizures and an additional 50% of them display aberrant electrical activity (Wenzel et al., 2001). Finally, IGERs exhibit spontaneous seizures starting at around 5 months of age (Amano et al., 1996)

Two main classes of *in utero* insults exist: exposure to chemicals and radiation. Intraperitoneal injection of various drugs, such as the DNA alkylating agents methylazoxymethanol (MAM) and carmustine (1-3-bis-chloroethyl-nitrosourea or BCNU), into pregnant rats has been shown to induce cortical dysplasia, *in vitro* hyperexcitability, and in some models spontaneous epilepsy (Baraban et al., 2000; Benardete and Kriegstein, 2002; Harrington et al., 2007; Wong, 2009). The *in utero* irradiated rat model is discussed in more detail in the following section.

Cortical dysplasia models based upon manipulations to the neonate have also been examined. Closed head injury was first reported to have caused focal cortical dysplasia by Cowen et al. (1970). Subsequently, a number of other protocols have been studied. The more popular of which include cranial injection of ibotenate and freeze lesioning. Ibotenate is an analogue of the excitatory neurotransmitter

glutamate. When injected intracortically into the neonate rat it induces localized abnormal cortical lamination, heterotopic neurons, and deviant sulcus formation, thus approximating focal cortical dysplasia (Marret et al., 1995; Redecker et al., 1998a; Redecker et al., 2005; Wong, 2009). Freeze lesioning uses a freezing probe placed on the surface of the neonate's skull, thus killing cortical cells near the probe. Over time, a four-layered microgyrus appears at the site of insult (Jacobs et al., 1996; Jacobs et al., 1999b; Wong, 2009). In both of these models, slice recordings show increased hyperexcitability (Redecker et al., 1998b; Jacobs et al., 1999a; Kellinghaus et al., 2007) but no spontaneous epileptic activity has been observed in living animals. (Redecker et al., 1998b; Holmes et al., 1999; Kellinghaus et al., 2007)

The *in utero* irradiated rat model of cortical dysplasia

The original motivation behind irradiating rats during gestation was to study the process of normal cortical development by interrupting the process at various points in time (McGrath et al., 1956; Hicks et al., 1959). Noting that radiation induced cortical dysplasia and the correlation between cortical malformations and intractable epilepsy, Roper began utilizing the model for use in the study of epilepsy (Roper, 1998). While I subsequently present an overview, it is to his 1998 review and *Models of Seizures and Epilepsy* that I refer the reader to for a detailed analysis of the model (Roper, 1998; Lin and Roper, 2006).

The protocol used for this model is among the most simple and easy to perform. Timed-pregnant rats are exposed to radiation from an external source. Doses typically range from between 150 to 250 cGy in most laboratories, and no significant differences between linear accelerators or cobalt sources have been noted (Roper, 1998). Animal care and handling is otherwise no different from controls. Aside from reports of learning

deficiencies and hyperactivity (Hicks et al., 1959), irradiated litters birth, wean, and feed normally, and live long life spans (Lin and Roper, 2006).

In early studies, it was discovered that the development of the cortex was drastically altered by radiation and is highly dependant on the time of exposure (Hicks et al., 1959). Over the last 50 years, subsequent studies have pieced together the exact histological effects that irradiation at different timings play. Exposure early in the process of cortical development, such as embryonic day 12 (E12), produces a significantly thinner but otherwise regularly laminated cortex. Exposure on E13 through E14 generates large clumps of subcortical grey matter in the white matter beneath a thinned cortex (Ferrer et al., 1993b). The greatest dysplasia is caused due to exposure on E16, which causes loss of laminar and columnar structure and abnormal orientation of pyramidal cells. As development continues, the effects of irradiation diminish. Exposure on E17 and E18 are similar to, but less severe than, E16. Finally, the effect of exposure on E19 and E20 are limited to the superficial layers, which are the last to develop (Roper, 1998).

In addition to timing, the degree of dysplasia has been correlated to the amount of radiation administered (Jensh and Brent, 1987; Fukui et al., 1991; Fushiki et al., 1996; Miki et al., 1999). More recently, Kellinghaus et al. (Kellinghaus et al., 2004) analyzed the histological and electrophysiological effects that different amounts of radiation caused. In this study, rats were irradiated with either 100, 145, or 175 cGy on E17. While increased dysplasia was correlated with higher radiation doses, only animals in the group receiving 145 cGy displayed spontaneous seizures.

The basic mechanism by which *in utero* irradiation induces cortical dysplasia is thought to consist of a two-step process (Roper, 1998). First, cells are initially damaged or killed due to exposure to radiation. Cell death of mitotically active and immature cells in the cerebral cortex and hippocampus have been shown to be mitigated by cycloheximide, indicating that protein synthesis is a deterministic factor in cell death (Ferrer et al., 1992; Ferrer et al., 1993a). Cell death is also highest in regions where precursor cells are synthesizing DNA (Bayer and Altman, 1991). Early studies also indicated that immature migrating neurons were severely damaged by radiation (Hicks et al., 1959), and later studies showed that the most important factor in determining a cell's sensitivity to radiation was migration (Altman et al., 1968). Second, after the initial insult, cortical development proceeds in an altered cellular environment, which disturbs the complex embryological cascade, ultimately leading to cortical dysplasia (Marín-Padilla et al., 2003). For instance, prior work has shown that radial glia, which act as important guidance structures for migrating neurons, are also vulnerable to radiation (Rakic, 1972; Rakic, 1988). Roper et al. (1997) showed that irradiation on E17 disrupted glial fibers that did not recover during the perinatal period and that the dorsomedial cortex was the site of both the most severe glia disruption postnatal and cortical dysplasia as adults (Roper, 1998).

In order to verify its utility, a number of comparisons between human cases of cortical dysplasia and this model have been made. Several critical similarities between the two are present, but some minor differences do exist. Foremost, this model has been shown to produce acute tissue preparations that are both disinhibited and hyperexcitable *in vitro* (Roper et al., 1995; Roper et al., 1997; Zhu and Roper, 2000;

Chen and Roper, 2003), as well as animals that seize spontaneously *in vivo* (Kondo et al., 2001; Kellinghaus et al., 2004). Therefore, this model properly meets the requirements of an epilepsy model. The technical fulfillment of this definition is crucial since other frequently utilized models, such as freeze lesioning, produces hyperexcitable tissue *in vitro* but does not produce spontaneous epileptogenicity *in vivo* (Kellinghaus et al., 2007). Next, this model produces histological abnormalities similar to those seen in human patients. While attempts to provide a universal classification of human cortical dysplasia have yet to be successful (Roper, 1998), Michel et al. (1995) produced a list of nine pathological features present. This model consistently provides three of these histological features: loss of normal laminar structure, neurons present in cortical layer I, and white matter neuronal heterotopia (Roper, 1998). Three prominent differences between the animal model and human model have been noted. Although the *in utero* irradiated rat model does produce cortical dysplasia, it is diffuse and is therefore does not accurately model focal or multifocal dysplasia like other protocols, such as freeze lesioning (Lin and Roper, 2006). Additionally, while irregular neuron morphology is produced, no giant neurons or balloon cells have been reported. Thus, this model more closely approximates mild to moderate, but not severe or Taylor's type cortical dysplasia or cortical tubers (Mischel et al., 1995; Roper, 1998; Lin and Roper, 2006). A final striking difference between the model and human cortical dysplasia is that irradiated animals also have abnormal cell dispersions in the CA1 and CA3 regions of the hippocampus, which has yet to be seen in humans (Roper et al., 1995; Kondo et al., 2001).

***in vitro* Techniques**

Although much has been learned about epilepsy from behaving animals exhibiting chronic recurrent seizures, underlying mechanisms responsible require more in depth study. Due to the limitations on what information can be obtained from subjects *in vivo*, tissue samples from animals have been studied *in vitro*. To accomplish this, animals are deeply anesthetized, sacrificed by decapitation, and their brains quickly removed and placed in an oxygenated nutrient medium. The brains are then sliced into thin sections and then studied, often in the presence of various pharmacological treatments such as bicuculline methiodide, 4-AP, and picrotoxin. Three primary techniques have been utilized for studying epileptiform activity from living brain slices. These techniques allow real-time monitoring and/or stimulation of single neurons or neuron populations *in vitro*.

Whole-cell patch recording

The workhorse of modern neuron electrophysiology, whole-cell patch recording is a technique that evolved from voltage clamping to achieve intracellular recording from a single neuron. In this technique, a glass micropipette filled with an ionic solution similar to the intracellular matrix with an approximately 1- μm opening serves as an electrode and is placed on the surface of the cell. Suction is then applied to remove a small section of the cell membrane, allowing access to the intracellular matrix. This allows recording of the total current through all ion channels across the cell membrane (Dhillon and Jones, 2000; Kandel et al., 2000; Yang and Benardo, 2002).

While the patch clamp method provides the most information possible about activity of a cell, there method has some limitations. The primary drawback is the difficulty in recording from more than one cell at the same time. Due to space

limitations, the technique does not scale, and it is not possible to obtain information from more than three or four neurons within a slice at the same time.

Being limited to two or three electrodes leads to reliance on signal processing techniques, such as triangulation based on waveform delays and propagation velocity estimation, (Tsau et al., 1998) or multiple stimulations and recordings at different locations (Telfeian and Connors, 1998) to ascertain information about the initiation location of epileptiform activity and propagation patterns. These techniques may be unreliable since signals in different cortical layers may propagate at different velocities.

Optical imaging with voltage and calcium sensitive dyes

Due to the physical constraints of monitoring activity at more than a few neurons simultaneously with patch clamp methods, new methods to ascertain neural activity were sought. The application of voltage sensitive dyes to electrophysiology has allowed researchers to observe changes in membrane potentials and neuron activity both *in vitro* (Cohen and Leshner, 1986; Yuste and Katz, 1991; Tsau et al., 1999; Baker et al., 2005; Trevelyan and Yuste, 2009) as well as *in vivo* (Grinvald et al., 1984; Kleinfeld and Delaney, 1996; Petersen et al., 2003).

In this technique, a voltage or calcium sensitive dye is added to the ACSF. Changes in voltage or calcium ion concentration cause a conformational change in the dye, which in turn changes the absorbance spectrum of the dye. A light source with a known spectrum is continuously passed through the tissue. Absorbance changes are obtained by a photo diode array or charged coupled device (CCD), which detects the light transmitted through the tissue. (Trevelyan and Yuste, 2009)

While this technique allows a much greater amount of activity of the slice to be observed, three primary drawbacks exist. First, although activity over a large area of

the tissue can be observed, stimulation cannot and must be performed by other means. Second, a great deal of experimental calibration and optimization is necessary to achieve a high signal to noise ratio. Finally, prolonged optical recording is limited due to dye bleaching and because the dyes may have an effect on the cells, such as modulating activity or damaging them. (Wu et al., 1993; Momose-Sato et al., 1995; Tsau et al., 1999; Baker et al., 2005)

Microelectrode arrays

The microelectrode array (MEA) was developed in the late 1970s using semiconductor fabrication techniques and was designed to circumvent the problems inherent with patch-clamp methods of recording from or stimulating multiple neurons simultaneously while also allowing for a far greater number of sites to be recorded from than previously possible (Thomas, 1972; Gross et al., 1977; Pine, 1980). While the first device possessed only 30 electrodes, MEAs have benefited greatly from advances in electronics and fabrication techniques, increasing the number of electrodes and sampling rate. The current standard MEA system in use at most research facilities consists of a 60 or 64 channel system, although commercial MEA systems can be purchased capable of acquiring data from 256 electrodes simultaneously (Ayanda Biosystems, Lausanne, Switzerland).

Fundamentally different than the intracellular recordings gained by the patch-clamp method, the MEA records changes in extracellular potentials caused by changes in ion concentrations due to cellular activity. As illustrated in Figure 1-1, MEAs are capable of detecting a wide array of dynamic activity, including population spikes (PS), local field potentials (LFP) such as field excitatory post synaptic potentials (EPSP) and

field inhibitory post synaptic potentials (IPSP), interictal, ictal events, and occasionally single-unit action potentials, also known as spikes.

Although chiefly used in neuroscience research, MEAs have been utilized on a broad array of cell and tissue types exhibiting electrical properties, cardiac (Thomas, 1972; Israel et al., 1984; Connolly et al., 1990; Natarajan et al., 2006), retinal (Wong et al., 1993; Meister et al., 1994; Grumet et al., 2000; Stett et al., 2000), and even cancer cells (Rothermel et al., 2006; Wolf et al., 2008). Within neuroscience applications, MEAs are used primarily to study dissociated neuron cultures, but have gained considerable traction by researchers using cultured organotypic tissue and acute slices of neural tissue (Novak and Wheeler, 1988; Egert et al., 1998; Oka et al., 1999; Egert et al., 2002; Heuschkel et al., 2002; Beggs and Plenz, 2004). In order to increase signal transduction between the tissue slice and electrodes, adaptations to the planar MEA have been made in which the electrodes are cones measuring on the order of 30 μm at the base and a height on the order of 60 μm (Heuschkel et al., 2002). The electrodes of these “3D” MEAs are able to pierce the outer layer of cells in the slice, which are typically dead or damaged during the specimen preparation process and insulate the active cells from planar electrodes. Figure 1-1 shows electrophysiological recordings from an acute rat cortical slice collected with a “3D” MEA, while Figure 1-2 shows an acute rat hippocampal slice on a “3D” MEA. Due to these advances, MEAs are now being employed to examine slice-wide activity of acute cortical rat and hippocampal slices (Egert et al., 2002; Beggs and Plenz, 2004).

Previous Work and Literature Review

Here I present a brief overview of the electrophysiological activity that has been reported to occur in both normally laminated and *in utero* irradiated induced dysplastic

acute rat cortical slices. Topics covered include stages of epileptiform events, propagation patterns and velocities, signal amplitudes, and waveform features.

Normally Laminated Slices

In order to understand the functional abnormalities caused by *in utero* irradiation induced cortical dysplasia, a review of electrophysiological activity in normal cortical slices is necessary. Although the role of the neocortex in pharmacologically resistant epilepsies has been increasingly apparent over the last two decades, the functional connectivity of the hippocampus structure has garnered the bulk of investigation (Borbély et al., 2006). Recently, significant efforts have increasingly been focused on characterizing epileptiform activity in the neocortex. Broadly, the results of these efforts can be placed into one of the following four categories: salient anatomical structures and physiologic properties, initiation of an epileptiform event, propagation of the activity to other neuron populations, and event termination.

Salient anatomical structures and physiological properties

The foundations on which all neocortical processing, oscillations, and epileptiform activity are built is the anatomical and physiological properties of the neocortical neurons. Used frequently for both *in vitro* and *in vivo* epilepsy experiments, the structural organization of the rat somatosensory cortex has been fairly well examined (Woolsey and Van der Loos, 1970). More recently, a number of journal articles have elucidated several cytoarchitectural features of the neocortex, which are thought to be specifically related to the formation and maintenance of epileptiform activity.

First, two main types of pyramidal neurons have been described in the neocortex: the intrinsically bursting (IB) neuron and the regularly spiking (RS) neuron (Connors et al., 1982; McCormick et al., 1985; Chagnac-Amitai et al., 1990; Larkman and Mason,

1990; Amitai, 1994; Williams and Stuart, 1999; Hefti and Smith, 2000). These two pyramidal neuron types differ in their distribution throughout the neocortical layers, electrophysiological properties, and connectivity. Although both neuron types are found in layer V of the neocortex, RS neurons are also found in layers II and III (Gottlieb and Keller, 1997). Electrophysiologically, the IB neuron type is capable of high frequency bursts of action potentials (Kasper et al., 1994), while the RS neuron type produces more regular discharges (Chagnac-Amitai et al., 1990). The cell types also show significant morphological and functional connectivity differences. IB cells are typified by large somas, thick apical trunks, and heavily branched dendrites, while RS cells have smaller somas, thinner apical trunks, and less branched dendrites (Chagnac-Amitai et al., 1990; Larkman and Mason, 1990). IB cells have extensive horizontal axonal projections within the infragranular layers (Kasper et al., 1994), while layer V RS cells' horizontal afferents project more strongly into layer VI and more weakly to layers II/III and V (Gottlieb and Keller, 1997). Both cell types receive excitatory and inhibitory inputs from all cortical cellular layers, although the laminar distribution of inputs differs between the two types. Layer VI serves as the predominant source of excitatory input into IB cells whereas layer V is for RS cells (Schubert et al., 2001). Inhibitory inputs onto IB cells arrive from layers II/III, IV, and V but exhibit far less control on these cells than the inhibitory inputs arriving from layers II/III and V on RS cells (Schubert et al., 2001).

Second, electrophysiological properties intrinsic to different cortical layers, which in healthy tissue are thought to be responsible for cortical information processing, may play a significant role in the prevention and control of epileptiform activity. A strong

dichotomy between the electrophysiological action of superficial and deeper cortical layers has been documented (Barkai et al., 1995; van Brederode and Spain, 1995; Yang et al., 1998; Dhillon and Jones, 2000; Yang and Benardo, 2000; Yang and Benardo, 2002). Specifically, superficial cortical layers appear to have a primarily inhibitory action whereas deeper cortical layers appear primarily excitatory (Barkai et al., 1995; Yang and Benardo, 1997; Yang et al., 1998). Yang and Benardo performed a series of experiments on intact and laminar strips of cortical slices that reaffirmed and expanded upon previous reports (Yang and Benardo, 2002). First, it was shown that isolated superficial layers are the only layers capable of glutamate-independent synchronized activity and that the synchronization was due to GABAergic activity. Second, excitatory activity in the superficial layers was weak, even though the tissue was bathed in the convulsant 4-AP. Third, activity in the middle and deep layers is primarily excitatory, since it is mediated through glutamatergic transmission. And finally, that the superficial inhibitory network can exert considerable control over the deeper layers.

These intrinsic laminar properties have been postulated to play a significant role in epileptiform activity. The excitatory / inhibitory stratification of the cortex has led some to postulate that the deep layers may be seizure sensitive while the superficial layers may be seizure resistant (Lopantsev and Avoli, 1998; Dhillon and Jones, 2000). It has been suggested that ictal events in rat neocortical slices are initiated by excitatory neurons isolated in the deep layers and then spread to the superficial layers (Connors, 1984; Hoffman and Prince, 1995; Lopantsev and Avoli, 1998). For instance, Connors (1984) used 400 – 500 μm thick slices of guinea pig sensorimotor neocortex and measured the

amount of focally applied L-glutamate or increased K^+ concentration to each layer necessary to evoke a paroxysmal field potential in the slice. It was found that a drastically smaller quantity applied to Layer IV or upper Layer V was necessary to evoke a slice-wide response, as compared to the other layers. In another experiment, Connors found that focally applied bicuculline applied to the superficial and deep layers caused no effect or a marginal increase in amplitude from the recording site nearest the application. However, when applied to the middle layers, the same amount of bicuculline caused field potentials of prolonged and variable latency. Further, one study documented that ictal discharges from the deep cortical layers are attenuated in layer II and hypothesized that this layer actively filters and controls epileptiform activity (Lopantsev and Avoli, 1998)

Initiation of epileptiform events

Initiation is the first phase of an epileptiform event. Having particular clinical relevance to epilepsy, knowing the causes and locations of initiation are imperative to designing treatments and preventative measures. Earlier studies have pointed towards IB neurons located in layer IV or V as potential “pacemakers” for these events (Connors, 1984; Chagnac-Amitai and Connors, 1989b; Silva et al., 1991). However, it was unknown whether the initiation process was dependent on a small number of cells or was an emergent property due to the interactions of a large number of cells throughout tissue.

Tsau et al. (1998) sought to solve this question using optical imaging and two electrodes to monitor spontaneous epileptiform activity in acute cortical slices. They reasoned that if events were initiated by a small number of cells, the initiation site would be confined to a localized area of tissue. While if events were initiated by the

interactions of a large number of cells, the initiation site would be a large, diffuse area with no apparent localized point (Tsau et al., 1998). Three interesting phenomena about initiation of epileptiform activity were discovered. First, every observed event began in a confined spot measuring less than the area of one of the photodetector elements used ($0.141 \mu\text{m}^2$) and subsequently propagated throughout the rest of the tissue. Second, all spontaneous events were initiated from a few confined initiation foci, further lending credence to the idea that initiation is started by a small localized grouping of “pacemaker” neurons. Finally, it was always found that one focus dominates over the other foci for a period of time before yielding to one of the other foci. Unfortunately, the locations of these foci were estimated from data obtained using only two electrodes, estimated horizontal and vertical propagation speeds, and clustering upon latency times. Using other techniques to verify the existence and location of initiation foci is desirable.

While Tsau reported that ictal events were always generated from two to three focal sites within a slice and these sites exhibited temporal dominance, other researchers have reported conflicting findings. For instance, using organotypic slices on microelectrode arrays and either BIC or kainic acid, Jimbo and Robinson (Jimbo and Robinson, 2000) reported that ictal events initiated in the superficial cortical layers and did not arise from a dominant focal point. Further, others have noted that the dominant layer of ictal generation depends on the type of treatment used. In most preparations, the deep layers serve as the ictal generation zone, but it has been observed that the upper layers are responsible when treated with kainic acid (Flint and Connors, 1996)

Propagation of epileptiform activity

Once a successful initiation event occurs, the activity propagates from the focus to surrounding tissue. Similarly as important as initiation in clinical relevance and a potential target for therapeutic advancements, propagation of epileptiform activity through the neocortex has received considerable study. Previous researchers have described the process of propagation not as a series of sequential initiations (Ermentrout, 1998), but as the transmission of synchronous activity from one population of neurons to another (Chervin et al., 1988; Chagnac-Amitai and Connors, 1989a; Golomb and Amitai, 1997; Ermentrout, 1998). Studies focusing on propagation consistently have been focused upon three main features: the pattern and speed by which the activity spreads, the importance and necessity of certain cortical laminae to support propagation, and mechanistic dependencies on which propagation relies.

Studies evaluating the propagation of neuronal activity in acute cortical slices have primarily observed evoked response to white matter electrical stimulation. Though distinctively different than endogenous activity, they provide key insight into the underlying functional architecture by which spontaneous activity also travels. For instance, Contreras and Llinás (2001) described propagation patterns, calculated velocities, and showed propagation dependency on stimulation frequency. In their study, acute slices of guinea pig somatosensory cortex were electrically stimulated in the white matter and evoked responses were observed using voltage sensitive dyes and intracellular recordings. During single stimulation, imaging revealed that tissue in layer VI immediately above the stimulation electrode was activated. Activity from this activation site immediately propagated vertically towards the pial surface and, nearly simultaneously, horizontally through layers V and VI. Once the wave front reached

layers II and III, activity propagated through those layers as well, although at a slightly slower velocity than in the infragranular layers.

Although the majority of studies observing propagation of evoked activity through cortical tissue stimulate sites in the white matter, similar propagation patterns are generated when stimulating any layer of cortex. For instance, Tsau et al. (1999) used a microelectrode and progressively stimulated each cortical layer and observed the evoked with response with voltage sensitive dyes. In every case a response was evoked, activity propagated vertically from the site towards the pia and almost simultaneously horizontally through the laminae.

Interestingly, propagation patterns display a strong dependency on stimulation frequency. Two experiments by Contreras and Llinás (2001) clearly demonstrated this frequency dependency by stimulating the white matter with different pulse trains, one at 10 Hz and one at 40 Hz. These frequencies were chosen due to their biological relevance. During slow-wave sleep, EEG is dominated by low frequency oscillations less than 15 Hz (Steriade et al., 1993; Contreras et al., 1996; Contreras et al., 1997), while high frequency oscillations in the range of 30 – 50 Hz dominate while awake (Steriade et al., 1993; Destexhe et al., 1999). In the first experiment, five pulse trains were applied at each frequency and the optical response measured. When the 10 Hz pulse train was applied, there was no appreciable difference in activity propagation between the first and fifth stimulation sequence. However, when the 40 Hz pulse train was applied, the activation profile gradually shrank, and by the fifth stimulation the wave propagation was restricted to a small, columnar area directly above the stimulation electrode. In the second experiment, one or both of two sites 1.5 mm apart were

stimulated with the pulse trains. When only one or the other site was stimulated, the response was as previously described. When both sites were stimulated simultaneously at 10 Hz, two waves spread from each site and coalesced in the middle of the slice. However, when both sites were stimulated at 40 Hz, activity propagation was limited to two separated columnar areas over both electrodes.

Intrinsic to propagation patterns, the velocity at which activity propagates has also been studied in neocortical slices. Estimates of propagation velocity vary widely by activity type, pharmacological treatments, and direction of propagation. Wu et al. (2001) reported velocities from two types of activity, ensemble activity and a “fast response” to stimulation that precedes ensemble activity, and compared them with literature reports of a third type, interictal spikes in pharmacologically disinhibited slices. Using optical imaging to observe evoked activity propagation, they reported ensemble activity propagated horizontally through cortical laminae much slower than fast response or literature reported interictal spikes at 1 – 20 mm/s, compared to 40 – 160 mm/s and 40 – 160 mm/s, respectively (Chervin et al., 1988; Wadman and Gutnick, 1993; Tanifuji et al., 1994; Golomb and Amitai, 1997; Tsau et al., 1998; Demir et al., 1999). Noting that ensemble activity propagation velocities were drastically slower than interictal spikes in disinhibited slices, Wu et al. directly compared the velocity of these two activity types in the same slice. Each slice was first perfused with normal ACSF and the velocity of ensemble activity was measured with optical imaging. Then, a modified ACSF containing 10 – 20 μM of bicuculline was perfused for 20 – 30 minutes and the velocity of interictal spikes was measured. It was found that the ensemble activity propagated over an order of magnitude slower than the disinhibited interictal spikes (11 ± 6 mm/s

vs. 125 ± 24 mm/s). The extreme change in propagation velocity within the same slices when treated with bicuculline further corroborated earlier reports that suggested inhibition is essential for controlling propagation velocity (Tanifuji et al., 1994).

Direction of propagation also strongly affects velocity and signal amplitude. As previously discussed, activity propagating from an initiation site moves both vertically towards the white matter and pia and almost simultaneously horizontally through the cortical laminae. Contreras and Llinas (2001) measured the propagation speed and showed velocity dependencies on both direction of propagation and cortical layer. Activity propagating vertically from layer VI to layer I was fastest and measured at 265 ± 48 mm/s. Horizontal deep layer propagation was faster than superficial propagation and was measured at 217 ± 53 mm/s and 181 ± 44 mm/s, respectively. Similarly, activity amplitude also is dependent on cortical layer. While activity propagates more quickly through the deep cortical layers, larger signal amplitudes are observed in the superficial layers (Connors, 1984; Connors and Amitai, 1993; Shepherd and Koch, 1998; Telfeian and Connors, 1999; Bai et al., 2006).

In addition to playing pivotal roles in the initiation of epileptiform activity, propagation velocity, and signal amplitude, specific cortical layers are required for sustaining epileptiform discharges. Three sets of experiments conducted by Telfeian and Connors (1998) showed that layer V is central to epileptiform activity propagation in mildly disinhibited cortical slices. In these experiments, neocortical slices were bathed in ACSF containing either high ($35 \mu\text{M}$) or low ($1.0 - 2.5 \mu\text{M}$) concentrations of picrotoxin and activity was evoked by electrical stimulation of the white matter.

In the first experiment set, partial vertical cuts (perpendicular to laminae) were made, leaving bridges of intact tissue. Sites in the white matter were stimulated and two recording electrodes placed at opposite ends of the slice in layer II/III monitored if propagation across the slice was successful. In slices bathed in high concentrations of picrotoxin, epileptiform activity successfully propagated across the slice as long as an intact tissue bridge at least 350 μm wide existed, independent of the layer the bridge was in. However, in slices bathed in low doses of picrotoxin, propagation across the slice was only successful if the tissue bridge was in layers IV and V or V and VI.

In the next set of experiments, propagation was compared between intact slices and slices in which horizontal cuts (parallel to laminae) were made to section the superficial, middle, and deep cortical layers. Intact and sectioned slices were able to successfully propagate activity in the presence of both high and low doses of picrotoxin. In the presence of low doses of picrotoxin, only intact and sectioned middle layers (layers IV and V) were able successfully propagate activity. This suggested that layer V is necessary for propagation if considerable inhibition is still present.

To further test this notion, intact slices were stimulated in the white matter and a recording electrode was placed in either layer I or layer VI to measure the horizontal distance of propagation. When the recording electrode was in layer I, horizontal cuts were progressively made between layers starting with the layer VI-V interface and moving upwards. When the recording electrode was in layer VI, horizontal cuts began at the layer I-II/III interface and moved downward. In both cases cuts were not complete and an intact vertical strip with all layers always remained above the white matter stimulation site. Other than one exception, none of these horizontal cuts, which

eliminated successive lower or upper layers, had any effect on lateral propagation distance unless part of layer Va (the superficial strata of layer V) or Vb (the deeper strata of layer V) was involved. When cuts were near the layer Va-Vb border, propagation distance was severely affected. Additionally, propagation was never entirely successful unless part of layer Vb remained intact.

In the final set of experiments, one recording electrode was placed in layer II/III above the stimulation site and another recording electrode was laterally at least 2 mm away. A series of focal GABA applications was made starting at the pia and moving downward in 200 μ m increments. One second after focal GABA application, the white mater was stimulated and propagation was monitored. Trials were spaced at 1-minute intervals to allow for complete recovery. GABA application to layer V caused the greatest effect on propagation latency. Further, dosages of GABA applied to layer V that completely blocked propagation were unable to similarly block propagation when applied to other layers.

Event termination

The third and final phase of an epileptiform event is termination. Although logically and functionally different from the processes of initiation and propagation, termination has received considerably less attention. Studies examining termination have been almost completely focused on underlying cellular mechanisms, nearly ignoring the interactions among neuron groups and the emergent properties that may contribute extensively to the process.

A number of intrinsic neuron properties and cellular mechanisms are evidenced to play key roles in the termination process. For instance, Bikson et al. (2003) demonstrated that epileptiform activity in hippocampal slices does not depend on

continuous somatic neuron firing. This may be attributed to the fact that although the neurons enter a depolarization block arresting the soma, the axon terminals may still be active (Gutnick and Prince, 1972; Noebels and Prince, 1978). Another example is the importance of synaptic interactions in the formation of secondary waves, which is demonstrated by effectively blocking them with NMDA receptor antagonists (Miles et al., 1984; Lee and Hablitz, 1991; Traub et al., 1993; Telfeian and Connors, 1998). Finally, since glial cells play a role in the clearance and maintenance of neurotransmitters in the extracellular space, they may have a significant function in all three stages of epileptiform events (Duffy and MacVicar, 1999; Kettenmann, 1999; Schousboe, 2003).

Pinto et al. (2005) presented one of the few works examining termination at both cellular and network levels. Here, the concept of termination was examined in two different ways. Spatially, termination was approached as propagation failure (Bressloff, 2001). Temporally, it was approached as the process by which secondary activity patterns following an initial wave front eventually return to rest (Miles et al., 1984; Traub et al., 1993). Utilizing a linear microwire array placed in layer II/III to record LFPs and whole-cell patch techniques to record individual neurons in layers II/III and V, evoked responses to layer IV stimulation were observed. Network-level results showed that, like initiation, termination occurred at discrete locations that remained constant from trial to trial. Moreover, in two-thirds of trials, termination coincided with the end of the initial depolarization wave. However, in one-third of trials, complex secondary patterns arose. Compared to secondary waves in the disinhibited hippocampal slices (Miles et al., 1984; Traub et al., 1993), the secondary activity in the neocortex was much less uniform from trial to trial. Cellular-level results showed that termination coincided with the patched

neurons entering a depolarization block. Further, individual neurons in both layers II/III and V were active during secondary activity.

***In Utero* Irradiated Induced Dysplastic Slices**

Although increasingly used to study human epilepsy, animal models of cortical dysplasia have yet to receive the amount or depth of study of normally laminated slices. Little work has been done in understanding the emergent properties of neuronal populations in dysplastic cortex. Of the few studies conducted, nearly all utilized dysplasia models other than irradiation, particularly freeze lesioning. Since the freeze lesioning model aims to replicate polymicrogyria, while the *in utero* irradiated model causes generalized cortical dysplasia, and since freeze lesioning fails to produce animals that are epileptic, applicability of results from these studies to the *in utero* irradiated model is questionable. Further, no literature currently exists examining differences in the three logical phases of epileptiform events in the *in utero* irradiated rat model of cortical dysplasia. The overwhelming majority of experiments conducted on the *in utero* irradiated model have been primarily focused on *in vivo* EEG features, individual *in vitro* epileptiform waveforms, differences in neuron distributions, and functional differences of neurons in dysplastic cortex.

***In vivo* EEG**

Roper et al. (1995) reported differences in EEG signals between controls and *in utero* irradiated animals in the first analysis of the model. In this study, EEG recordings from surgically placed skull screws were taken from control and E17 pups irradiated with 196 cGy of gamma radiation. Neither group displayed ictal activity under normal conditions, but one experimental animal exhibited interictal activity at 0.8 spikes per minute. Once the anesthetic agents acepromazine or xylazine were administered,

experimental animals displayed ictal activity, while controls did not. Further, both control and experimental animals displayed interictal activity under these anesthetic agents, but the mean frequency of interictal discharges was higher in experimental animals than controls, 2.7 ± 0.79 Hz and 1.1 ± 0.42 Hz respectively.

Later, Kondo et al. (2001) expanded on these finding by performing the first continuous EEG monitoring of the *in utero* irradiated rat model, an injury-based cortical dysplasia model. The experimental group was composed of rats that were exposed to 145 cGy of radiation on E17. Recording electrodes were implanted into 7 control and 7 experimental rats at P45 and EEG signals were monitored for 71 – 297 hours (mean 174.1 hours) beginning 24 hours after electrode implantation. During the monitoring periods, interictal discharges were observed only in one of seven control rats, but all 7 of the irradiated rats. Further, while none of the control rats exhibited spontaneous seizures measured with EEG, four of the irradiated rats did.

Most recently, Kellinghaus et al. (2004) compared the effects of varying radiation doses and performed long-term video and EEG recordings. Three experimental groups were formed by exposure to 100, 145, or 175 cGy of radiation on E17 and EEG electrodes were surgically implanted on P60. No interictal epileptiform discharges were observed in the control rats, but occurred at a median frequency of 0.89 per hour in the 100 cGy-dosed group, 0.83 per hour in the 145 cGy-dosed group, and 0.29 per hour in the 175 cGy-dosed group. Interestingly, spontaneous seizures were observed only in the 145 cGy-dosed group, even though a positive correlation between radiation dose and the dysplasia severity was found.

***In vitro* epileptiform waveforms**

After the first study demonstrating that *in utero* irradiated rats displayed ictal EEG recordings and may serve as a model of epilepsy, Roper et al. (1997) examined whether the protocol generated a greater propensity for epileptiform activity than normally laminated slices in the presence of the GABA_A antagonist bicuculline methiodide (BMI). The experimental group was exposed to 225 cGy of radiation on day E17. After weaning on day P21, 400 μm thick coronal *in vitro* brain slices were prepared with a vibraslicer. Electrical stimulation was delivered at the white matter interface and extracellular field potentials were recorded from the superficial layers of the somatosensory cortex. Slices were then disinhibited with 10 μM BMI and the median number of negative field potentials per epileptic event (NFP/EE) was compared. In the absence of BMI, both normally laminated and dysplastic slices only produced a single negative field potential in response to stimulation. However when slightly disinhibited with BMI, control and experimental slices displayed epileptiform activity both in response to stimulation and spontaneously. While the total number of epileptiform events was not significantly different between groups, dysplastic slices displayed a greater number of NFP/EE (4.1 ± 1.03 vs. 1.6 ± 0.4 for evoked events and 5.1 ± 1.2 vs. 1.5 ± 0.5 for spontaneous events).

Following the finding of *in vitro* hyperexcitability of *in utero* irradiated cortical slices by Roper et al. (1997), subsequent studies began to seek out the underlying mechanisms responsible. These studies primarily have focused on examining the differences in neuron distributions and the intrinsic cellular properties of neurons in dysplastic cortex.

Neuron distributions

Since many theories of epileptogenesis are based on an imbalance in the normal distribution of excitatory and inhibitory neurons and their connections, Roper et al. (1999) proceeded to measure the excitatory/inhibitory neuron distribution in dysplastic slices. The experimental group was created by *in utero* irradiation to 225 cGy of radiation on day E17. Controls and animals were sacrificed as adults (age > P90), and immunohistochemical studies were performed on brain slices. Results were consistent with previous studies (McGrath et al., 1956; Cowen et al., 1970; Roper et al., 1995; Roper, 1998), with experimental animals displaying features including cortical dysplasia, a thinned neocortex lacking lamination, subcortical grey matter, heterotopic neurons, heterotopic neurons in the hippocampus, and absence of the corpus callosum. After application of staining techniques, it was found that two types of cortical inhibitory neurons (interneurons) were reduced by 40 – 50% in irradiated animals, but that overall neuron density was unchanged. These data suggested that interneurons are preferentially reduced by *in utero* irradiation.

Deukmedjian et al. (2004) performed a follow-up study aimed at better understanding the progression by which the irradiation protocol preferentially reduced the neocortical GABAergic system. To chart the process of the reduction, experimental animals exposed to 225 cGy of radiation on day E17 and controls were examined using immunohistochemical techniques at two different time points: E21 and P6. In irradiated rats, the total number of neurons was about 50% of controls at both time points. During the time interval, the total number of neurons doubled in both groups. Surprisingly, during the doubling, the distribution of neurons changed. While GABAergic neurons increased by an order of magnitude in control animals, no change was reported in

irradiated animals. This led to a drastic shift in the distribution of inhibitory neurons in the experimental group, from 18% at E21, down to 9% at P6. Thus, it seems neocortical GABAergic neurons are less capable at recovering from radiation-induced injury.

Functional differences of neurons in radiation induced dysplastic cortex

More recent studies have been focused on identifying the functional differences of neurons in *in utero* radiation induced dysplastic cortex. Zhu and Roper (2000) performed the first of such studies. Spontaneous events and evoked responses were obtained from pyramidal neurons in neocortical slices from control and rats irradiated with 225 cGy at E17 using whole-cell techniques. Spontaneous IPSCs (sIPSCs), miniature IPSCs (mIPSCs), sEPSC, and mEPSCs were examined and illustrated several functional changes leading to reduced inhibition in the dysplastic cortex. First, both the amplitude and frequency of sIPSCs were reduced, 35% and 70% respectively in dysplastic cortical neurons. However the decay time constant and 10 – 90% rise times were unchanged between the groups. Second, the frequency of mIPSCs was reduced in dysplastic cortex by 86%. Third, monosynaptic evoked IPSCs in dysplastic cortex showed a 48% decrease in mean maximal amplitude compared to controls. Fourth, evoked EPSCs from dysplastic cortex showed both greater peak amplitude and averaged area than controls. Finally, spontaneous EPSC in dysplastic cortex showed a 42% increase in amplitude and 77% increase in frequency. Combined, these data show considerable inhibitory system impairment in the *in utero* radiation induced cortex.

A follow-up study conducted by Chen and Roper (2003) examined the properties of heterotopic cortex, gray matter residing deep within the subcortical white matter of irradiated slices, and corroborated the selective impairment of the inhibitory system in

dysplastic cortex. Whole-cell voltage clamp recordings showed a similar reduction in the average frequency of sIPSCs in heterotopic cortex compared to normal pyramidal neurons in layer II/III (4.1 ± 0.4 Hz vs. 7.4 ± 0.6 Hz) (Zhu and Roper, 2000). However, sIPSC amplitudes and kinetic properties, such as 10 – 90% rise times, were not significantly different between groups. Similarly to sIPSCs, the frequency of mIPSCs was also reduced in dysplastic cortex (2.2 ± 0.4 Hz vs. 3.3 ± 0.3 Hz), while the amplitude and kinetic properties were unchanged.

Differences in short-term plasticity in inhibitory and excitatory neurons were also examined. This was done by stimulating near the cells with a 5-pulse train at 10 or 20 Hz and observing the response. The IPSC responses evoked from cells at 10 Hz behaved similarly in both groups and depressed over successive pulses in the train. However, the EPSC responses evoked at 20 Hz differed. In control cortex, successive EPSC responses were greater than the first response, with the second pulse in the train causing the largest amplitude response, while in dysplastic cortex subsequent responses gradually decreased in amplitude. While this study effectively demonstrates impairment in the function of interneurons on pyramidal neurons in heterotopic cortex, it was unable to tell if it was due to a decreased number of interneurons or other changes in presynaptic release mechanisms.

Subsequent studies have continued to illustrate the intrinsic differences between individual neurons in *in utero* irradiate rats and controls. These differences include a decreased response of interneurons to excitatory drive (Xiang et al., 2006; Zhou et al., 2009) and supporting evidence for arrested neuron development (Chen et al., 2007).

Objectives and Central Hypothesis

In order to further characterize the *in utero* irradiated rat model of cortical dysplasia for use in epilepsy research, a greater emphasis on network-level interactions must be given. In this study, I utilize MEAs to analyze spontaneous epileptiform discharges in cortical slices from animals exposed *in utero* to one of two different radiation doses on E18 and compare results with normally laminated slices. By using MEAs to acquire electrophysiological data, both classic and novel statistical techniques, notably Granger Causality, can be utilized.

Through these techniques, I seek to achieve two main goals. First, since previous work devoted to studying the spatial properties of ictal propagation in acute rat cortical slices has focus solely on normally laminated slices, I aim to begin providing a comparable understanding about epileptiform activity in *in utero* radiation induced dysplastic slices. Second, utilizing new metrics, such as Granger Causality, I aim to gain deeper insight into the spatial regions driving ictal activity in both normally laminated and dysplastic cortical tissue. In particular, it is currently unknown whether the origination of ictal events, as defined by the location that has the first local field potential peak, is also the region responsible for driving the ictal event. The answer to this question potentially has high clinical relevance, since methods of surgical resection in cases of intractable epilepsy often focus removal of the seizure initiation site localized by scalp or sub cranial EEG recordings. Due to the poor surgical outcomes in cases of intractable neocortical epilepsy unless the entire dysplastic region is removed, I hypothesize that the location of ictal initiation does not coincide spatially with the location responsible for driving the ictal event.

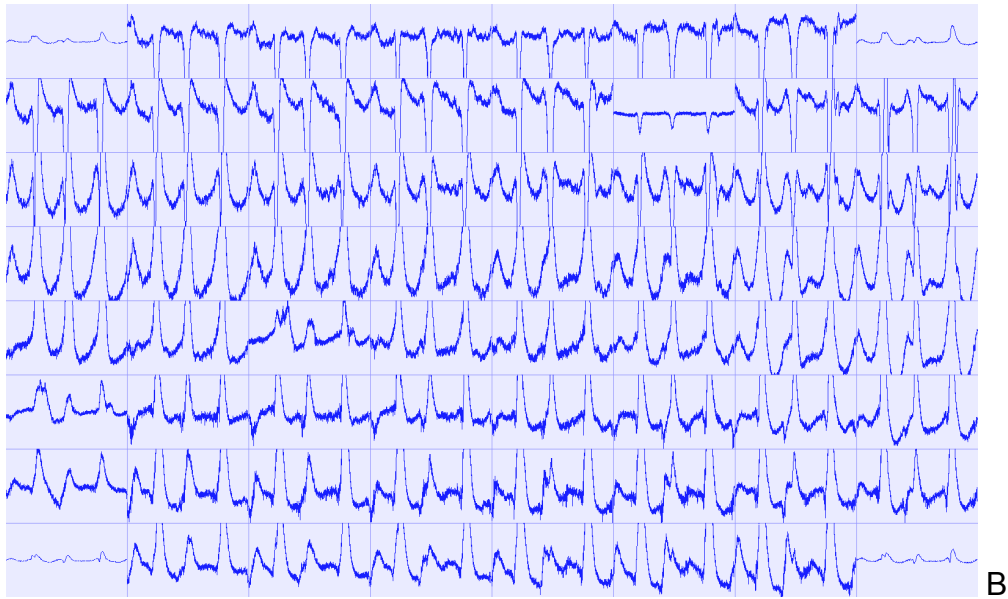
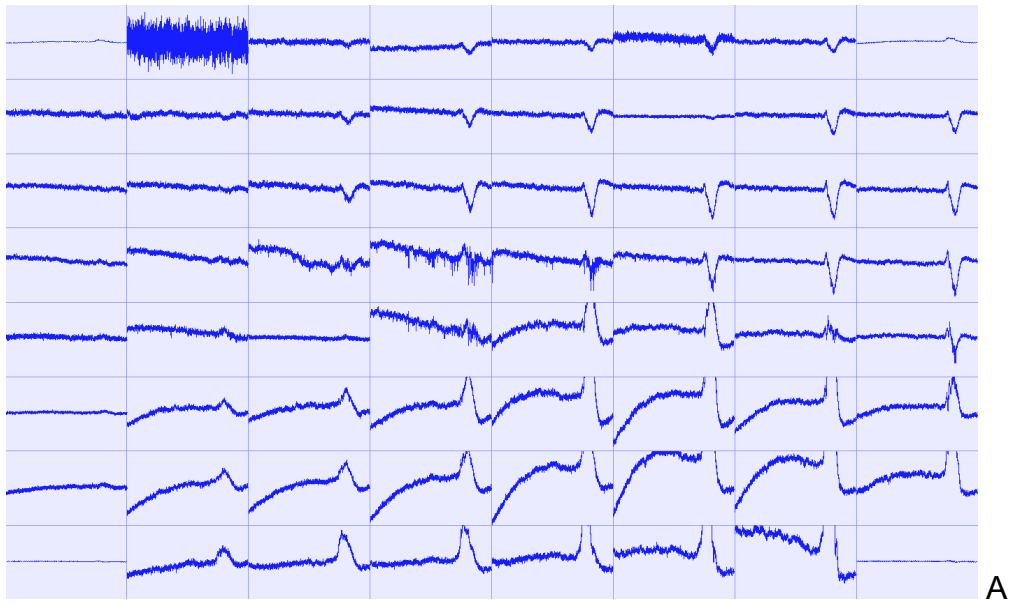


Figure 1-1. Data collected in the DeMarse lab from acute rat cortical slices treated with 4-AP (140 μ M) and KCl (7.5 mM) using 60-channel 3D MEAs. A) Data recorded during an interictal period. Each window represents activity on one channel over the course of the previous second. The amplitude of each window is 150 μ V. This is an example of a spontaneous population spike recorded from multiple channels throughout the tissue with individual spikes embedded on four of the waveforms. B) Later during recording, the activity progresses to an ictal event. Time and amplitude scales the same as A.

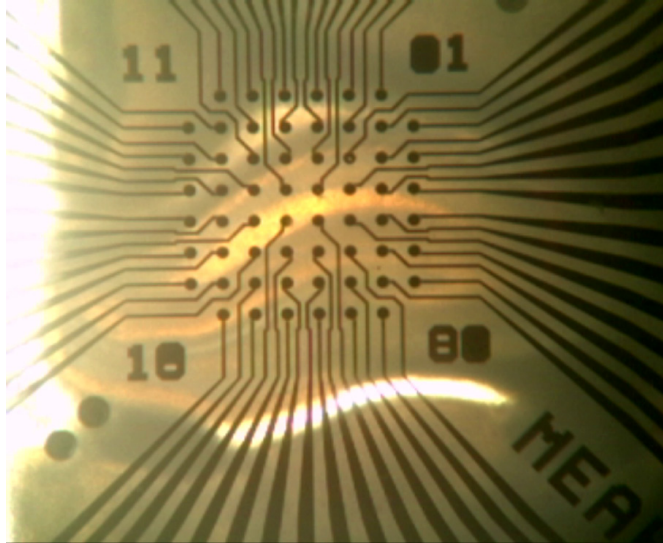


Figure 1-2. An acute rat hippocampal slice with CA1 and the dentate gyrus placed over the electrodes of an Ayuda Biosystems MEA60 200 3D. The electrodes are pyramid-shaped with a square base measuring $40\ \mu\text{m}$ by $40\ \mu\text{m}$, and have a height of 50 to $70\ \mu\text{m}$ with a center-to-center spacing of $200\ \mu\text{m}$.

CHAPTER 2 EXPERIMENT AND METRICS

Experimental Protocol

Animal acquisition, irradiation, housing, and brain slice preparation were performed by the Roper Laboratory (Epilepsy Neurophysiology Lab, University of Florida Department of Neurosurgery, Gainesville, FL) as previously described (Roper et al., 1997; Zhu and Roper, 2000; Chen et al., 2007) and is briefly discussed in the following text.

Animals and Irradiation Protocol

Timed pregnant Sprague Dawley rats were acquired from Harlan (Indianapolis, IN, U.S.). The day of insemination was designated as embryonic day 0 (E0). Pregnant rats were split into one control group and two experimental groups. The two experimental groups were further classified as either low dose irradiated or high dose irradiated. On E17, pregnant rats from the experimental groups were placed in a well ventilated acrylic glass (poly(methyl methacrylate)) box and exposed to either 145 cGy or 225 cGy, corresponding to low dose or high dose respectively, of external radiation from a linear accelerator source. Otherwise, all litters were housed identically.

Offspring were born naturally and weaned on postnatal day 21 (P21). All animals were kept on 12-hour dark/light cycles and received food and water ad libitum. All procedures followed guidelines approved by the Institutional Animal Care and Use Committee at the University of Florida.

Brain Slice Preparation

Rats were anesthetized via isoflurane inhalation and sacrificed by decapitation. Their brains were quickly removed and placed in chilled (0-4 °C) dissection artificial

cerebrospinal fluid (ACSF) thoroughly saturated with 95% O₂ and 5% CO₂ (carbogen) and containing the following solute concentrations in mM: 124 NaCl, 2.5 KCl, 1.25 NaH₂PO₄, 6.0 MgSO₄, 1.0 CaCl₂, 26.2 NaHCO₃, 10.0 glucose. A low potassium concentration and high magnesium concentration were chosen to block activity during dissection and slicing.

Brains were allowed to cool for approximately 90 seconds and then were removed from the dissection ACSF, affixed to a Vibratome (Leica VT1000s, Leica Microsystems, Wetzlar, Germany) stage with superglue, and covered with chilled carbogen saturated dissection ACSF. Coronal brain slices (400 µm thick) were taken from 8.7 to 4.8 mm anterior to the interaural line (Paxinos and Watson, 1997), which contains motor and somatosensory cortex (Lehohla et al., 2000). Finally, slices were allowed to equilibrate in room temperature (~22 °C) dissection ACSF constantly oxygenated with carbogen for at least 1 hour prior to recording.

Following slice equilibration, slices were bisected along the medial longitudinal fissure and individually transferred to a 3D MEA (Ayanda Biosystems, Lausanne, Switzerland) and positioned under visual guidance using an inverted microscope (Nikon Eclipse TS100, Nikon Instruments Inc., Melville, New York) so that the electrodes were beneath the cortical layers. Recording locations ranged medially from M2, the secondary motor cortex, to the barrel field of the primary somatosensory cortex

After tissue positioning, a mesh harp (ALA Scientific Instruments, Farmingdale, New York) was placed on top of the slice to increase slice contact with the electrodes and prevent slice movement during recording. The MEA was then placed into the recording system (MEA1060, Multichannel Systems, Reutlingen, Germany). Carbogen

saturated and warmed (35 °C) recording ACSF containing the following solute concentrations in mM: 124 NaCl, 5.0 KCl, 1.25 NaH₂PO₄, 0.5 MgSO₄, 2.0 CaCl₂, 26.2 NaHCO₃, 10 glucose, and 0.14 4-aminopyridine (4-AP), was continuously perfused into the MEA recording chamber at a rate of 2-3 ml/min via a microfluid chamber level controller (LevelLock LL-2, ALA Scientific Instruments). Increased K⁺ and Ca²⁺ concentrations, decreased Mg²⁺ concentration, and 4-AP were administered in the recording ACSF to encourage spontaneous epileptiform activity, which is uncommon in submerged slice preparations (D'Arcangelo et al., 2001; Meierkord et al., 1997).

Recording

A ground electrode was connected to the system and submerged in the MEA recording chamber. Electrophysiological signals were amplified, band pass filtered from 1 Hz - 10 KHz, and digitized by a data acquisition card (Multichannel Systems, MEA1060BC, Reutlingen, Germany) at a sampling rate of 25 kHz with 12 bit resolution. Real-time monitoring of voltages on all 60 channels was performed using internally developed software built upon the Open Source MEABench suite (Wagenaar et al., 2005). Recordings were started immediately upon the onset of the first ictal event for each slice and continued for at least 15 minutes. However, if an ictal event was not observed within 20 minutes, the slice was discarded. In total, data from 11 slices from 7 control animals, 7 slices from 4 low dose animals, and 11 slices from 5 high dose animals, ranging in age from P12 to P32 (median age P19), were analyzed.

Post Processing and Data Analysis

After recording, the raw signals were post processed by software to identify and separate ictal events into a single file for each slice. Information stored for each ictal event included: time of the event, the channel that triggered the event, the length of the

event, and voltages throughout the event at the 60 electrodes. To detect ictal events, a voltage threshold of 2.8 – 3.5 times the standard deviation of the mean voltage measured in the absence of activity was used. If at any time any channel had a voltage exceeding the threshold for more than 150 ms, a local field potential (LFP) event was declared on that channel and data from 100 ms prior to the time of peak voltage and 500 ms after was collected. During the 500 ms after the peak other LFP events could occur. If three or more contiguous LFP events were detected an ictal event was declared. Recording of the ictal continued until no LFPs had occurred for 500 ms. At this time, the end of the ictal event was declared and the event was stored to disk. Figure 2-1 gives a visual representation of the automated post-processing algorithm. After automated post processing, data from every channel of each ictal event was plotted with custom software written in Objective-C and verified by visual inspection to be genuine. Events were required to have at least three successive super-threshold peaks on at least one channel to distinguish them from LFPs. Since ictal events were typically measured simultaneously across the entire 8x8 electrode grid they were easy to distinguish. Events that were erroneously classified as ictal events (e.g.: electrical noise produced by the perfusion system) by the automated program due to recording artifacts or that did not have at least three successive super-threshold peaks were removed from analysis. Subsequent data processing and analysis was performed using programs written in MATLAB and Objective-C.

Definition of Metrics

The two questions that I aim to answer are, “What are the differences between *in vitro* cortical ictal, or seizure-like, activity in control and irradiated animals?” and, “Does the initiation site of ictal events coincide spatially with the region driving ictal activity?”

In order to answer these questions, a set of metrics must be defined to measure and quantify the ictal activity recorded. I first present a simple test to ascertain if the slice activity is stable with respect to time. This simple test provides a solid foundation necessary for all subsequent qualitative and quantitative analysis performed. Next, I present the actual metrics, which are subdivided into three groups based upon their use by previous researchers and their complexity. First, I introduce and define a set of classic metrics used by previous researchers that do not incorporate spatial or topological information and do not vary over time. Second, I progress to more complex metrics, which capitalize on the rich spatial information about the slice provided by the MEAs. Finally, I present a brief overview of Granger Causality and its application to quantifying causal interactions during propagation within and across the cortical layers during ictal events.

Verification of Slice Stationarity

In order for any of the metrics or statistical analysis performed to have meaningful results, the electrophysiological activity of the slice must be stable with respect to time. This is especially important for metrics that depend on temporal components. If electrophysiological activity is not sufficiently stable over the recording period, results from statistical analysis will become meaningless.

Specifically, two important scenarios exist which could invalidate temporally dependent metrics. First, there is an amount of time the recording solution, which contains 4-AP, an elevated KCl concentration, decreased Mg^{2+} concentration, and is heated to 35 °C, must sufficiently “wash in” the tissue and begin to have a physiological effect. This could cause an increase in activity during the wash-in period. Second, gradual cell/slice death over the course of the recording could result in a decrease in

activity over the course of the recording. In order to ensure that neither of these phenomena plays a significant role, two provisions were made.

The first provision was the experimental protocol, which was designed to mitigate the effects of “wash-in”. Recording was only started after the first observed ictal event. This typically took between 5 and 15 minutes. I modeled the change in concentrations of solutes in the recording chamber by assuming the chamber initially held 1 ml of dissection ACSF, the average in and out flow rates were 2.5 ml/minute, and the fluids mixed perfectly. Next, I constructed a differential equation based on these assumptions to approximate the solute concentrations in the recording chamber over time as follows:

The number of moles of solute in chamber at time t is equal to the initial number of moles plus the amount of solute flowed in at time t minus the amount of solute flowed out at time t . This gives Eq. 2-1, the general differential equation for recording chamber solute concentration as a function of time.

$$C'(t) = [\text{solute}]_{\text{in}} - \text{flow}_{\text{out}} * C(t) \quad (2-1)$$

where $C'(t)$ is the change in the number of moles of solute in the chamber with respect to time, $[\text{solute}]_{\text{in}}$ is the number of moles of solute flowing into the chamber per minute, flow_{out} is the number of moles leaving the chamber per minute, and $C(t)$ is the number of moles of solute in the chamber at time t .

For 4-AP, the specific equation is

$$C'(t)_{4\text{-AP}} = 0.35 * 10^{-6} - 2.5 * C(t)_{4\text{-AP}}$$

with an initial condition of

$$C(0) = 0$$

Using the general solution method gives

$$C(t)_{4-AP} = e^{-2.5*t} (\int 0.35 * 10^{-6} * e^{2.5*t} dt + k)$$

Solving the indefinite integral gives

$$C(t)_{4-AP} = e^{-2.5*t} (0.14 * 10^{-6} * e^{2.5*t} + k) \quad (2-2)$$

Reducing Eq. 2-2 yields

$$C(t)_{4-AP} = 0.14 * 10^{-6} + k * e^{2.5*t}$$

Finally, solving for the constant k using the initial condition produces

$$C(t)_{4-AP} = 0.14 * 10^{-6} * (1 - e^{2.5*t})$$

Similarly, Eq. 2-3 through Eq. 2-5 gives the amount of K^+ , Mg^{2+} , and Ca^{2+} present in the chamber at a given time, respectively.

$$C(t)_{K^+} = (-2.5 * e^{-2.5*t} + 5.0) * 10^{-6} \quad (2-3)$$

$$C(t)_{Mg^{2+}} = (5.5 * e^{-2.5*t} + 0.5) * 10^{-6} \quad (2-4)$$

$$C(t)_{Ca^{2+}} = -0.00025 * e^{-2.5*t} + 0.000005 \quad (2-5)$$

Using these equations to plot the concentration of each solute as a function of time gives the graphs shown in Figure 2-2.

In the case of Mg^{2+} , which has the longest delay, the chamber concentration reaches within 5% of the final concentration within 131 seconds and within 0.5% of the final concentration within 186 seconds. This shows that complete wash-in should be completed well before the 5 – 15 minutes before the first ictal event is observed and recording is started.

The second provision made to ensure that wash-in and necrosis had no appreciable effect was examining the rate at which ictal events occurred over time. It is hypothesized that ictal events should occur more or less linearly over time. The ictal event number versus event start time for each recording was plotted and a linear fit was

performed to ascertain the level of linearity. An initial, rapid increase in activity could be attributed to wash-in, while a gradual decline throughout or rapid decline in activity later in longer recordings could be attributed to necrosis. Should such an increase or decrease in activity be seen, data from only the linear region should be included for further statistical analysis (e.g.: after any rapid initial activity increase and before any noted activity decrease).

Classical and Non-Spatial Metrics

Ictal events per recording time

The first, and most fundamental metric used is the number of ictal events per unit of recording time. For the purposes of this document, an ictal event or ictal is defined as at least three consecutive local field potentials (LFPs) exceeding 3.2 standard deviations above the noise floor recorded on at least one of the sixty channels and includes 100 ms before the first LFP breaks the threshold and continues 500 ms after the activity levels return to the noise floor. Since recording lengths vary between slices, normalizing by recording length is necessary.

This metric has widespread use and has been used by previous researchers to characterize epileptiform activity in different *in vitro* models (Gulyás-Kovács et al., 2002), compare the effectiveness of protocols aimed at mitigating spontaneous ictal activity in slice (Albensi et al., 2004), and quantify the increased hyperexcitability caused by cortical dysplasia (Kondo et al., 2001; Zhou et al., 2009).

In this study, an elevation in the number of ictal events per time is expected with dysplastic slices, due to a loss of laminar structure and regulatory inhibition networks, thus lowering the ictal threshold and allowing for more synchronous activity to occur.

Further, in line with results reported by Kellinghaus et al. (2004), it is expected that low dose irradiated subjects will have a greater increase than high dose irradiated subjects.

Average event length

Employed by previous researchers to quantify the effectiveness of various pharmacological and electrical stimulation protocols aimed at lessening epileptiform activity, the average event length is the second fundamental metric used to quantify electrophysiological activity differences between groups (D'Arcangelo et al., 2005; D'Antuono et al., 2002; de Guzman et al., 2008). Dysplastic slices are expected to have a longer average event length, due to loss of regular morphology and impeding inhibitory networks that would normally terminate synchronous events.

Distribution of event lengths

Expanding further on the average event length metric, I present histograms of event lengths, normalized by recording time. This provides a more descriptive metric than average event length, since information about the presence of clusters of event lengths would be hidden by a simple average. Decreased inhibition is expected to lead to distributions tending towards longer event lengths in irradiated subjects as compared to control subjects.

Average burst integral

The epileptiform field potential (EFP) burst integral has been used to quantify the hyperexcitability of dysplastic cortex due to freeze lesioning in the rat model (Kellinghaus et al., 2007) and human patients (Möddel et al., 2005). This metric was employed using data collected from intracellular methods and is dependent on the amplitude of the signals collected. Since our protocol used extracellular recording techniques, namely 3-D MEAs, to acquire electrophysiological signals, this metric becomes less reliable.

Amplitude variations arise due to a number of factors, including differences in slice placement on the array, tissue contact with the 3-D electrodes, thickness of the insulating dead-cell layer caused by the tissue slicing process, and distances between active neuron populations and the electrodes. Due to the average burst integral's reliance on uniform signal amplitude collection and variability in this due to our experimental protocol, I chose not to include incorporate this metric into our analysis.

Average inter-event interval

The inter-burst interval (IBI) metric is frequently used by *in vitro* experimenters using dissociated cultures and computer models (Canepari et al., 1997; Chiappalone et al., 2003; Chiappalone et al., 2006), and it has been adapted by researchers using acute slices (Slutzky et al., 2001; Slutzky et al., 2003) and *in vivo* experiments with EEG (van Putten and van Putten, 2007). In this study, I define the IBI as the length of time between the end of one ictal event and the beginning of the next. Due to cortical dysplasia leading to a loss of inhibition, normal oscillatory activity, which normally would terminate via inhibitory networks, are expected to more effectively recruit neuron ensembles, resulting in a lower IBI for irradiated subjects. Further, it is hypothesized that the mean IBI from the low dose group will be shorter than the mean IBI from the high dose group.

Distribution of inter-event intervals

Also expanding on the average IBI metric, I present histograms of IBI lengths, normalized by recording time. This provides a more descriptive metric than average IBI length, since information about the presence of clusters IBI lengths would be hidden by a simple average. Decreased inhibition is expected to lead to distributions tending towards shorter IBIs in irradiated subjects as compared to control subjects. Further, it is

anticipated that the IBI distribution from the low dose group will tend towards shorter lengths than the high dose group.

Recovery ratio

Tying event duration and IBIs together, I seek to quantify the “recovery ratio” after an ictal event. I define the recovery ratio as the inter-event interval divided by the duration of the immediately preceding event. I expect three main trends in the recovery ratio. First, it is expected that longer events will be followed by a longer IBI, due to depletion of neurotransmitters. Second, it is hypothesized that due to loss of lamination and inhibitory networks, irradiated subjects will, in general, have a decreased recovery ratio. Finally, I expect a larger decrease in recovery ratios from low dose group than recovery ratios from the high dose group.

Number of local field potentials per epileptic event

Modifying the number of negative field potentials (NFP) and NFP per epileptic event (NFP/EE) metrics previously employed by researchers such as Roper et al. (1997), I developed MATLAB software based on the public domain peakdet program (Billauer, www.billauer.co.il) to down sample the signals from 25 kHz to 250 Hz and then count the number of positive and negative local field potentials appearing on each channel during each ictal event to assess if there are differences between experimental and control groups. Due to previous studies, I expect to find a greater number of field potentials per ictal event in dysplastic tissue (Roper et al., 1997).

Spatial Metrics

A great deal of research has been devoted to exploring the spatial properties of seizure like activity in acute rat cortical and hippocampal slices. However, this previous work has focused solely on normally laminated tissue. Here I describe the previously

used and expanded spatial metrics I applied to normally laminated and dysplastic cortical slices to compare seizure like events.

Initiation site

Previous studies using 1-D electrode arrays and optical imaging have shown that the initiation for spontaneous epileptiform activity is a localized process usually constrained to a few localized groups of neurons in layer V of the neocortex with most preparations (Flint and Connors, 1996). Further, literature reports conflicting views on the existence of dominant initiation foci. Some researchers indicate that there is no dominant initiation site (Jimbo and Robinson, 2000), while others claim that typically two or three initiation foci exist and the dominant foci changes over time (Tsau et al., 1998). Here, I denote the initiation location as the first channel to reach its first peak in each ictal event. It is anticipated that control slices will have a few dominant initiation foci contained chiefly in the lower cortical layers, while the irradiated slices will have a greater number of initiation foci spread throughout cortical layers due to loss of lamination.

Ictal wave propagation speeds and pattern

Modifying metrics employed by previous researchers (Bakker et al., 2009; Chervin et al., 1988; Demir et al., 1999; Golomb and Amitai, 1997; Pinto et al., 2005), I analyzed the propagation of ictal activity through the tissue. This was done quantitatively by calculating wave propagation velocities through the tissue slices both horizontally through layers and vertically across layers. Further, I qualitatively analyzed wave propagation patterns originating from dominant initiation foci using color gradients generated from event first peak times. Results from these metrics were then compared between groups.

Termination site

Previously examined in normally laminated slices by Pinto et al. (2005) using a linear array of electrodes, I define the termination site as the electrode with the last peak in an ictal event. In accordance with the findings of Pinto et al., I expect termination to be confined to a few foci in the upper layers in normally laminated slices. As with event initiation, due to loss of lamination in dysplastic slices, I expect less regular termination sites as compared to control subjects.

New Metrics

Overview of Granger Causality

While classic and spatial metrics allow for characterization of ictal events, it is possible that these observations are the result of more complex and unobserved underlying processes. For instance, although a dominant initiation focus may be present in a slice, this may not be the location actually driving the seizure event. This has particular clinical relevance in cases of intractable epilepsy where surgical resection of brain tissue is employed. Therefore, it is desirable to utilize a technique, such as Granger Causality, that allows analysis into underlying processes.

Although originally used for economic data, Granger Causality has gained significant traction in the neuroscience community over the last half decade. Specifically, it has been most attractive in instances where researchers wish to gain greater insight into causal interactions between neuron populations or brain region in behaving animal or human subjects and where experimental physical or ethical boundaries limit data collection to EEG or MRI (Goebel et al., 2003; Hesse et al., 2003; Bollimunta et al., 2008; Roebroek et al., 2005; Roebroek et al., 2009).

First, it provides a mathematical quantification of causal relationships, providing an effective means to compare the strength of causal interactions among groups. Secondly, it separates causal relationships from merely coincidental occurrences. Third, using an improved technique, known as conditional Granger causality, it allows for the elimination of mediating and confounding influences.

The fundamental idea behind Granger Causality can be tracked back to Wiener (1956). He proposed, given two simultaneously measured time series A and B, that A can be said to be causal to B if past information about A allows a more accurate prediction about the future behavior of B. Granger later formalized this idea in 1969 (Granger, 1969) for linear regression models of stochastic processes. This is accomplished by evaluating whether or not the variance of the prediction error for B at the present time is reduced by including past measurements from A in a linear regression model. If it is reduced, then A is said to have a causal, direct, or driving influence on B. Granger Causality analysis has three main advantages over traditional cross-correlation metrics. First, GC is less sensitive to changes in overall activity rate. Second, it provides a directional measure of the “causal” influence, whereas cross-correlation does not. Finally, GC may require less data to successfully complete a meaningful analysis.

Pairwise Granger Causality

Here I present an overview of the mathematical underpinnings of Pairwise Granger Causality in both the time and frequency domains which closely follows the Geweke (1982; 1984) and Ding et al. (2006) treatment of the subject matter.

We begin with autoregressive (AR) modeling of neural time series. Consider two simultaneously acquired stationary time series: X , given by X_1, X_2, \dots, X_n , and Y , given by Y_1, Y_2, \dots, Y_n . The single variable autoregressive (SVAR) model representations of these time series based on p previous samples can be given by:

$$X(t) = \sum_{j=1}^p a_x(j)X(t-j) + \varepsilon_t$$

$$Y(t) = \sum_{j=1}^p a_y(j)Y(t-j) + \varepsilon_t$$

where the variance of each error series, $\varepsilon_{X(t)}$ and $\varepsilon_{Y(t)}$ respectively, is a measure of the linear prediction accuracy. Combining these into a bivariate autoregressive (MVAR) model, $W(t)$, where X and Y are calculated on previous values of both time series gives

$$W(t) = \begin{pmatrix} X(t) = \sum_{j=1}^p a_{XX}(j)X(t-j) + \sum_{j=1}^p a_{XY}(j)Y(t-j) + \eta_t \\ Y(t) = \sum_{j=1}^p a_{YX}(j)Y(t-j) + \sum_{j=1}^p a_{YY}(j)Y(t-j) + \gamma_t \end{pmatrix} \quad (2-6)$$

Using Wiener's idea, Granger formulated that if the X prediction is improved by using past information about the Y series, then Y can be said to have a "causal" influence on the X time series. This influence can be quantified by

$$F_{Y \rightarrow X} = \ln \frac{\text{var}(\varepsilon_t)}{\text{var}(\eta_t)}$$

The variance of the prediction error for the AR model of X is compared to the variance of the prediction error when Y is included in the model. Evaluating whether or not there is a causal influence in the opposite direction, from X to Y , merely requires reversing the roles of the two time series.

Since natural time series, such as economic data, contains oscillatory components, Geweke (1982; 1984) later developed the mechanics to handle a spectral version of Granger Causality, thus allowing the quantification of causal influences at specific frequencies. This method compares the power of a time series generated by the stochastic processes intrinsic to that time series, or its intrinsic power, to the total power of the same time series. Since the total power of the time series includes any causal influences from other time series in the frequency domain, there may be a difference in the intrinsic power and total power. Thus, when no causal influence exists upon the time series, the total power is equal to the intrinsic power and the log ratio of the total to intrinsic power is equal to zero.

Before being able to compare the total and intrinsic powers of a time series, a number of steps must be taken. In order to generate the frequency domain function $W(f)$, a Fourier transform is performed on the MVAR $W(t)$ defined in Eq. 2-6 yields, and yields

$$A(f)W(f) = E(f) \quad (2-7)$$

where $A(f)$ is the spectral coefficient matrix and $E(f)$ is the spectral noise vector resulting from the Fourier transform. Next, Eq. 2-7 is rearranged by setting the transfer function $H(f)$ equal to $A(f)^{-1}$, which produces

$$W(f) = H(f)E(f)$$

Next, the spectral matrix $S(f)$, containing the auto spectra and cross spectra of $W(t)$, can be calculated, as shown in Eq. 2-8.

$$S(f) = H(f)\Sigma_3 H^*(f) \quad (2-8)$$

Where $H^*(f)$ is the transpose and conjugate of $H(f)$ and Σ_3 is the covariance matrix of the noise terms from $W(t)$.

Spectral Granger causality is based upon decomposing the total power (variance) of a given frequency f for one time series into the sum of the intrinsic power and causal power from an influencing series. Each time a new spectral matrix is calculated in the same manner, except both sides of Eq. 2-7 are left multiplied by Geweke's normalization transform

$$P = \begin{pmatrix} 1 & 0 \\ -\frac{\text{cov}(\eta_t, \gamma_t)}{\text{var}(\eta_t)} & 1 \end{pmatrix}$$

The normalization transform isolates the intrinsic power of X by calculating the intrinsic power component of the total power separately from the causal power component (Geweke, 1982). The X component of the new transfer function, shown in Eq. (2-9), is then used to calculate the intrinsic power of the X time series.

$$\tilde{H}_{xx}(f) = H_{xx}(f) + \left(\frac{\text{cov}(\eta_t, \gamma_t)}{\text{var}(\eta_t)} \right) H_{xy}(f) \quad (2-9)$$

The Granger Causality spectrum is then calculated by taking the logarithm of the ratio of the total power over the intrinsic power

$$F_{y \rightarrow x}(f) = \ln \left(\frac{S_{xx}(f)}{\tilde{H}_{xx}(f) \text{var}(\eta_t) \tilde{H}_{xx}^*(f)} \right)$$

Finally, Using the value of the causality spectrum, it is then possible to evaluate how much of the variance of a signal at f is due to the second signal exerting a causal influence.

Conditional Granger Causality

While useful at determining connections between time-series, Pairwise Granger Causality (PWGC) has two notable limitations at ascertaining network topology, particularly in networks where mediated connections exist: false-positive connections and over estimated connection strengths. These shortcomings are illustrated in Figures 2-3 and 2-4.

Suppose I have the simple three-neuron network with connectivity as shown in Figure 2-3A. Neuron X is connected to Neuron Y and Neuron Y is connected to Neuron Z. No other connections exist. Performing a traditional PWGC Analysis on this network will likely describe the network shown in Figure 2-3B. The most obvious difference between the actual network and the one reconstructed through PWGC analysis is the erroneous direct connection from Neuron X to Neuron Z. This is due to the fact that Neuron X has a mediated connection to Neuron Z through Neuron Y. In other words, the firing of Neuron X induces Neuron Y to fire, which then induces Neuron Z to fire.

Secondly, in the PWGC reconstructed network, the connection strength between Neuron Y and Neuron Z is over estimated. This connection over-estimation is the sum of two components: the “actual” endogenous firing of Neuron Y causing Neuron Z to fire and the mediated connection from Neuron X to Z through Y, in which Neuron X fires, “evoking” a response from Neuron Y, causing Neuron Z to fire. False-positive connection inferences and over-estimated connection strengths are compounded in networks possessing a cascade of mediated connections, such as the network shown in Figure 2-4. As the length of the neuron chain increases, the estimated PWGC reconstructed connection weights towards the end of the chain approach 1.

In order to tease out these mediated connections, a modification of PWGC Analysis, known as Conditional Granger Causality (CGC) Analysis, which can identify and remove mediated connections erroneously interpreted as direct connections, can be performed. Algorithms have been developed to perform this analysis in both the time and frequency domains (Ding et al., 2006). For brevity, I only present the time domain case and use the simple three-neuron network shown in Figure 2-3A for our discussion. In the time-domain, CGC compares the prediction of Z including Y in a bivariate MVAR model, $V(t)$ shown in Eq. 2-10, with the prediction of Z including Y and X in the trivariate MVAR model, $U(t)$ shown in Eq. 2-11.

$$V(t) = \begin{pmatrix} Y(t) = \sum_{j=1}^p a_{YZ}(j)Z(t-j) + \sum_{j=1}^p a_{YY}(j)Y(t-j) + \kappa_t \\ Z(t) = \sum_{j=1}^p a_{ZZ}(j)Z(t-j) + \sum_{j=1}^p a_{ZY}(j)Y(t-j) + \alpha_t \end{pmatrix} \quad (2-10)$$

$$U(t) = \begin{pmatrix} X(t) = \sum_{j=1}^p A_{xx}(j)X(t-j) + \sum_{j=1}^p A_{xy}(j)Y(t-j) + \sum_{j=1}^p A_{xz}(j)Z(t-j) + \lambda_t \\ Y(t) = \sum_{j=1}^p A_{yx}(j)X(t-j) + \sum_{j=1}^p A_{yy}(j)Y(t-j) + \sum_{j=1}^p A_{yz}(j)Z(t-j) + \mu_t \\ Z(t) = \sum_{j=1}^p A_{zx}(j)X(t-j) + \sum_{j=1}^p A_{zy}(j)Y(t-j) + \sum_{j=1}^p A_{zz}(j)Z(t-j) + \nu_t \end{pmatrix} \quad (2-11)$$

Since the influence of Neuron X on Neuron Z is entirely mediated through Neuron Y, the trivariate model prediction of Z is no more accurate than the bivariate model. This is determined by taking the log of the ratio of the variance of the prediction error of Z from $V(t)$ to the prediction error of Z from $U(t)$ and is shown in Eq. 2-12.

$$F_{Y \rightarrow Z|X} = \ln \frac{\text{var}(\alpha_t)}{\text{var}(\nu_t)} \quad (2-12)$$

Thus yielding a value of zero in the case where the influence of Neuron X on Neuron Z is completely mediated through Neuron Y, but a value greater than zero when Neuron X has a direct, non-mediated influence on Neuron Z.

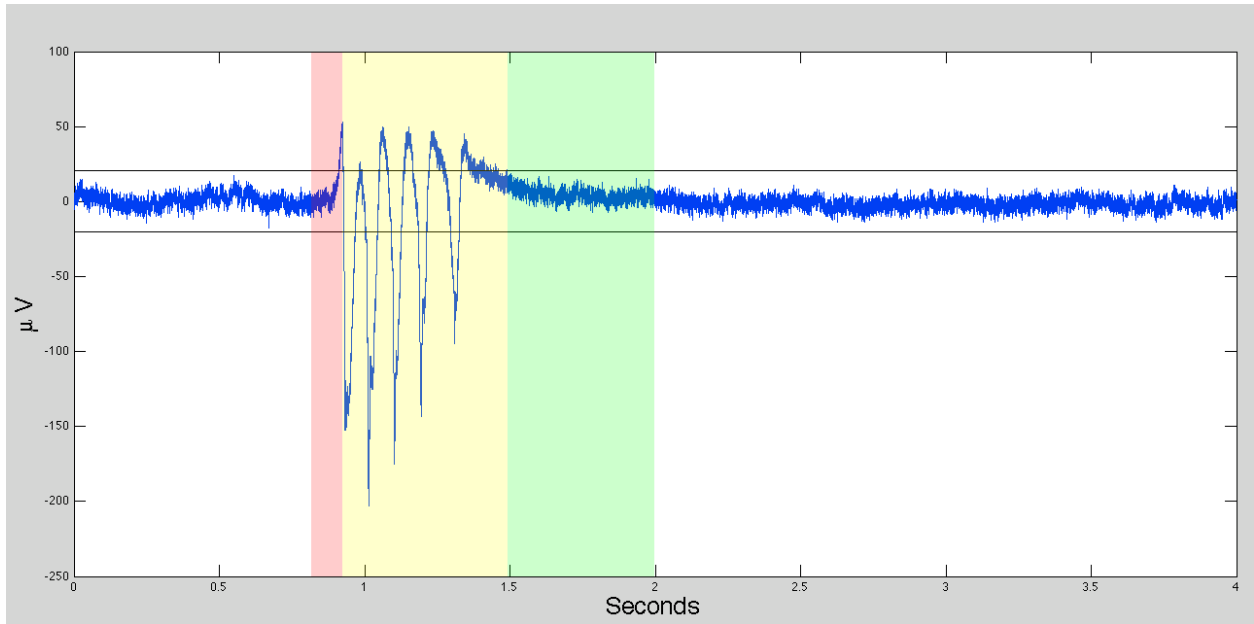


Figure 2-1. Visual representation of the automated post-processing algorithm. Here four seconds from one channel of raw data in which an ictal event occurred is plotted. The two black horizontal lines centered about 0 μV are the thresholds. Together, the three shaded areas represent the packaged ictal event. The red-yellow interface is the peak of the threshold-crossing event. The red area denotes 100 ms of data prior to the event peak that is collected, yellow represents the main part of the event, and green is the last 500 ms of data collected after the voltage on the channel returns within threshold.

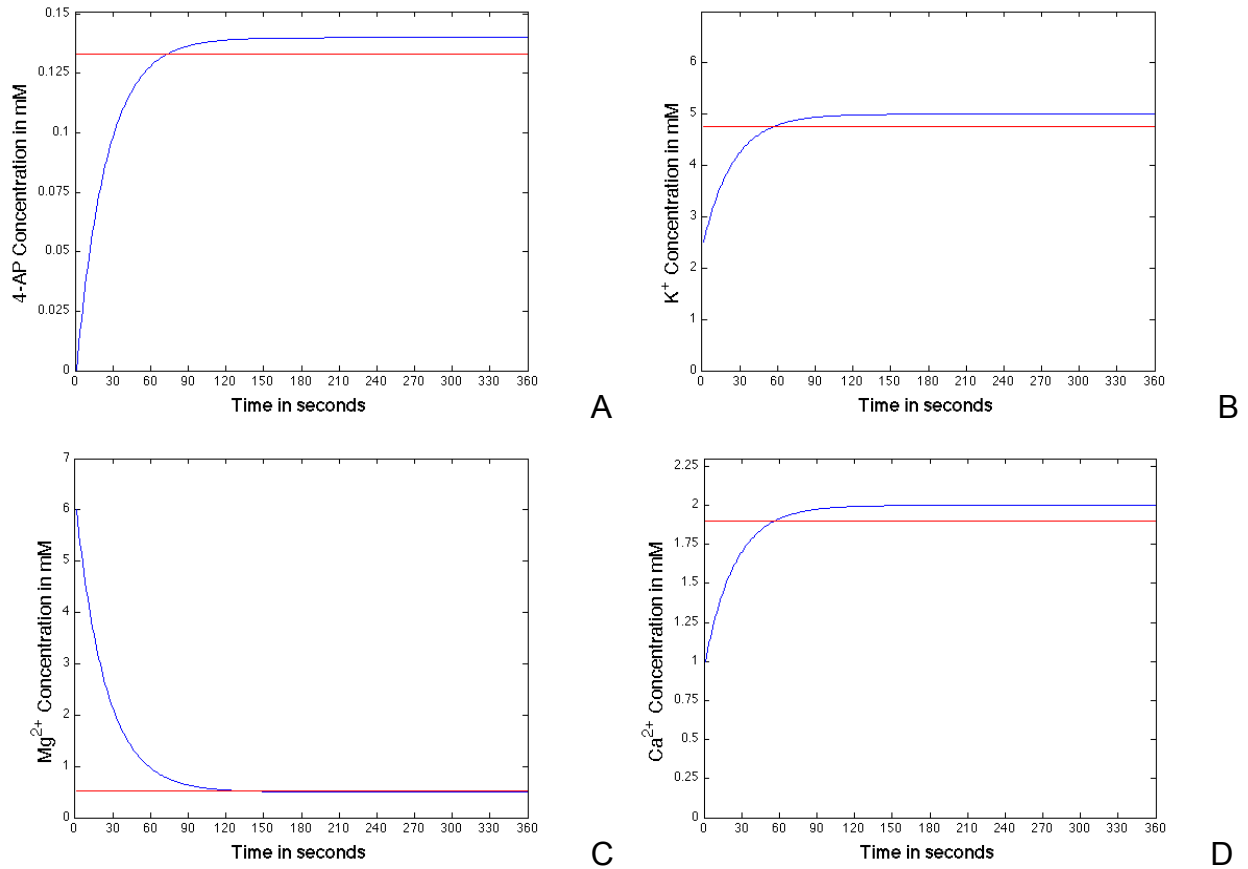


Figure 2-2. Concentration of solutes in the recording chamber vs. time. Since the concentrations of some solutes differ between the dissection and recording ACSF, there is a delay at the beginning of each experiment when the recording fluid is “washing in”. Blue indicates the solute concentration within the recording chamber and the red indicates a concentration within 5% of the final concentration. A) 4-AP Concentration vs. Time, B) K⁺ Concentration vs. Time, C) Mg²⁺ Concentration vs. Time, and D) Ca²⁺ Concentration vs. Time

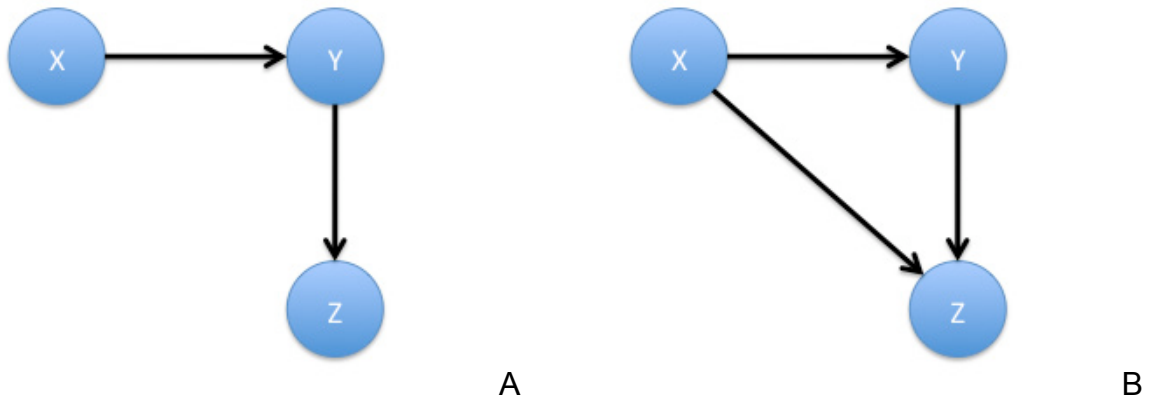


Figure 2-3. Example of an erroneous direct causal connection generated by Pairwise Granger Causality on a network in which a mediated connection exists. A) The actual network possessing a mediated connection from Neuron X to Neuron Z through Neuron Y. B) The PWGC reconstructed network, which possesses an erroneous direct connection from Neuron X to Neuron Z due to the aforementioned mediated connection. Note: differences in connection weights were omitted from B for clarity.

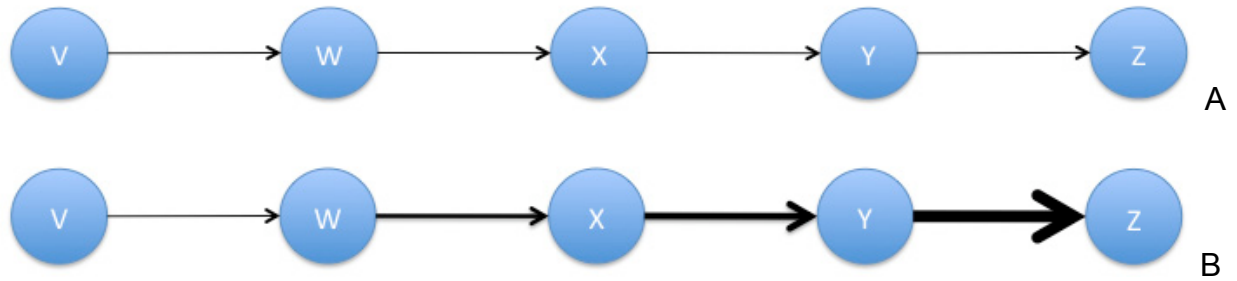


Figure 2-4. Example of erroneously increasing connection weights generated by PWGC in which a series of mediated connections exists. A) The actual “chain” network possessing a series of mediated connections from Neuron V to Neuron Z. B) The PWGC reconstructed network in which the connection weights are erroneously over emphasized progressively down the chain of mediated connections. Note: erroneous direct connections, as described in Figure 2-3, would also be inferred by PWGC but were omitted from B for clarity.

CHAPTER 3 VERIFICATION OF SLICE STABILITY

Although the experimental protocol was designed to limit the potential effects of chemical wash-in and tissue necrosis, and was validated with mathematical models in Chapter 2, further validation of the protocol is required to ensure that our subsequent statistical analysis will be meaningful. I verify slice stability by plotting the ictal event number versus the start time of the event. A linear trend is expected, indicating that the activity is stable—or stationary—with respect to time. However, if wash-in of K^+ or 4-AP and wash-out of Mg^{2+} is gradual, a super-linear trend of ictal onset would be observed. Additionally, if tissue slowly dies over the course of a recording session, a sub-linear trend would be observed.

Control Slice Stability

The stability of the control slices was first assessed. In order to evaluate stability, a series of three plots was generated from the electrophysiological data collected for each slice. Initially, the ictal event number was plotted versus the start time of the event using MATLAB. A simple linear fit was performed on the data and superimposed on the graph. One such plot, which is representative of the normally laminated control slices, is presented in Figure 3-1. As illustrated, the data show that the ictal events occur at a fairly regular, rhythmic rate. This indicates that wash-in of the recording ACSF and simultaneous wash-out of the dissection ACSF have no appreciable effect on the rate of ictal events.

While Figure 3-1 is representative of the data for nearly all of the control slices, one appears to have a change in ictal event generation rate over the course of the recording. Figure 3-2 presents this slice. The plot appears to consist of three linear

phases. The first phase occurs from 0 to 6 minutes. Beginning around 6 minutes into the recording, the slope of the linear trend appears to increase drastically. After approximately 2 minutes of this increased linear activity, a near instantaneous drop occurs where the frequency of ictal events returns to the earlier rate. This pattern warranted further investigation. The data from the recording were split into each of the three phases and analyzed separately. All three phases demonstrate linear trends. The slopes of the linear fits are 6.5, 25, and 7.6 for the first, second, and third phases, respectively. It is unlikely that this change of slope can be attributed to ACSF wash-in/wash-out for a number of reasons. First, although there is a marked change in slope between the phases, the trend within each phase is always linear. An effect from wash-in/wash-out and tissue necrosis would be expected to be an exponential rise early in the recording or asymptotic decrease late in the recording, respectively. Second, the increase in slope occurs after almost 5.5 minutes, well after the effect of wash-in/wash-out would be expected from the models discussed in Chapter 2. Third, the second change in slope reverts back to a state very similar to the first phase of the recording and does so after around the 7-minute mark. Tissue necrosis is unlikely after only 7 minutes. Finally, no other control slices display appreciable non-linear phases. Thus, it is unlikely that only one of 11 such slices is affected by these phenomena.

In order to further verify that the changes in linear slope demonstrated in Figure 3-2 were not attributable to wash-in/wash-out and tissue necrosis, two further plots were constructed. In addition to the rate of ictal event generation, the duration of ictal events could be modified by wash-in/wash-out and tissue necrosis. If these processes have an appreciable effect, ictal events durations should become longer during the period while

the dissection ACSF is replacing the recording ACSF. Additionally, as neurons die, ictal events should shorten in duration because a monotonically decreasing number of neurons would be able to sustain activity. To address this issue, I first plotted ictal event length vs. the event number; the results are shown in Figure 3-3. No reliable trend in ictal durations is evident from this plot. I also compared ictal event durations vs. ictal event start times; the results are shown in Figure 3-4. Although the rate of event generation elevates around 5.5 minutes into the recording and returns to the earlier rate near the 7-minute mark, there is no significant change in ictal durations. These plots were generated for all slices. Figure 3-5 and 3-6 present these plots for the representative data set initially plotted in Figure 3-1.

Finally, three slices from three different control animals exhibited an interesting “stair-step” trend. Figure 3-7 illustrates one such stability plot. Although not strictly linear, the stair-step pattern is consistent over the recording period and does not appreciably change. Next, plots of event duration vs. event number and event duration vs. event start time for these slices were inspected to see if there was a correlation between the stair-step pattern and event lengths. These plots are shown in Figure 3-8 and Figure 3-9, respectively. No apparent relationship between ictal event duration and the pattern is seen and neither wash-in/wash-out nor tissue necrosis appears to affect ictal activity, indicating that the activity remains stable for these slices as well.

Low Dose Slice Stability

Initial stability analysis for low dose slices began with examining ictal event number vs. ictal event start time. This analysis demonstrates a very pronounced stair-step trend in five of the seven slices from four of the five animals. Further, the remaining animal and two low dose slices demonstrate a less pronounced stair-step pattern

instead of the simple linear trend present in the majority of control slices. Figure 3-10 shows one example of the more pronounced stair-step stability plots. Again, although not simply linear, the stair-step pattern is consistent and does not appreciably change, even over an extended recording time exceeding 40 minutes.

Next, plots of ictal event duration vs. ictal event number were generated for low dose subjects. Figure 3-11 presents this plot for the data set used to construct Figure 3-10. Although the majority of events are short in duration (approximately 1 – 4 s), much longer event durations (approximately 25 – 40 s) appear to occur at a rate of every 20 – 30 events. No increase in event duration early in the recording or decrease in event duration late in the recording was observed, indicating that activity remained stable.

Finally, ictal event duration vs. ictal event start time plots were generated for low dose subjects. Figure 3-12 presents this plot for the data set used to construct Figures 3-10 and 3-11. Again, no event duration increase early in the recording or event duration decrease in the recording was observed. This further corroborates that the epileptiform activity generated is stable. Surprisingly, the longer duration events occur at relatively periodic rates, with an approximate period of 6 minutes in this example. Further, these long events are followed by clusters of short-duration events, which are in turn followed by periods of no activity.

High Dose Slice Stability

Lastly, stability for high dose irradiated subjects was assessed. Only one slice from this group exhibited a simple linear trend. The stair step pattern was observed in six of the eleven slices and four of the seven animals. The remaining four slices demonstrated a primary linear trend with a weak stair-step influence. Figure 3-13

presents all three stability plots for the high dose subject demonstrating a linear trend and Figure 3-14 presents these plots for a slice demonstrating the stair step.

Regardless of whether the pattern demonstrated was linear, stair step, or an amalgam of the two, the trend remained stable over the course of the recording period. This indicates that electrophysiological activity from high dose subjects, like control and low dose subjects, was stable over time.

Stability Conclusions

Overall, analysis of slice stability revealed acceptable stationarity of slice electrophysiology during the recording periods. Normally laminated control tissue demonstrated typically constant rates of activity. A few control slices displayed changes in ictal initiation rate but maintained linearity. Three of the eleven control slices from three of the seven control animals displayed a stair-step pattern in the occurrence of events. Examining the duration of the ictal events over time further validated stability and corroborated initial results suggesting that neither wash-in/wash-out nor tissue necrosis played a significant role in epileptiform activity over the course of the recording periods.

Five of seven slices from four of five low dose irradiated animals exhibited the stair-step pattern on their ictal event number vs. event starting time plot. Further analysis showed that longer duration events occurred at relatively regular intervals, both in terms of event number and time. Additionally, these long duration events preceded clusters of subsequent short duration events, which were in turn followed by periods of no activity. These trends remained unchanged over recording periods exceeding 40 minutes, thus indicating that the activity was stable.

Finally, high dose subjects displayed a simple linear trend in one slice and the stair-step pattern in six of eleven slices from four of seven animals. The remaining high dose subject displayed a primarily linear trend with a weak stair-step influence. Regardless, the trends remained constant over the course of the recording. This analysis suggests that neither wash-in/wash-out nor tissue necrosis had an appreciable effect on the electrophysiological activity of any slice over any of the recording periods.

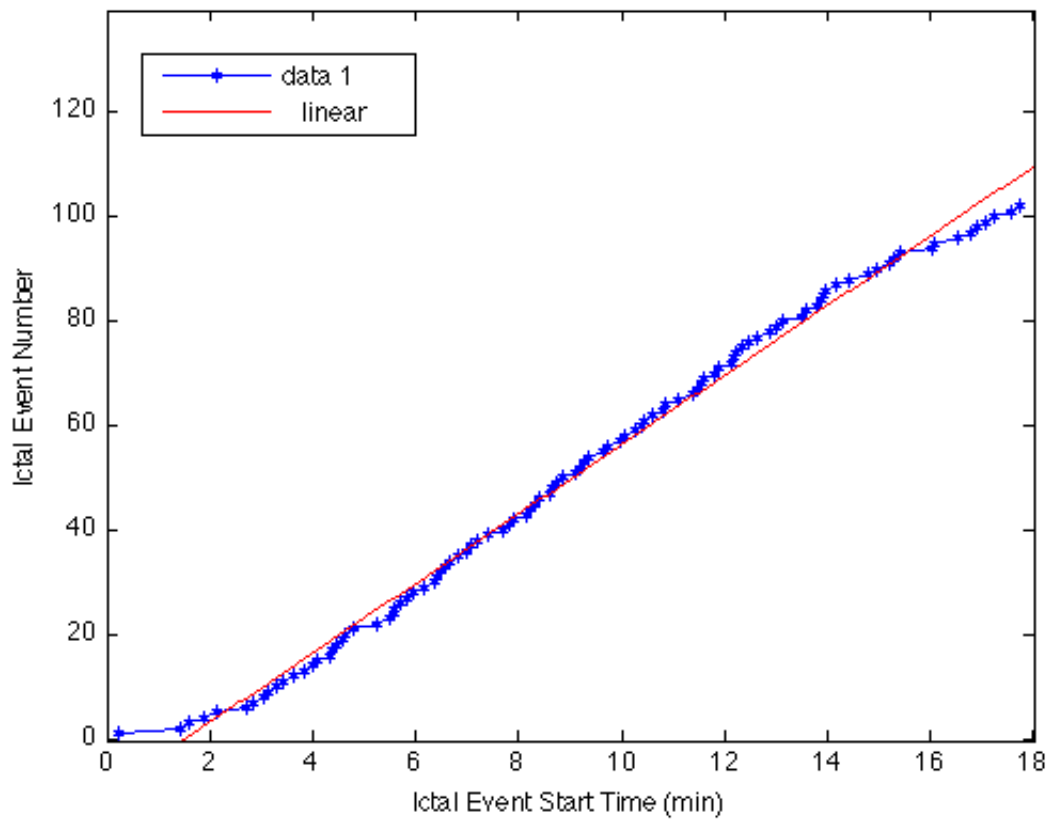
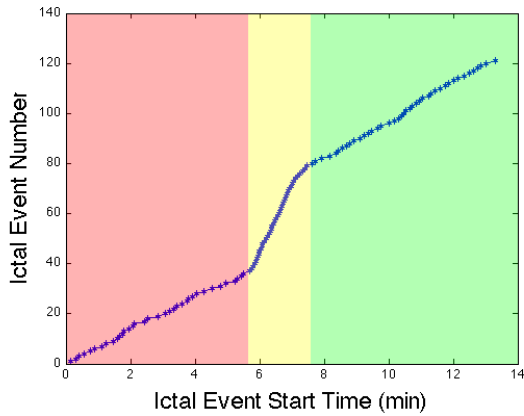
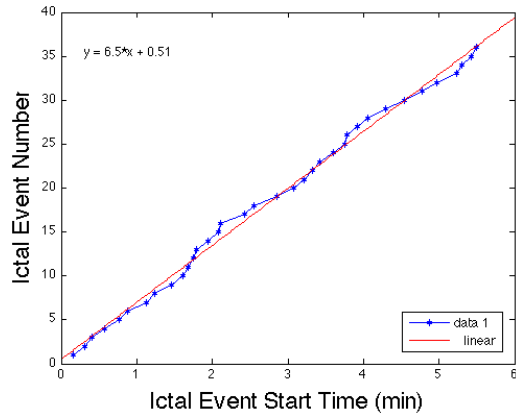


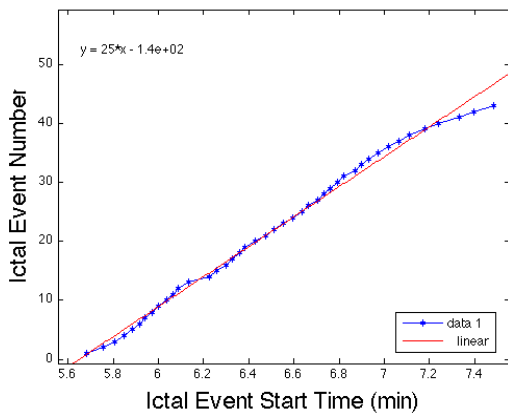
Figure 3-1. Ictal event number vs. ictal event start time for a normally laminated slice used to verify activity stability. The blue plot is the ictal event number vs. the start time. The red line is a linear fit of the data. As expected, the data signify that the wash-in / wash-out process did not have an appreciable effect on ictal activity.



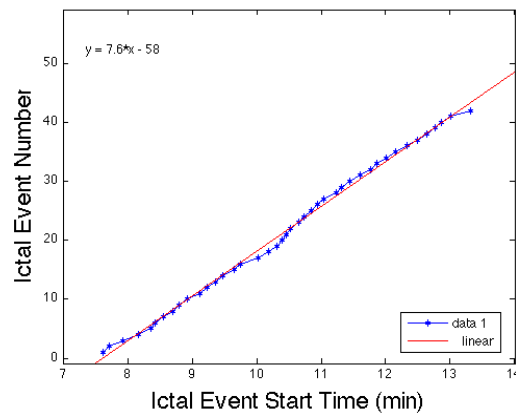
A



B



C



D

Figure 3-2. Control slice demonstrating three linear phases. A) Ictal event number vs. ictal event start time over the entire 13.3-minute recording. The slice activity has three distinct linear phases and are color coded red, yellow, and green for phase 1, phase 2, and phase 3, respectively. B) Enlarged plot of the first phase (red) from A, from the beginning until approximately 6 minutes into the recording. The slope of the linear fit for this phase is 6.5. C) Enlarged plot of the second phase (yellow) from A, from approximately 6 to 8 minutes during the recording. The slope of the linear fit for this phase is 25. D) Enlarged plot from the third phase (green) of A. Here the activity returns to a state similar to the first phase with a slope of 7.6.

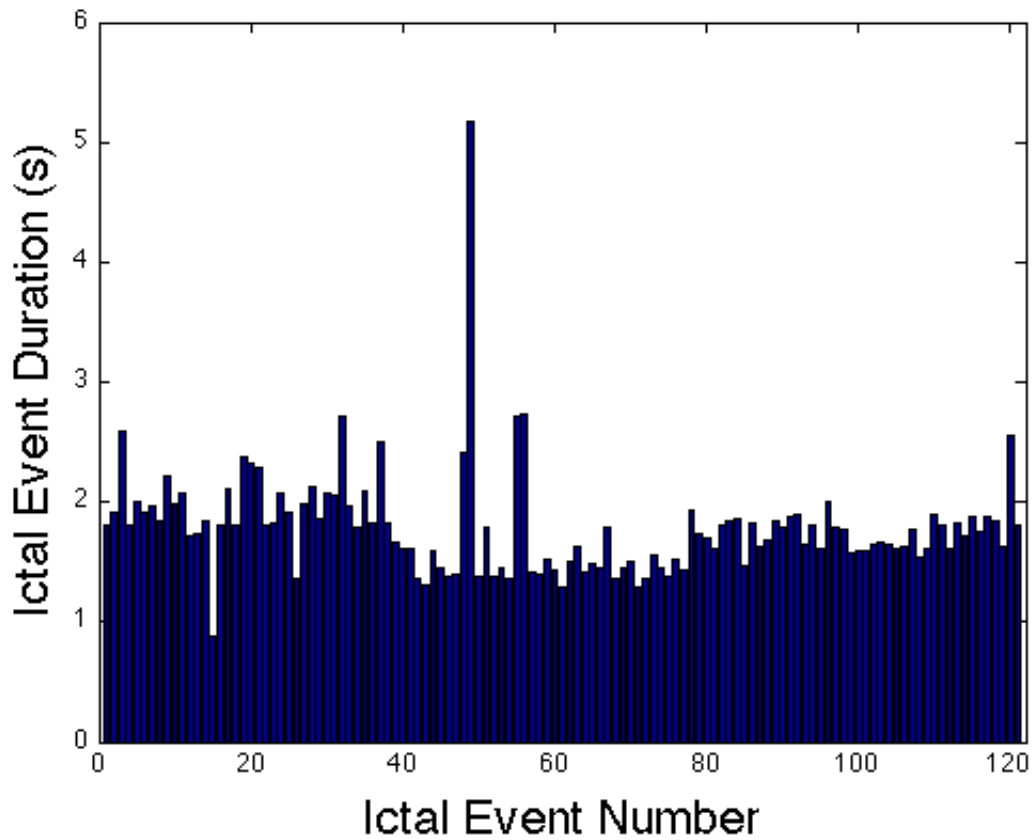


Figure 3-3. Ictal event duration vs. ictal event number. Data are from the same recording used to generate Figure 3-2, which appeared to have three distinct activity phases. No observable increase in ictal durations occur over the course of earlier events and no observable decreases occur over the course of later events, further suggesting ACSF wash-in / wash-out and tissue necrosis did not have an appreciable effect on epileptiform activity over the course of the recording period.

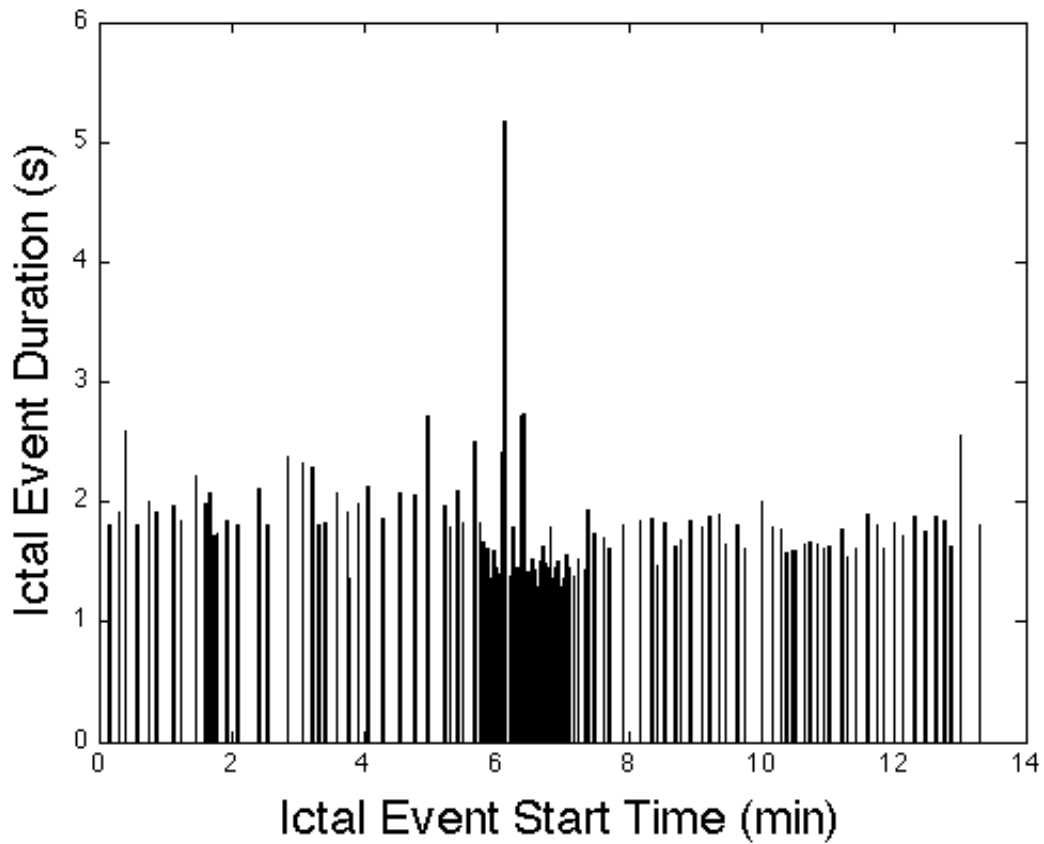


Figure 3-4. Ictal event duration vs. ictal event start time, verifying epileptiform activity was stable over the course of the recording period. Although an increased rate of event occurrence was observed during the second phase of the recording period (Figure 3-2 panel A (yellow), and Figure 3-2 panel C), no trend in event duration exists.

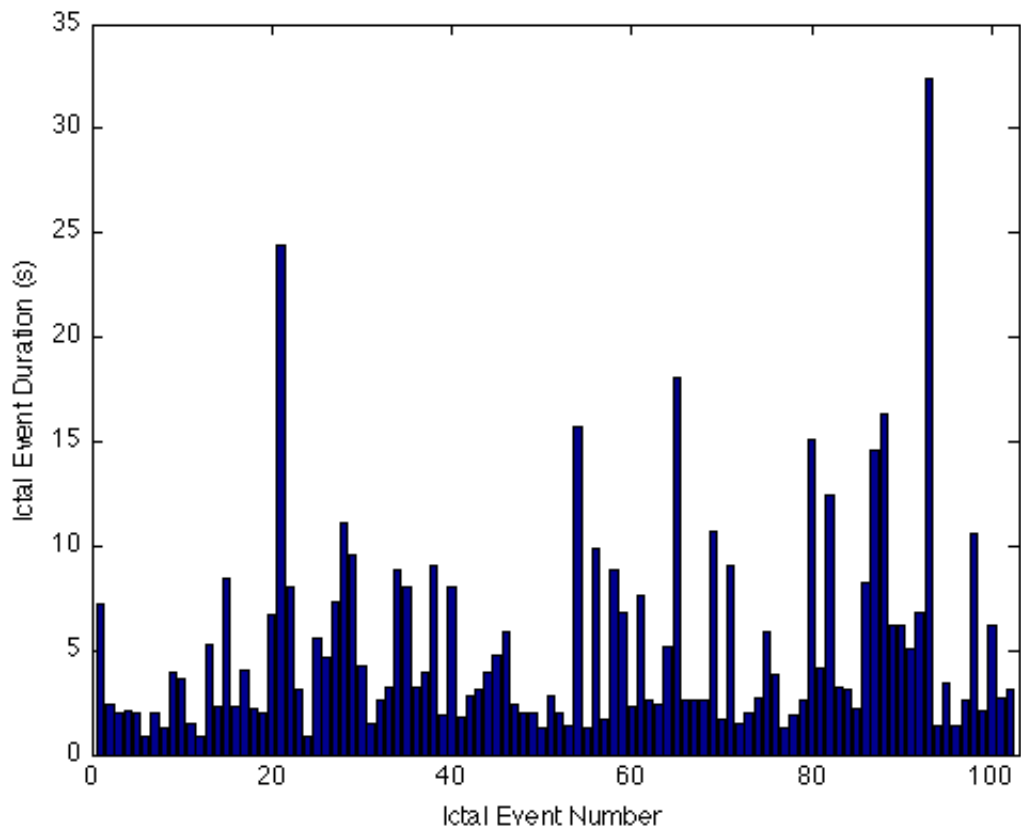


Figure 3-5. Ictal event duration vs. ictal event number for the same normally laminated slice data used in Figure 3-1. Again the data do not indicate a trend attributable to wash-in / wash-out.

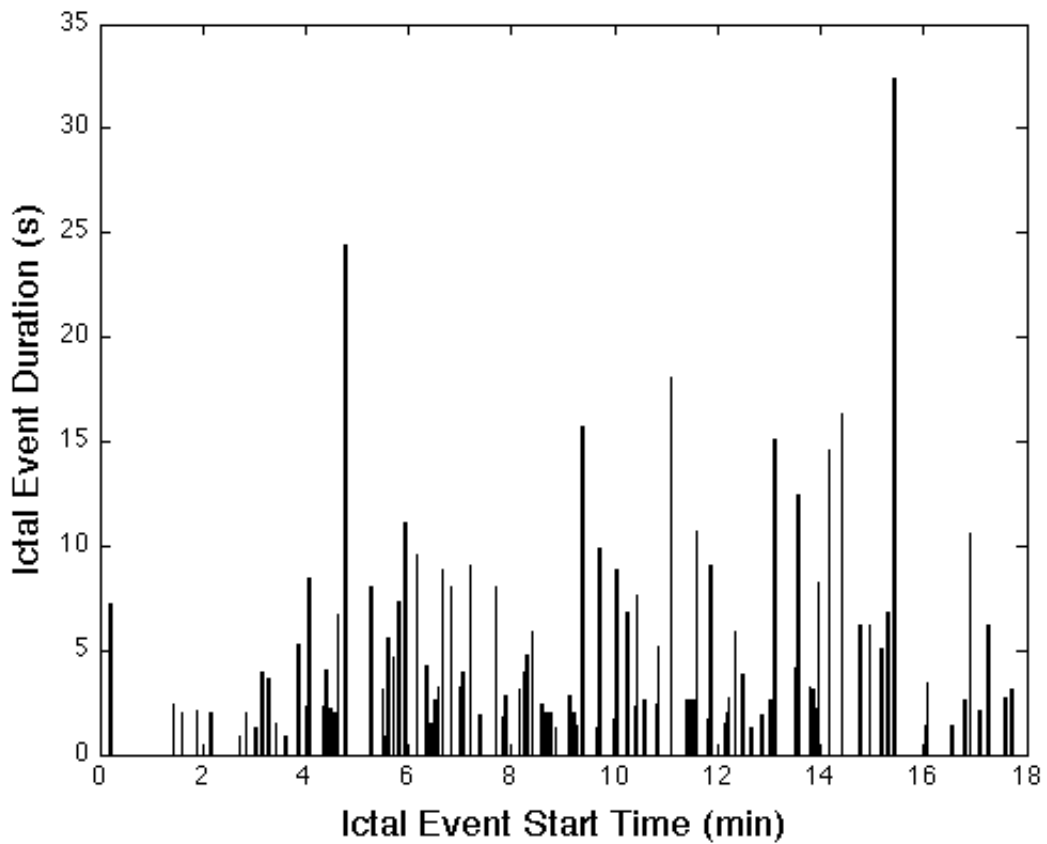


Figure 3-6. Ictal event duration vs. ictal event start time number for the same normally laminated slice data used in Figure 3-1 and Figure 3-5. This plot factors in the start time of the ictal event rather than just the event number. Again, the data suggest that wash-in / wash-out has no appreciable effect on activity.

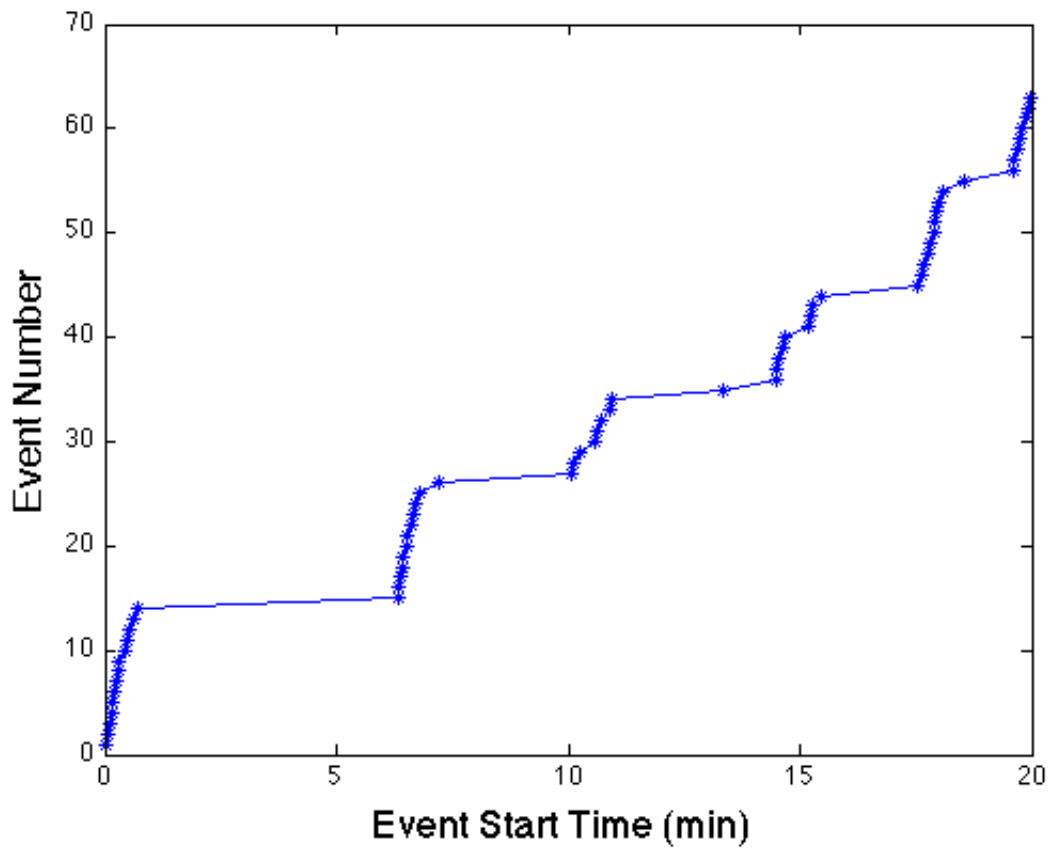


Figure 3-7. Plot of ictal event number vs. ictal event start time for a control slice subject illustrating stair-step pattern. Although not strictly a linear trend, the trend was maintained for a 20-minute period without significant deviation, suggesting stable activity during the recording period.

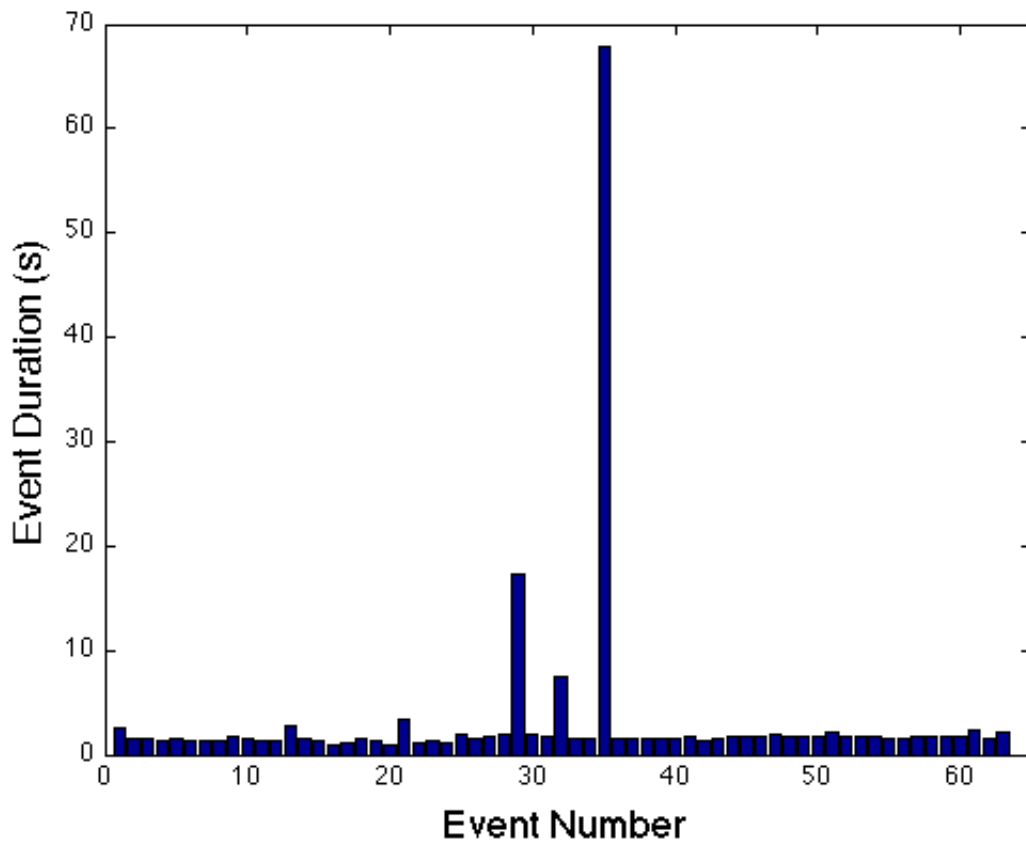


Figure 3-8. Ictal event durations vs. ictal event number for a control subject. Data used are the same used to generate Figure 3-7. No definite trend was seen for ictal durations, indicating that wash-in/wash-out and tissue necrosis were not factors leading to the stair-step pattern.

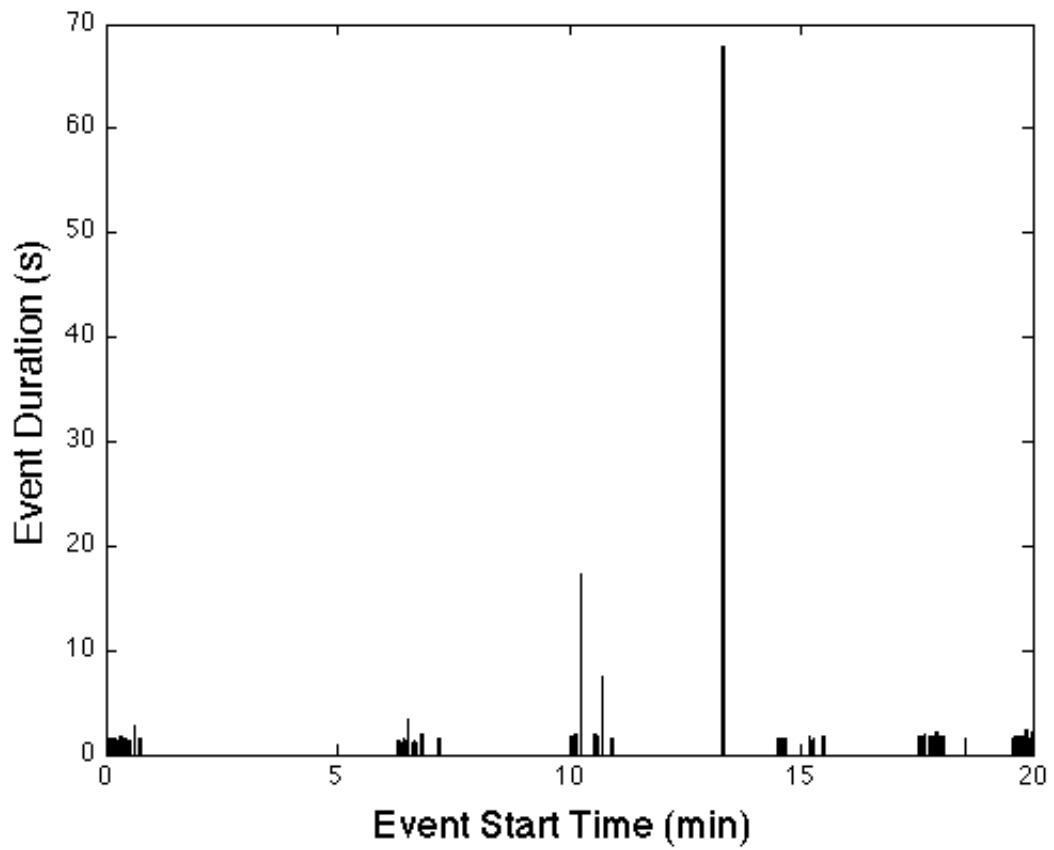


Figure 3-9. Ictal event duration vs. ictal event start time for a control subject. Data are from the same subject used to generate Figure 3-7 and Figure 3-8. This clearly makes the periodic event clustering more apparent.

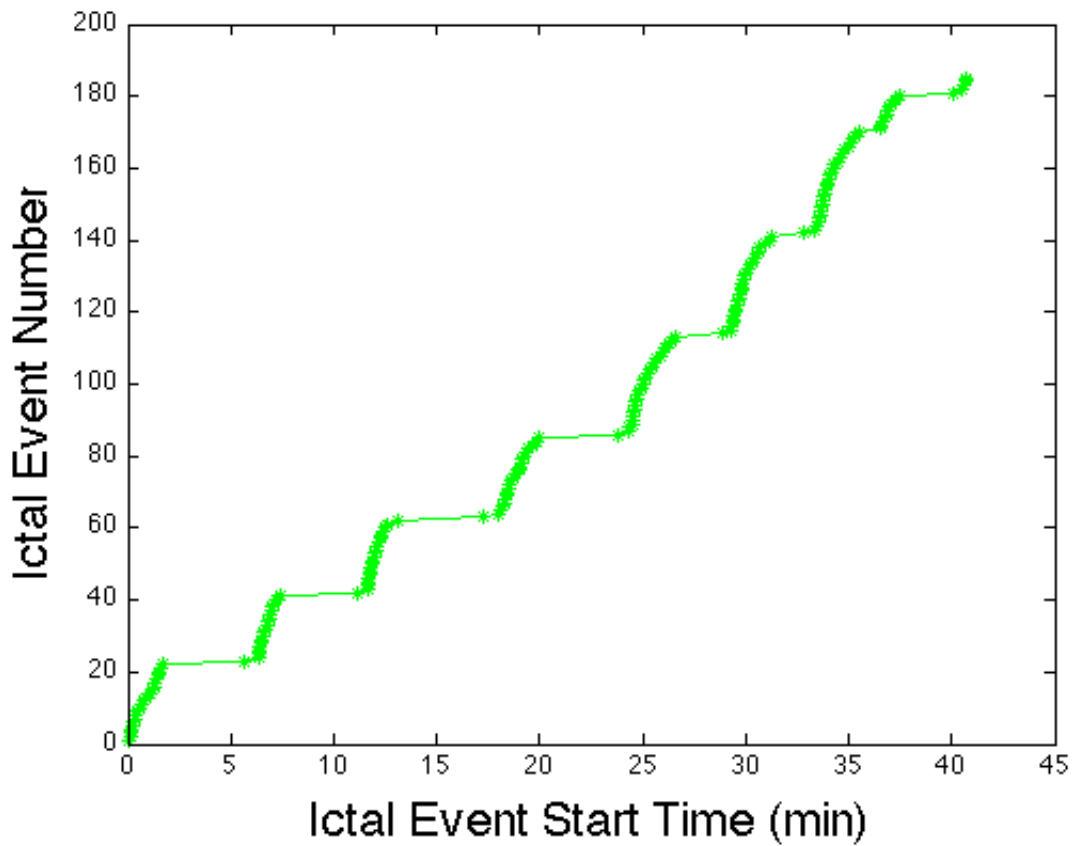


Figure 3-10. Plot of ictal event number vs. ictal event start time for a low dose irradiated subject illustrating characteristic pronounced stair-step pattern. Although not simply linear, the trend was maintained for over 40 minutes without significant deviation, suggesting stable activity during the recording period.

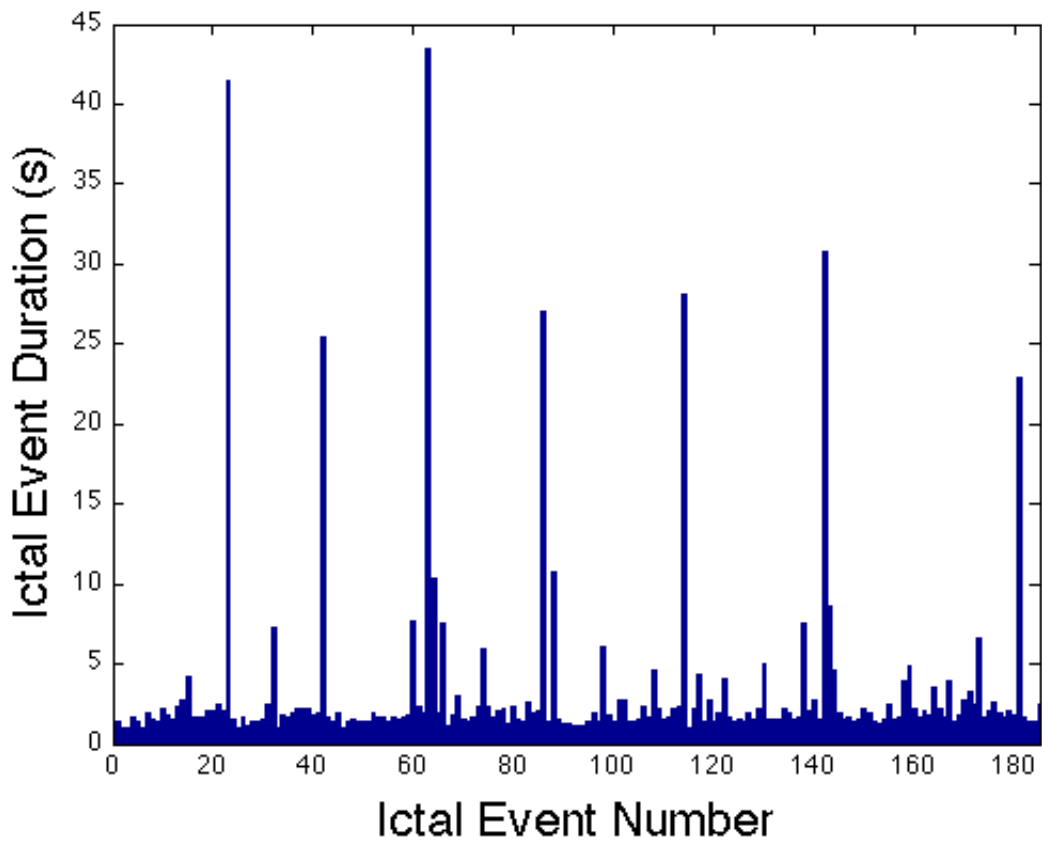


Figure 3-11. Ictal event durations vs. ictal event number for a low dose irradiated subject. Data used are the same used to generate Figure 3-10. As expected, an increasing trend early in the recording period and decreasing trend late in the recording period were absent, signifying stability over the recording period. Interestingly, long events appear to occur every 20 – 30 events.

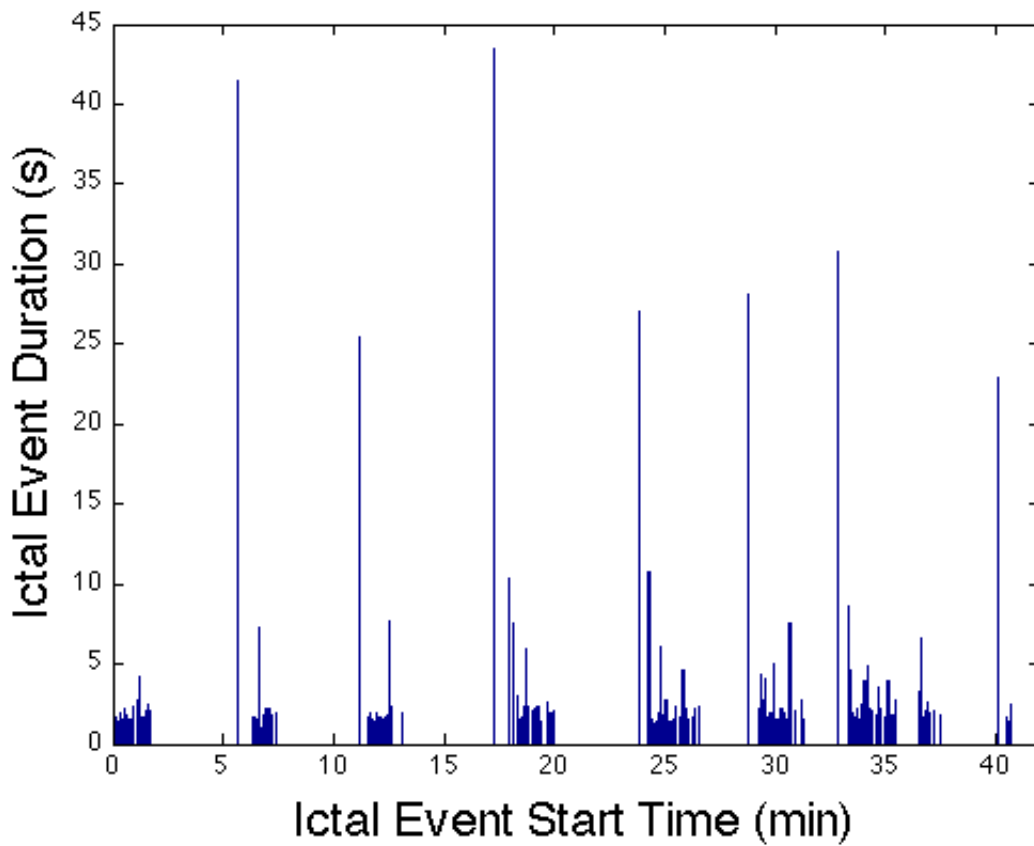
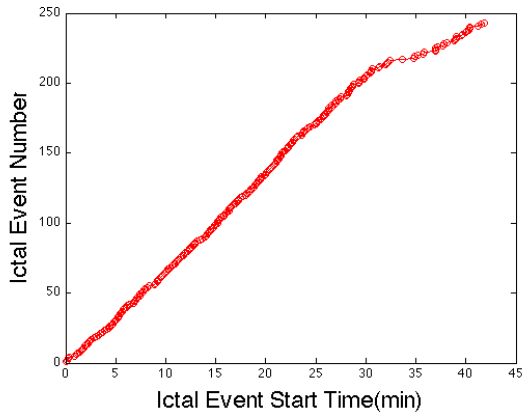
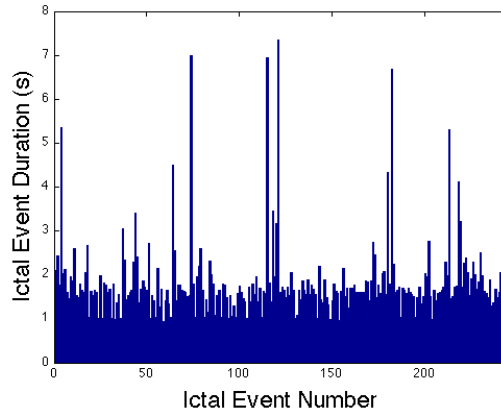


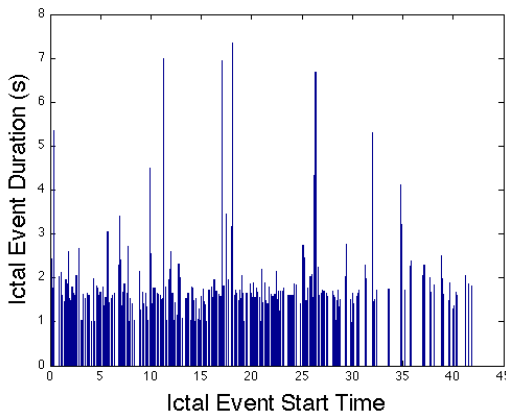
Figure 3-12. Ictal event duration vs. ictal event start time for a low dose irradiated subject. Data are from the same subject used to generate Figure 3-10 and Figure 3-11. This more clearly illustrates the periodic trend. Interestingly, the events with long durations occur at a relatively periodic rate and precede series of subsequent short duration events.



A

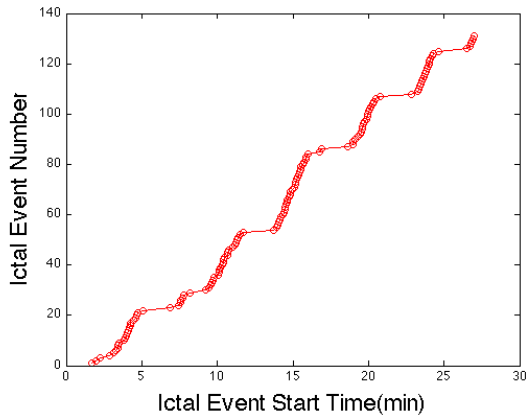


B

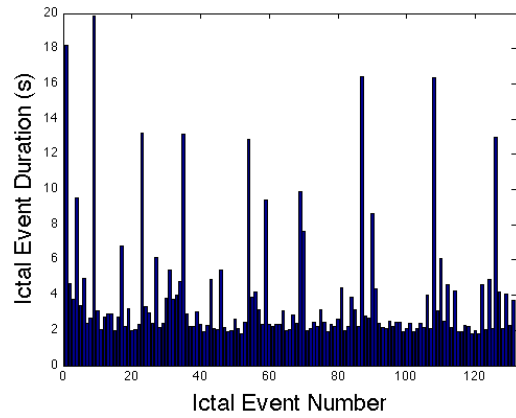


C

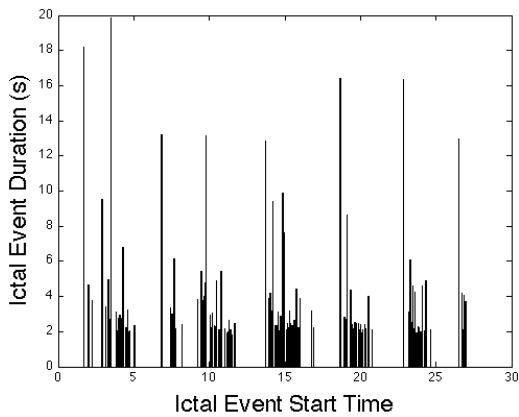
Figure 3-13. Characteristic stability plots for the high dose subject exhibiting a simple linear trend. A) The ictal event number vs. ictal event start time plot. This plot demonstrates a linear trend and was observed in most control slices. B) The ictal event duration vs. ictal event number plot for this subject, displays no trends in event duration over time, suggesting stability. C) The ictal event duration vs. ictal event start time plot also displays no trends over the recording period. Together, these data suggest that high dose slices, like control and low dose slices, display stable activity.



A



B



C

Figure 3-14. Characteristic stability plots for high dose subject exhibiting the stair-step trend. A) The ictal event number vs. ictal event start time plot, demonstrating the stair-step pattern also seen in nearly all low dose slices and over half of high dose slices. B) The ictal event duration vs. ictal event number plot for this subject displays no trend in event duration over time, suggesting stability. C) The ictal event duration vs. ictal event start time plot also displays trend changes in event duration over the recording period. However, as seen with low dose slices, long duration events appear to precede clusters of short duration events, which are then followed by periods of inactivity. Together, these data suggest that high dose slices, like control and low dose slices, display stable activity.

CHAPTER 4 CLASSICAL AND SPATIAL RESULTS AND ANALYSIS

Results of Classical Analysis Techniques

In this section I present the results of the experiments and analyze the data using classical, non-spatial metrics. These metrics have previously been employed by researchers to quantify the differences in seizure-like activity in a number of experimental protocols, such as the comparing the efficacy of different AEDs or electrical stimulation protocols.

Ictal Events per Recording Time

The occurrence of ictal events were modeled as being generated by a Poisson process, a stochastic process that counts the average number of events occurring per a unit time interval, where the events are generated independently at a constant average rate. I assumed this Poisson process to be homogeneous, with each class having a fixed-but-unknown rate parameter. The maximum-likelihood estimator for this parameter is simply the mean number of events per minute for each class, and the standard error is the square root of the sample mean. Control subjects produced an average 3.2298 ± 1.7972 events per minute, low dose subjects produced an average 4.0957 ± 2.0238 events per minute, and high dose subjects produced an average 2.6091 ± 1.6153 events per minute.

These results partially confirm the hypothesis that dysplastic tissue would have a higher mean rate of ictal events per time and low dose subjects would present a greater increase in ictal rate than the high dose subjects. Although low dose subjects presented an elevated mean rate of ictal events compared to control subjects, high dose subjects produced a lower mean rate of ictal events. However, this decline in ictal

rate generation in high dose subjects is not completely surprising, as behaving high dose subjects have not been shown to display epilepsy *in vivo*.

Average Event Length

Because event lengths are always positive, a distribution over event lengths with probability mass on negative values is inappropriate. Thus, data were modeled using a log-normal distribution. First, the lowest and highest 2.5% of samples were discarded to remove outliers. Then the event duration mean and standard deviation were calculated for each group, as well as the 95% confidence interval for the event length, according to Equations 4-1, 4-2, and 4-3 respectively. These results are shown in Table 4-1.

$$E[X] = e^{\mu + \frac{1}{2}\sigma^2} \quad (4-1)$$

$$std.dev.[X] = e^{\mu + \frac{1}{2}\sigma^2} * \sqrt{e^{\sigma^2} - 1} \quad (4-2)$$

$$CI_{95\%}[X] = [e^{\mu - 1.96\sigma}, e^{\mu + 1.96\sigma}] \quad (4-3)$$

where μ and σ are the mean and standard deviation of the natural logarithm of the event durations, respectively. These calculations show that the low dose group had both a shorter mean event length and smaller standard deviation than either the control or high dose groups.

Distribution of Event Lengths

To further investigate differences in event durations between groups, the distributions of event lengths were compared. Again, the lowest and highest 2.5% of samples from each group were discarded. Then normalized histograms were generated and are shown in Figure 4-1. Visually, three observations are apparent. First, the minimum event lengths generated by high dose subjects was longer than the minimum lengths generated by either the low dose or control subjects. Second, over

12% of the low dose events were of minimum length. Finally, the high dose and control groups contain a larger portion of longer events than the low dose group.

Next, the event lengths were fit to a log-normal distribution; the resulting fits are shown in Figure 4-2, along with a rug plot for reference. Although the most likely event duration was similar for all three groups, the fitted probability density functions show that events from low dose subjects are much more likely to be shorter in duration than either control or high dose events. Further, events from high dose appear to likely be longer in duration than control events.

Finally, two simple two-sample t-tests were performed. The first was done to investigate whether the measured event durations have significantly different means across groups. It was found that the mean ictal duration in low dose subjects was different than control and high dose subjects ($p_{\text{control, low dose}} = 2.746 \times 10^{-52}$, $p_{\text{low dose, high dose}} = 6.997 \times 10^{-55}$), but high dose was similar to control ($p_{\text{control, high dose}} = 0.1650$). The second two-sample t-test was to investigate whether the mean of the measured low dose events was less than the high dose or control events. The second two-sample t-test did not assume the classes had equal variances. The results indicate that there is significant evidence that mean ictal duration of the low dose group was lower than both the control and high dose group ($p \approx 0$, for both).

Together, these results reject the hypotheses that events generated by dysplastic tissue would have a longer mean duration and have a distribution of event lengths tending towards longer event lengths compared to controls. Surprisingly, low dose subjects, the only group to display epilepsy *in vivo*, have the lowest mean event duration, standard deviation, and 95% confidence interval, and have a distribution of

event lengths that tends towards shorter events compared to the other two groups. Additionally, control and high doses groups have a similar mean event duration, standard deviation, and distribution of event lengths.

Average Inter-Event-Interval

The inter-event-intervals were modeled using an exponential distribution, which is commonly used to model the time between event occurrences that are generated independently with a constant rate. First, the lowest and highest 2.5% of samples were discarded. Then, the event duration mean and standard deviation for each group were calculated, as well as a 95% confidence interval for the mean, according to Equations 4-4, 4-5, and 4-6, respectively. Results are shown in Table 4-2.

$$E[X] = \frac{1}{\lambda} \quad (4-4)$$

$$std.dev.[X] = \frac{1}{\lambda} \quad (4-5)$$

$$CI_{95\%}\left(\frac{1}{\lambda}\right) = \left[\frac{1}{\lambda} \frac{2n}{\chi^2_{2n;0.025}}, \frac{1}{\lambda} \frac{2n}{\chi^2_{2n;0.975}} \right] \quad (4-6)$$

where λ is the reciprocal of the sample mean and $\chi^2_{k;x}$ is the critical value of the chi-squared distribution with k degrees of freedom at the level specified by x. From these calculations, the low dose group had shorter mean inter-event intervals, a smaller standard deviation, and smaller confidence intervals than the control or high dose groups. The control and high dose groups had similar means, standard deviations, and confidence intervals.

Distribution of Inter-Event Intervals

To further investigate potential differences in inter-event intervals between groups, the distributions of intervals were compared. Again, the lowest and highest 2.5% of

samples from each group were discarded. Then normalized histograms were generated and are shown in Figure 4-3. As with the event duration histograms, three observations are apparent. First, the histograms appear to follow an exponential distribution for all groups. Second, a higher percentage of inter-event intervals from low dose subjects are much smaller than those from control or high dose subjects. Finally, with the exception of the shortest bin, the normalized histograms for inter-event intervals from high dose and control subjects appear to be similar.

Next, the inter-event durations were fitted to an exponential distribution; the resulting fits are shown in Figure 4-4, along with a rug plot for reference. The fitted probability density functions show that inter-event intervals from low dose subjects are much more likely to be shorter in duration than either control or high dose events. Further, inter-event intervals from high dose and control subjects appear to be very similar. The two-sample Kolmogorov-Smirnov confirmed that the inter-interval distribution of the low dose subjects is significantly different than the control and high dose subjects ($p_{\text{control, low dose}} = 3.552 \times 10^{-14}$, $p_{\text{low dose, high dose}} = 1.985 \times 10^{-11}$) and that the control and high dose subjects are not significantly different from one another at the 5% confidence level ($p_{\text{control, high dose}} = 0.0603$).

These results partially confirm the hypotheses that the mean inter-event intervals in dysplastic subjects tend to be shorter in irradiated subjects and that the inter-event interval distribution of irradiated subjects tends towards shorter lengths. Although the mean inter-event intervals from the low dose group is significantly lower than the control and high dose groups, the mean inter-event intervals of the control and high dose groups are not significantly different from one another.

Recovery Ratio

After the lowest and highest 2.5% of samples from the three groups were discarded, scatter plots of inter-event intervals vs. event durations were generated and are shown in Figure 4-5. Because the points for the groups frequently overlapped, multiple scatter plots were necessary for readability. Although some points from control and high dose subjects are distal from the central group, the vast majority of points for all groups cluster near the origin. No linear trend is observed in the groups, which was verified by calculating the correlation between event duration and inter-event interval for each group ($\rho_{\text{event duration, inter-event interval}} = 0.0725, 0.2367, \text{ and } 0.0088$ for control, low dose, and high dose groups, respectively).

Next, the recovery ratios for each group and their mean and standard deviations were calculated and are shown in Table 4-3. The sample means of the three groups are within 7.23% of each other, although the standard deviations of the groups vary much more. To gain insight into the distribution of recovery ratios, histograms of the recovery ratios were generated and are shown in Figure 4-6. Recovery ratios in all groups tend to be short (less than 5). However, control subjects tend to have a more uniform recovery ratio distribution than the experimental groups. Additionally, the decay in recovery ratios from low dose subjects is the most rapid, with over 59% being less than 3.

Finally, because the variables were not independent, no attempt was made to fit these data to a distribution. Instead, two nonparametric two-sample Kolmogorov-Smirnov tests were again performed. All groups are statistically different from one another at the 5% confidence level ($p_{\text{control, low dose}} = 3.8237 \times 10^{-5}$, $p_{\text{control, high dose}} =$

0.0018, $p_{\text{low dose, high dose}} = 0.0023$). Next, tests were performed to ascertain whether the distributions of irradiated group recovery ratios were less than the distribution from the control group. Only the distribution from the low dose group was found to be statistically likely to be smaller than the high dose group ($p = 0.0054$).

These results mostly reject the three hypotheses made about recovery ratios. First, no linear trend indicating an increased recovery ratio with increasing event lengths is observed. Second, both low and high dose groups have longer mean recovery ratios than the control group. Finally, the mean recovery ratio of the low dose group is greater than the high dose group.

Number of Field Potentials per Epileptic Event

The rates of positive, negative, and total field potentials among each group were assessed. First, the number of extrema occurring on each channel for every event was calculated and divided by the event duration. Next, since poor tissue-electrode contact could cause a large number of channels to register significantly fewer or no extrema, but not an elevation in the number of local field potentials, the extrema rate of the top six channels were averaged together for each event. This mean was used as the extrema rate for the event. The mean and standard deviation for the positive, negative, and total extrema rate were calculated and are presented in Tables 4-4, 4-5, and 4-6, respectively.

Next, the distributions of the positive extrema rate, negative extrema rate, and total extrema rate between each group were compared. After discarding the upper and lower 2.5% of samples, normalized histograms were generated and are shown in Figure 4-7, 4-8, and 4-9 for control, low dose, and high dose groups, respectively. The

extrema rates were then fitted to a normal distribution and the resulting fits are shown in Figure 4-10, along with a rug plot for reference.

Finally, a series of two-sample t-tests were performed to investigate whether the measured number of positive, negative, and total extrema rates during ictal events had significantly different means across groups. These results are presented in Table 4-7 and show that both the mean positive and negative extrema rates are significantly different among groups. Similarly, the mean total extrema rate of the control group is significantly different than the high dose group. However, there are not significant differences between the total extrema rates of the control and low dose groups or the high dose and low dose groups.

The hypothesis that dysplastic tissue would exhibit a higher extrema rate was partially confirmed. Low dose subjects displayed an elevated mean positive extrema rate compared to the control group, and the mean positive extrema rate in high dose subjects was lower than in the control group. The low dose group also displayed the lowest mean negative extrema rate, and the control group had the highest. Finally, the mean total extrema rate was found to be statistically different only between the control and high dose groups. Thus, the low dose group produced a disproportionately higher positive extrema rate and disproportionately lower negative extrema rate, compared to the other groups.

Summary of Classical Analysis

The results from classical analysis provide quantitative results that greatly expand upon the previous counter-intuitive anecdotal findings that high dose irradiated animals, which exhibit severe cortical dysplasia, are functionally more similar to control animals than low dose irradiated animals, which exhibit milder cortical dysplasia. Specifically,

low dose irradiated animals differ notably from control and high dose animals in that they have a higher mean number of ictal events per recording time, lower mean event length, smaller mean inter-event interval, greater number of positive extrema per epileptic event, lower number of negative extrema per ictal event. These findings suggest that a “Goldilocks Principle” applies to the amount of cortical dysplasia necessary to generate epilepsy. In other words, there may exist an ideal degree of dysplasia necessary to generate epilepsy, while dysplasia that is too minor or too severe fails to do so. Further, the combination of a higher mean number of ictal events and smaller inter-event interval in low dose subjects may be act to saturate the inhibitory networks, allowing seizure events to occur *in vivo*.

Results of Spatial Analysis Techniques

In this section I present further results of the experiments and analyze the data using spatial metrics. Previously, these spatial metrics were used exclusively on normally laminated slices to study the phases of ictal events and propagation of epileptiform activity.

Initiation Site

After calculating the initiation location for each event in all slices, two types of plots were generated for each recording to analyze the data. The first plot generated was a “heat map,” which shows the percentage of ictal events starting at each location on the MEA. If one or more dominant initiation foci were observed, the cell layer at which it existed was estimated using micrographs of the slice placed over the MEA. The second type of plot used was a graph of initiation channel number vs. event number. Dominant initiation foci are only observed in three control subjects (two from one animal and the third from a second animal), three low dose subjects (all from different animals), and no

high dose subjects. Of these, all of the control subjects and one of the low dose subjects demonstrate a strongly dominant focus; the other foci are weakly dominant. No other subjects displayed localized initiation foci. Figure 4-11 displays both plot types and the associated micrograph for one of the control subjects displaying dominant initiation foci, and Figure 4-12 displays both plot types and associated micrograph for a different control subject without dominant initiation foci.

In all control subjects, the dominant initiation foci are located in the deep (or infragranular) layers. Due to severe delamination in irradiated groups, estimation of the initiation focus location was based upon the layers that would be present in normally laminated subjects. Initiation foci are located in the approximated deep layers for one of the low dose subjects and in the upper, or supragranular, layers in two low dose subjects.

A final property observed in some slices displaying more than one dominant initiation focus was temporal dominance. Figure 4-11 part C illustrates this property. Here, two dominant initiation foci are present. Initially, electrode 40 serves as the dominant initiation focus. However, after approximately one-sixth of the events occur, electrode 42 becomes the dominant initiation focus and remains so throughout the experiment. Temporal dominance of initiation foci was observed in one control subject and one low dose subject. All other slices exhibiting dominant initiation foci merely had a higher number of initiations occurring at that location and did not display any temporal dominance.

Propagation

Two previously employed metrics for propagation were utilized: wave speed, a quantitative measure, and propagation pattern, a qualitative analysis of the flow of

epileptiform activity throughout the tissue. Because complex wave patterns could arise from phenomena, such as reflected waves, I chose to only include the first 500 ms of each event in the analysis. Next, the time of the first peak on each channel for all events was calculated. These data were then used to calculate the wave speeds and generate a visual representation of the wave propagation pattern.

Wave speed

Using the first peak times, a number of wave speed metrics were utilized. First, the horizontal and vertical wave speeds through the three groups were calculated. Wave speeds slower than 1 mm/s and faster than 275 mm/s were discarded from analysis. After discarding the upper and lower 2.5% of samples, the means for each group were calculated and two-sample Kolmogorov-Smirnov tests performed. Mean speeds are presented in Table 4-8 and results of the two-sample Kolmogorov-Smirnov tests between groups are presented in Table 4-9.

In all groups, and in accordance with literature, the mean speed of vertical wave propagation was greater than horizontal propagation within the same group. These results were also found to be statistically significant by the two-sample Kolmogorov-Smirnov test ($p = 2.0475 \times 10^{-83}$, 1.1113×10^{-28} , and 8.3396×10^{-24} for control, low dose, and high dose, respectively). Again, the high dose group appeared to be more functionally similar to controls than the low dose group, with high dose subjects having the lowest mean wave speeds in both horizontal and vertical directions. The low dose group presented the fastest mean wave speed times, and the mean horizontal speed was faster than the mean vertical wave speed for either the control or high dose groups.

Next, using micrographs for registration, the mean horizontal wave speed through the three categories of cell layers (supragranular, granular, and infragranular) was

calculated and two-sample Kolmogorov-Smirnov tests were performed. As with initiation sites, estimation of cell layer in delaminated subjects was based upon approximation to normally laminated slices. Mean horizontal wave speeds through each layer grouping are presented in Table 4-10 and results of the two-sample Kolmogorov-Smirnov tests are presented in Table 4-11 and Table 4-12.

Interestingly, and differing from the experiments performed by Contreras and Llinás in guinea pig cortex (Contreras and Llinás, 2001), the horizontal waves propagated fastest through the supragranular layers. Additionally, a key functional difference in the low dose group was that the propagation speed in the infragranular layer was slowest, while in the control and high dose groups, wave propagation through the granular layer was slowest. Results from two-sample Kolmogorov-Smirnov tests showed strong statistical significance between mean propagation speeds through each layer classification within each group and corresponding layers across groups.

Propagation pattern

In slices in which dominant initiation foci were present, colored gradients were used to qualitatively assess the propagation pattern originating from the foci. As previously mentioned, only three control and three low dose irradiated slices demonstrated dominant initiation foci. To create the colored gradients, the first peak times for all the ictal events originating from the dominant foci were averaged together, while events originating at other locations were discarded for this analysis.

Two main differences were observed between the control and low dose groups. First, wave propagation in control slices was typically uniform from the initiation site and the wave front eventually was observed at all locations. In low dose slices, the wave front did not move uniformly throughout the slice and some areas did not observe a

peak until far later in time, even though the sites were adjacent to one another. Second, wave propagation originating from a dominant focus in low dose slices appeared to move much more quickly through the slice than in control slices. Figure 4-13 illustrates these findings.

Termination Site

The procedure used to analyze termination locations was similar to the initiation location analysis. After calculating the termination location for each event in all slices, three types of plots were generated for each recording to analyze the data. The first two plots were the same type used in the initiation analysis: a “heat map,” which shows the percentage of ictal events terminating at each location on the MEA, and a graph of termination channel number vs. event number. If one or more dominant termination foci were observed, the cell layer at which it existed was estimated using micrographs of the slice placed over the MEA. The final plot type plotted both initiation and termination channel locations vs. event number. This was used to ascertain whether a dominant initiation focus was coupled to a dominant termination focus.

In general, a dominant termination focus was present in subjects also having a dominant initiation focus. Dominant termination foci were observed in two of the three control subjects that displayed dominant initiation foci and in two of the three low dose subjects with dominant initiation foci. However, one control subject that did not display a dominant initiation focus displayed two dominant termination foci. No dominant termination foci were observed in any high dose subject. Figure 4-14 displays termination analysis plots from the control subject used in Figure 4-11, and Figure 4-15 displays termination analysis plots for a control slice displaying no dominant termination foci.

Termination foci were found in all anatomical layers in control subjects, in the infragranular or granular layers in low dose subjects, and were not observed in high dose subjects. Again, estimation of cell layer in delaminated subjects was based upon approximation to normally laminated slices. One control subject had a single dominant termination focus located in the supragranular layers, one control subject had a single termination focus in the infragranular layers, and one control subject had one dominant termination focus in the granular layer and another in the infragranular layers. A dominant termination focus was seen in the infragranular layers of one low dose slice and the granular layer of another low dose slice.

Like initiation foci, termination foci also demonstrated temporal dominance. Only one control subject, shown in Figure 4-14 panel C, and one low dose subject had a termination focus displaying strong temporal dominance. Two control slices and one low dose slice displayed weak termination temporal dominance. The other low dose slice with a dominant termination focus merely had a higher percentage of events ending at that location and did not display temporal dominance.

Finally, coupling of a termination focus to an initiation focus was examined. Figure 4-14 panel D illustrates this occurrence. Here the dominant initiation focus, located at column 8 row 2, is strongly coupled to the dominant termination focus, located at column 1 row 2. Strong coupling was observed in only one control subject and one low dose subject. Weak coupling was observed only in one control dose slice.

The hypothesis that normally laminated subjects would display highly focused initiation and termination sites while dysplastic slices would display more diffuse initiation and termination sites was partially rejected. Dominant initiation foci were

observed in a minority of control and low dose (mildly dysplastic) subjects, while no high dose (severely dysplastic) subjects displayed dominant initiation or termination locations. The majority of slices in all groups displayed diffuse initiation and termination sites throughout the tissue.

Summary of Spatial Metrics

The three phases of epileptiform activity: initiation, propagation, and termination (Pinto et al., 2005) in both normally laminated and dysplastic cortex were analyzed. As with conflicting reports in literature about the existence of dominant initiation foci, some control and low dose subjects displayed such a phenomena, while the majority of subjects and all high dose irradiated subjects displayed diffuse initiation sites. In agreement with literature, wave propagation speeds were found to be faster traveling vertically across cell layers than horizontally through them. Wave velocities and propagation pattern in dysplastic cortex was provided and compared to normally laminated tissue, further showing functional similarities between high dose irradiated and control slices. Finally, dominant termination foci were observed in a small minority of control and low dose subjects, but not in high dose subjects.

Table 4-1. Ictal duration mean, standard deviation, and 95% confidence interval

Group	Mean (s)	Standard deviation (s)	95% Confidence interval (s)
Control	2.5623	1.1783	0.9866 – 5.4930
Low dose	1.7541	0.6459	0.8183 – 3.3111
High dose	2.7853	1.5925	0.8526 – 6.8573

Table 4-2. Inter-event interval mean, standard deviation, and 95% confidence interval

Group	Mean (s)	Standard deviation (s)	95% Confidence interval (s)
Control	12.1508	12.1508	11.2180 – 13.2055
Low dose	7.8289	7.8289	7.2921 – 8.4277
High dose	11.7032	11.7032	10.8879 – 12.6141

Table 4-3. Recovery ratio mean and standard deviation

Group	Mean	Standard deviation
Control	4.6889	5.8627
Low dose	5.0280	9.1528
High dose	4.8501	7.5043

Table 4-4. Positive extrema rate mean and standard deviation

Group	Mean (positive extrema / s)	Standard deviation (positive extrema / s)	95% Confidence interval (positive extrema / s)
Control	4.8246	1.5838	4.6967 – 4.9296
Low dose	5.4449	1.7579	5.3008 – 5.5199
High dose	4.5027	4.5028	4.3742 – 4.5884

Table 4-5. Negative extrema rate mean and standard deviation

Group	Mean (negative extrema / s)	Standard deviation (negative extrema / s)	95% Confidence interval (negative extrema / s)
Control	4.6345	1.5287	4.5024 – 4.7218
Low dose	3.9797	1.1564	3.8969 – 4.0373
High dose	4.5028	2.2451	4.2656 – 4.5437

Table 4-6. Total extrema rate mean and standard deviation

Group	Mean (extrema / s)	Standard deviation (extrema / s)	95% Confidence interval (total extrema / s)
Control	8.8641	2.7362	8.6364 – 9.0389
Low dose	8.6512	2.2476	8.4994 – 8.7769
High dose	8.4680	3.1588	8.2192 – 8.6286

Table 4-7. Results of two-sample t-tests on measured extrema rate means

	Positive extrema rate	Negative extrema rate	Total extrema rate
Control vs. Low dose	5.3335×10^{-13}	1.7433×10^{-18}	0.0993
Control vs. High dose	4.1827×10^{-5}	0.0262	0.0052
Low dose vs. High dose	4.7256×10^{-32}	3.2117×10^{-8}	0.0876

Table 4-8. Mean horizontal and vertical wave speeds through tissue

Group	Mean horizontal speed (mm / s)	Mean vertical speed (mm / s)
Control	33.7410	43.0345
Low dose	45.8539	52.9533
High dose	30.9584	34.2324

Table 4-9. Results of two-sample Kolmogorov-Smirnov tests on wave propagation speeds between groups

	Mean horizontal speed	Mean vertical speed
Control vs. Low dose	8.8093×10^{-116}	1.7101×10^{-66}
Control vs. High dose	3.3318×10^{-81}	9.0150×10^{-131}
Low Dose vs. High dose	8.0999×10^{-143}	2.4330×10^{-169}

Table 4-10. Mean horizontal propagation speed through cell layers

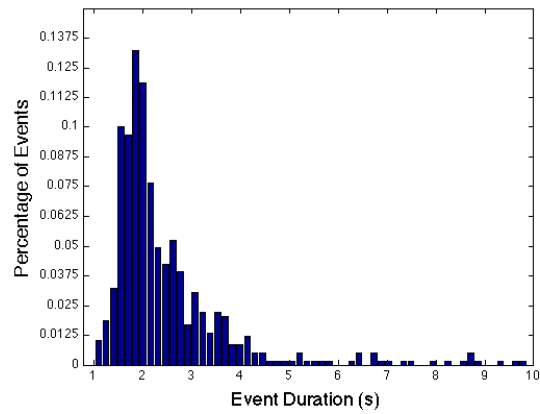
	Mean supragranular layer speed (mm / s)	Mean granular layer speed (mm / s)	Mean infragranular layer speed (mm / s)
Control	33.7783	29.9520	33.0372
Low Dose	48.2533	45.9235	40.0221
High Dose	30.8285	22.4406	23.3160

Table 4-11. Results of intra-group two-sample Kolmogorov-Smirnov tests on horizontal wave propagation speeds between cell layers

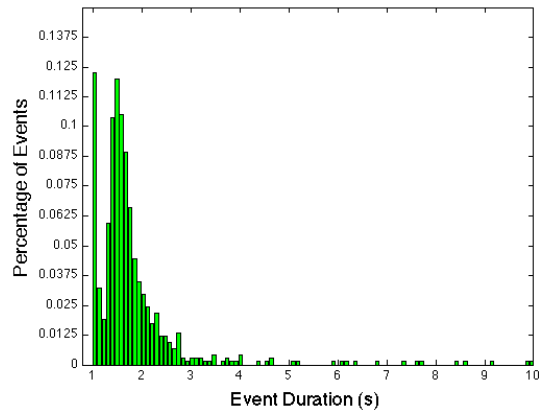
	p-value
Control supragranular vs. Control granular	9.5269×10^{-40}
Control supragranular vs. Control infragranular	4.2351×10^{-14}
Control granular vs. Control infragranular	1.3191×10^{-12}
Low dose supragranular vs. Low dose granular	2.7296×10^{-13}
Low dose supragranular vs. Low dose infragranular	8.2805×10^{-62}
Low dose granular vs. Low dose infragranular	1.3214×10^{-9}
High dose supragranular vs. High dose granular	5.9380×10^{-11}
High dose supragranular vs. High dose infragranular	1.4839×10^{-31}
High dose granular vs. High dose infragranular	1.3852×10^{-12}

Table 4-12. Results of inter-group two-sample Kolmogorov-Smirnov tests on horizontal wave propagation speeds between cell layers

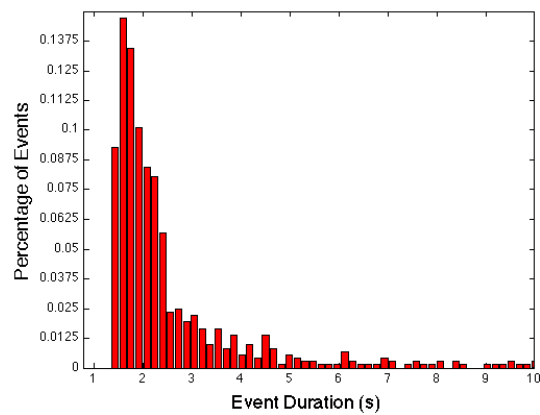
	Supragranular layer	Granular layer	Infragranular layer
Control vs. Low dose	2.3866×10^{-29}	4.4604×10^{-38}	2.3577×10^{-22}
Control vs. High dose	6.3804×10^{-53}	5.8648×10^{-35}	2.0605×10^{-167}
Low dose vs. High dose	2.2467×10^{-78}	2.0162×10^{-75}	2.0494×10^{-130}



A



B



C

Figure 4-1. Histograms of event duration normalized by number of events. For readability, events over 10 s in length have been omitted. A) Normalized histogram of event durations in control subjects. B) Normalized histogram of event durations in low dose subjects. C) Normalized histogram of event durations in high dose subjects.

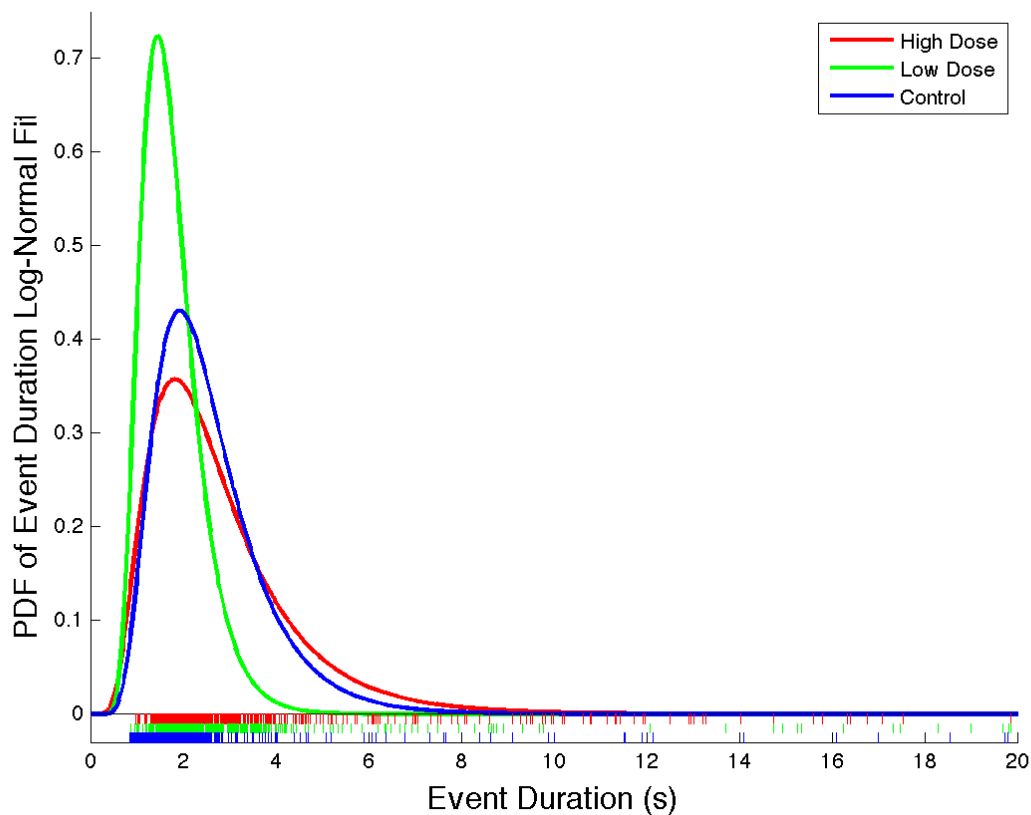
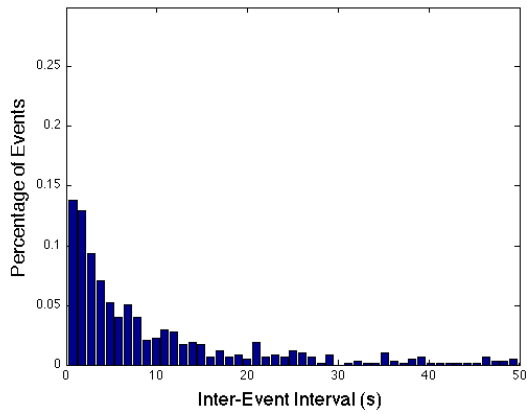
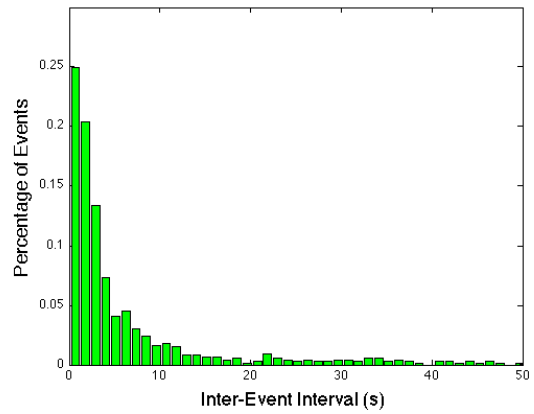


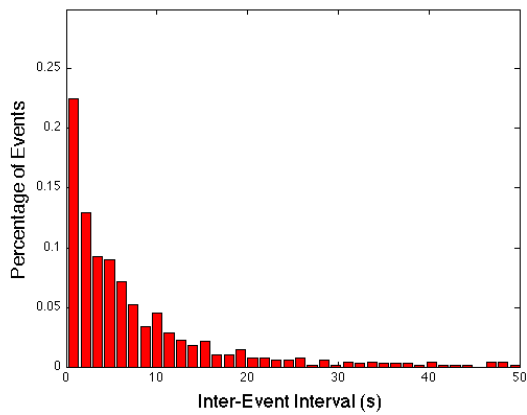
Figure 4-2. Log-normal fits of the event durations for each group. The ticks below the x-axis correspond to events occurring with the respective duration. For readability, this figure omits events greater than 20 s. The mean event duration from control and high dose subjects are significantly different from low dose subjects ($p \approx 0$ for both), while control subjects have a statistically insignificant higher probability of having shorter events than high dose subjects ($p = 0.1650$). Further, the mean duration of events from low dose subjects was statistically lower than the mean from either high or control groups ($p \approx 0$ for both).



A



B



C

Figure 4-3. Histograms of inter-event intervals normalized by number of event intervals. For readability, intervals over 50 s in length have been omitted. A) Normalized histogram of inter-event intervals in control subjects. B) Normalized histogram of inter-event intervals in low dose subjects. C) Normalized histogram of inter-event intervals in high dose subjects.

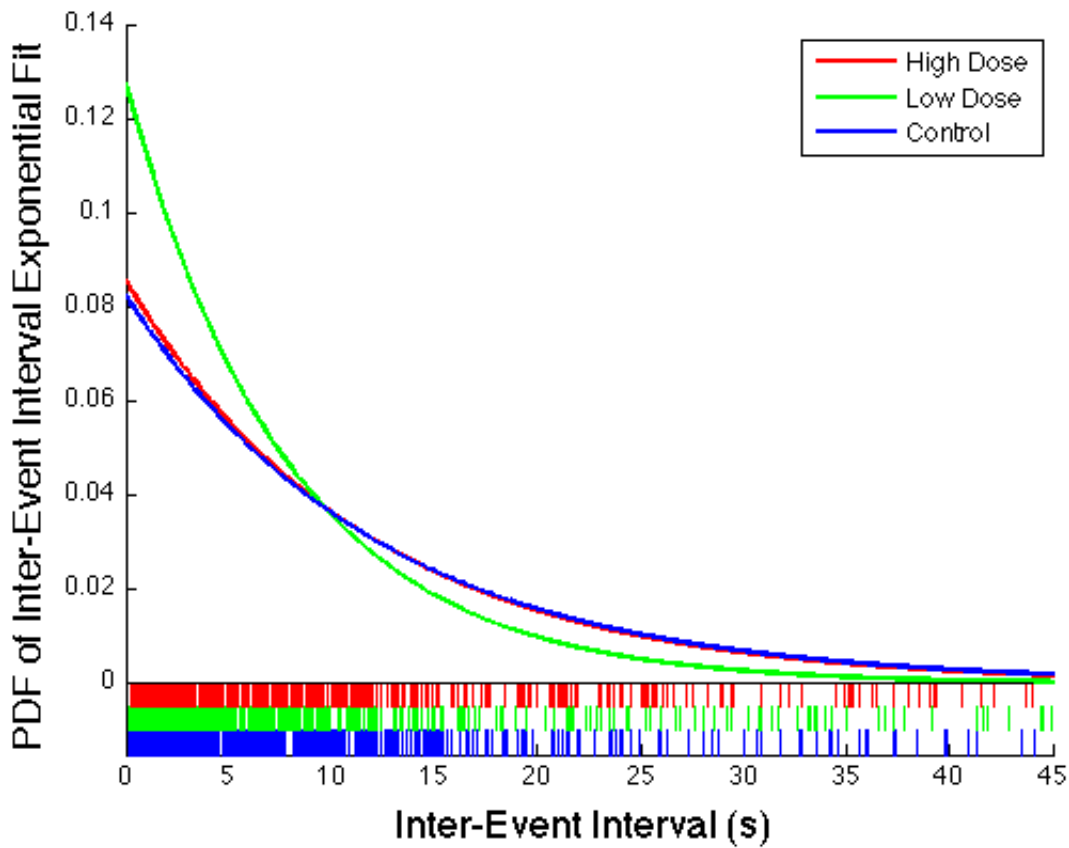


Figure 4-4. Exponential fit of the inter-event intervals for each group. The ticks below the x-axis correspond to event intervals occurring with the respective duration. For readability, this figure omits intervals greater than 45 s. The mean inter-event interval from low dose subjects was statistically different from the means of either control subjects or high dose subjects ($p \approx 0$ for both), while the mean inter-event interval from control subjects was not statistically different from high dose subjects ($p = 0.0603$).

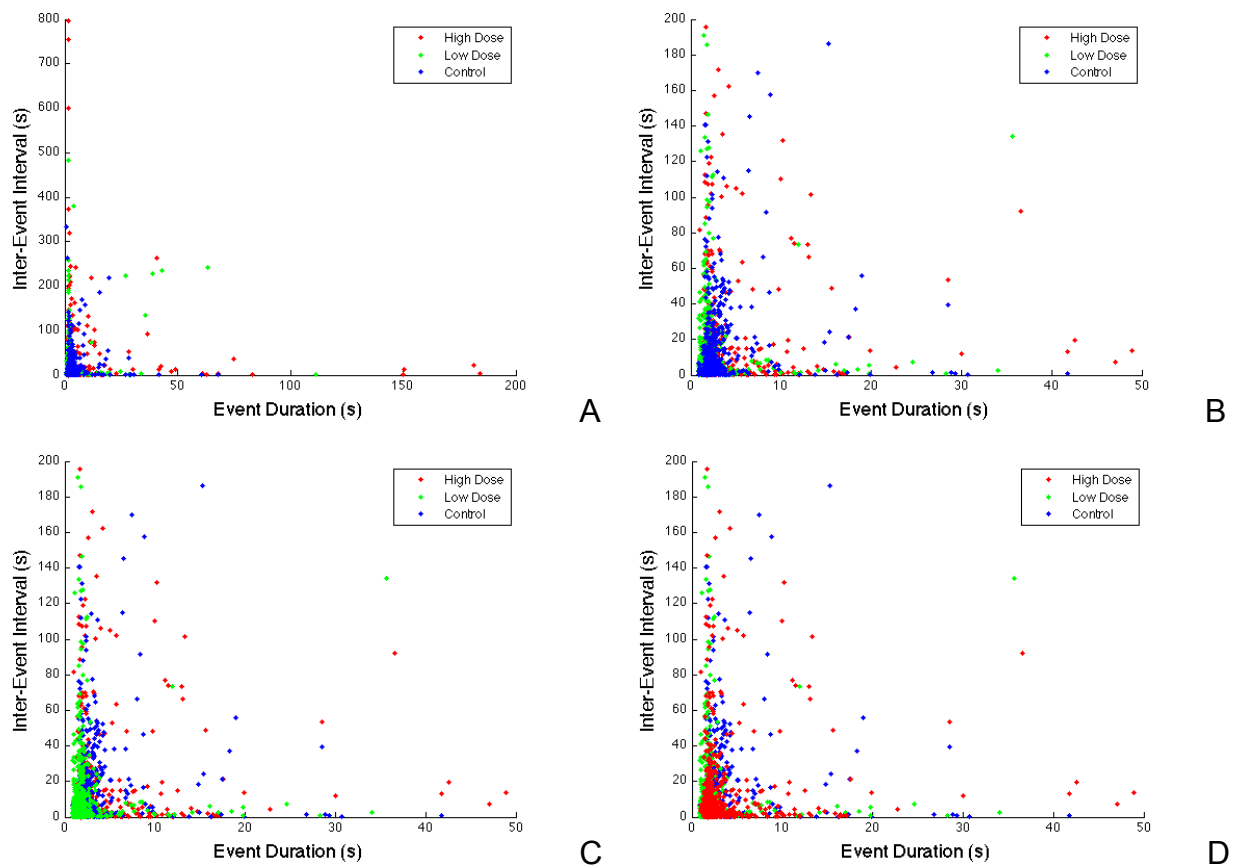
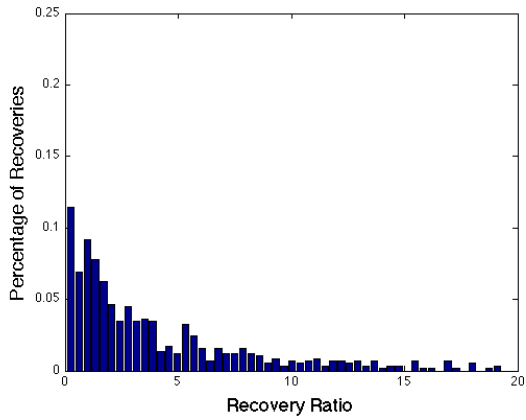
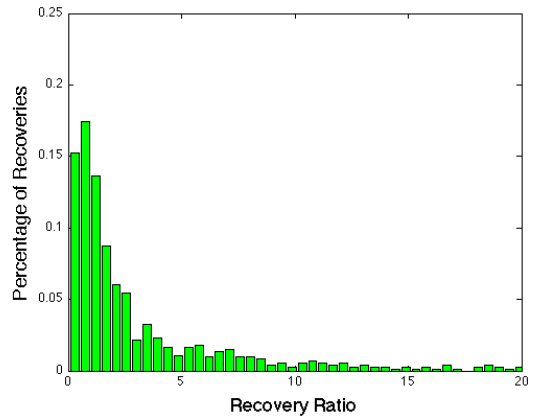


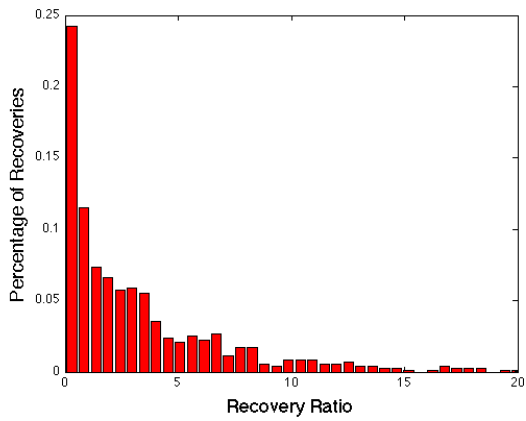
Figure 4-5. Recovery scatter plots. The recovery scatter plot is a plot of inter-event intervals vs. time. A) All events from all groups plotted, with the control group plotted last. B) Zoomed in view of lower left portion of A to show detail. C) Zoomed in region with low dose group plotted last. D) Zoomed in region with high dose plotted last.



A



B



C

Figure 4-6. Histograms of recovery ratio for subjects. Recovery ratios larger than 20 were omitted for visual readability. A) Histogram of recovery ratios from control subjects. B) Histogram of recovery ratios from low dose subjects. C) Histogram of recovery ratios from high dose subjects.

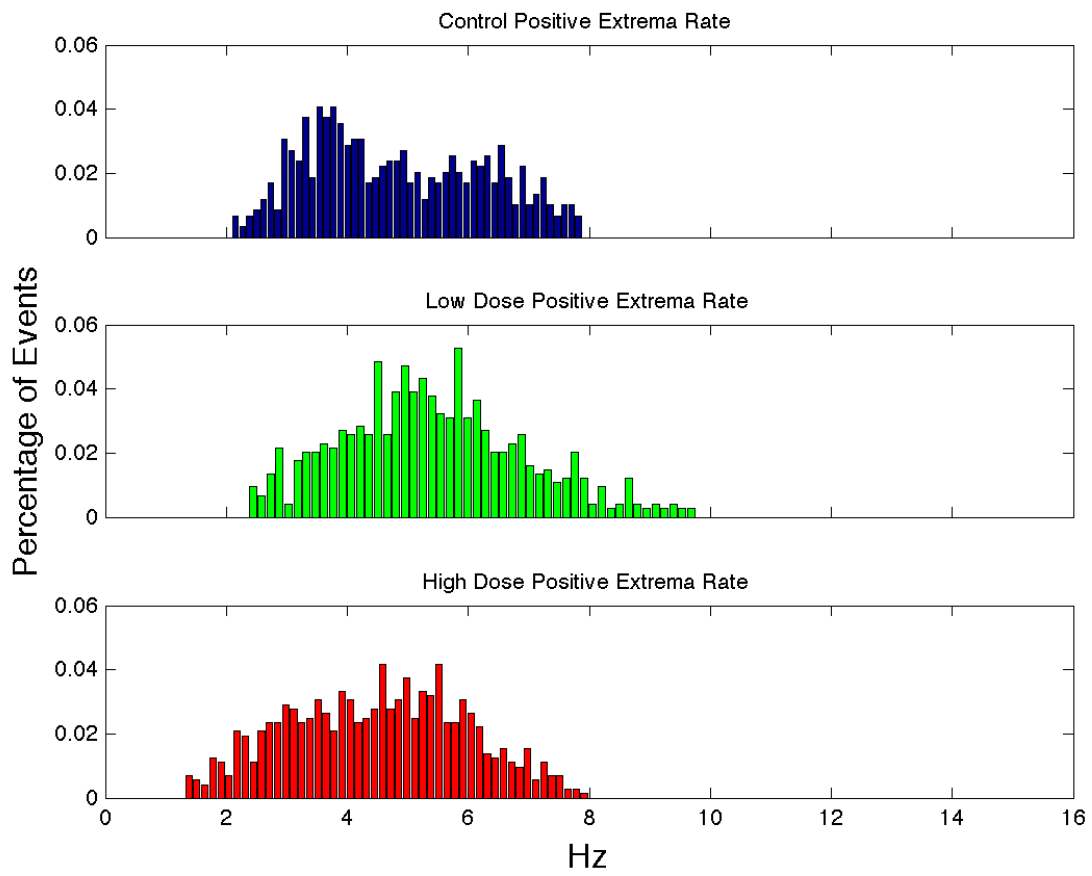


Figure 4-7. Histograms of positive extrema rates in control, low dose, and high dose groups.

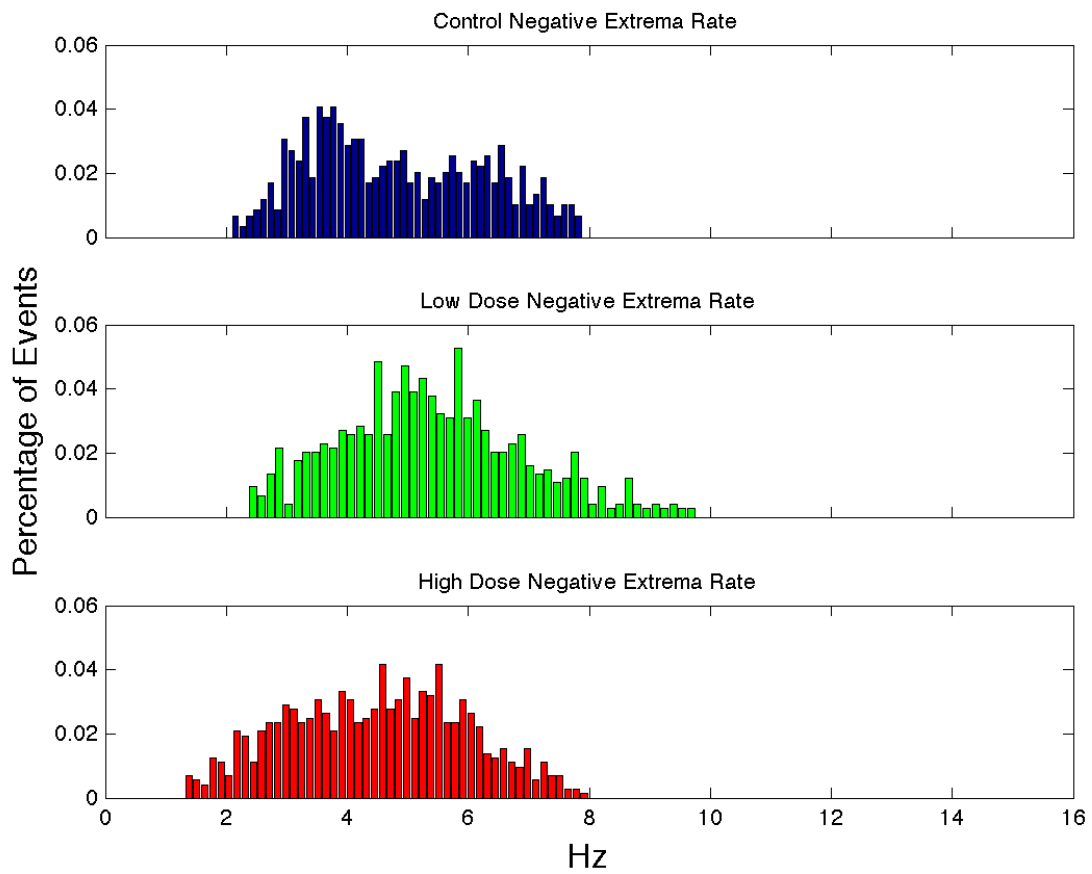


Figure 4-8. Histograms of negative extrema rates in control, low dose, and high dose groups.

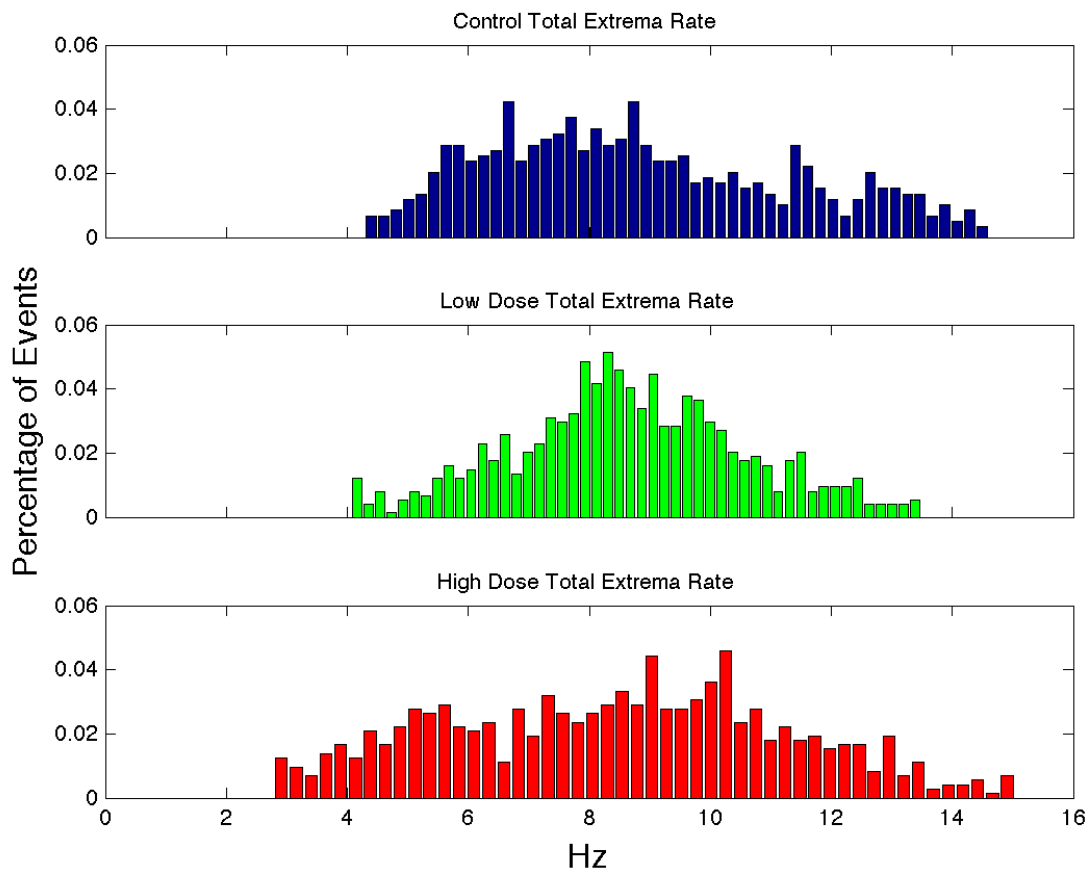
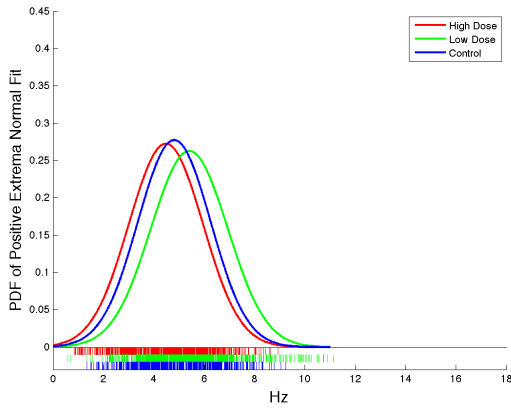
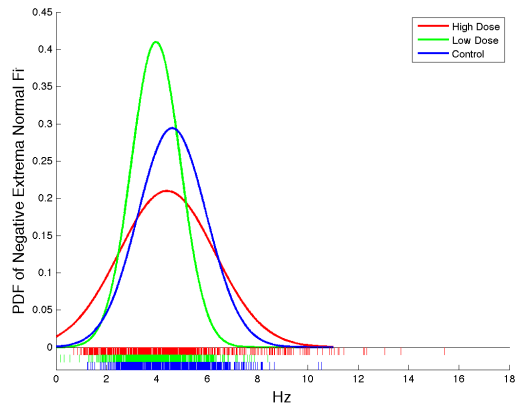


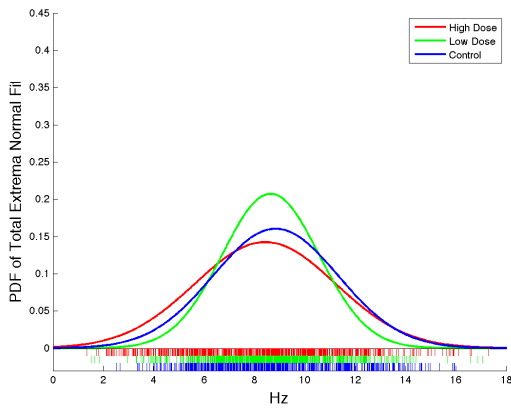
Figure 4-9. Histograms of all extrema rates in control, low dose, and high dose groups.



A



B



C

Figure 4-10. Normal fits of the positive, negative, and total extrema rates for each group. A) Normal fit of the positive extrema rate for each group. B) Normal fit of the negative extrema rate for each group. C) Normal fit for the total extrema rate for each group.

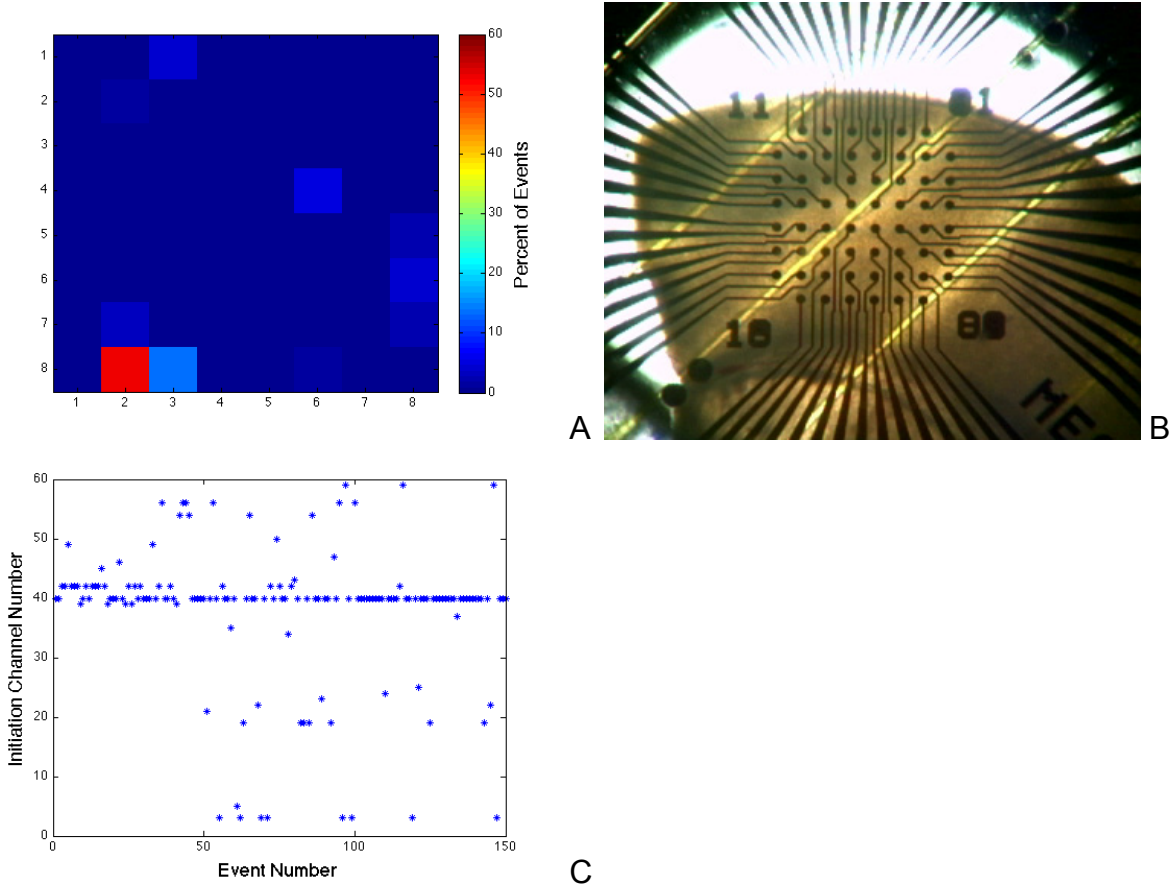


Figure 4-11. Analysis plots for a control subject displaying a strongly dominant initiation focus. A) Heat map of initiation events showing that the electrode located at row 8, column 2 was strongly dominant. B) Micrograph of the slice, using a Teflon harp to ensure good tissue-electrode contact. The dominant focus appeared to arise from the infragranular layer. C) Plot of initiation channel vs. event number illustrating that initially, a second focus was strongly dominant for the first sixth of the events before the primary focus became dominant.

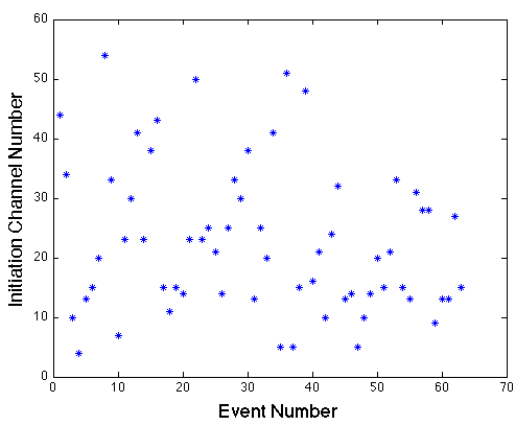
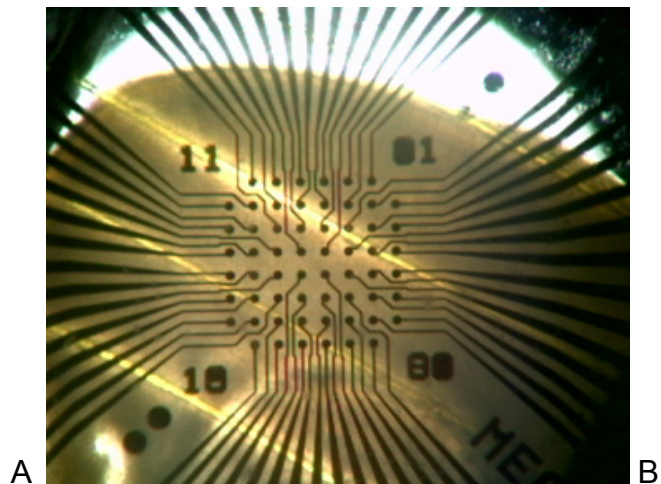
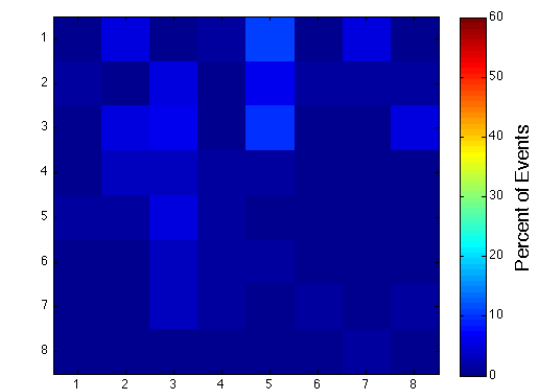


Figure 4-12. Analysis plots for a control subject without a dominant initiation focus. A) Heat map of initiation events showing diffuse initiation pattern. B) Micrograph of the slice, using a Teflon harp to ensure good tissue-electrode contact. C) Plot of initiation channel vs. event number illustrating absence any dominant initiation foci, including temporally local dominant initiation foci.

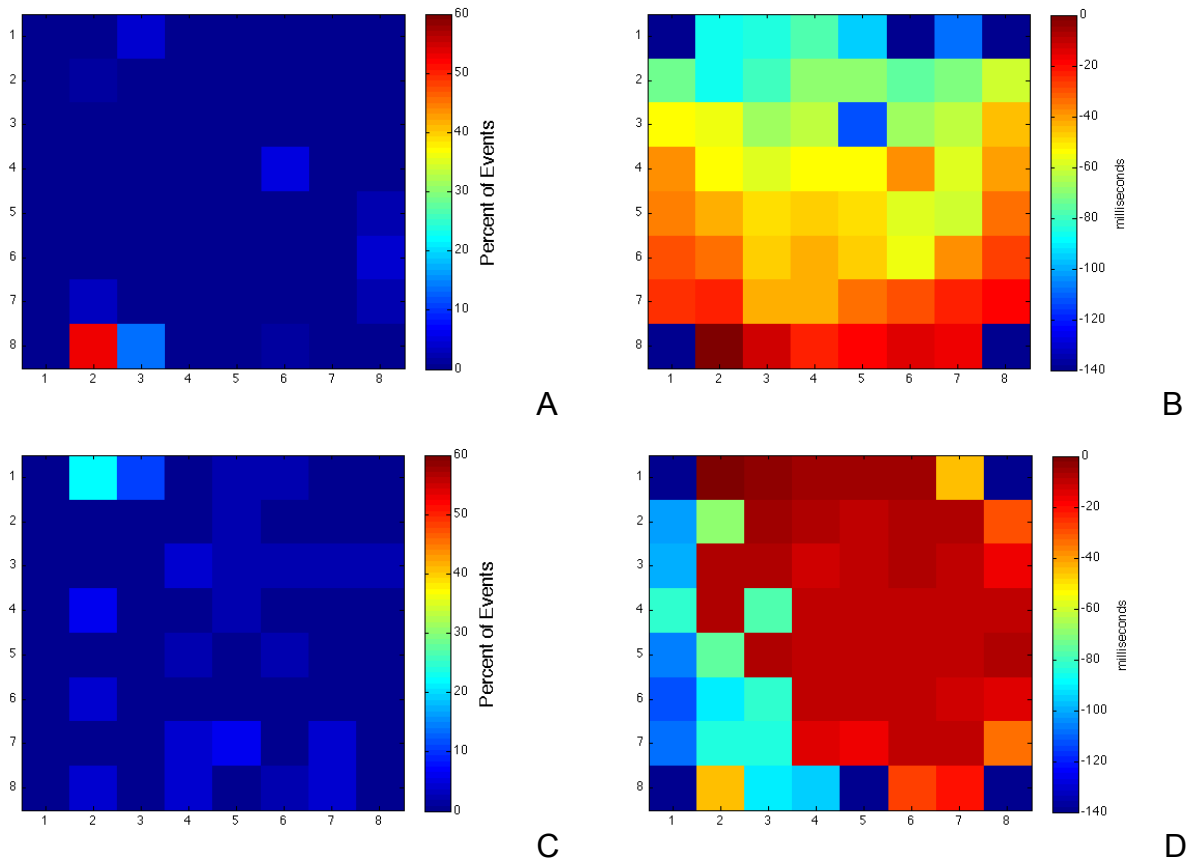


Figure 4-13. Wave propagation analysis plots. A) Control slice heat map showing the dominant initiation focus located at row 8, column 2. B) Colored gradient formed from averaging first peak times for events originating at row 8, column 2. Note that the wave propagates rather uniformly from the origination point and the wave front is observed at all locations. C) Low dose slice heat map showing the dominant initiation focus located at row 1, column 2. D) Colored gradient formed from averaging first peak times for events originating at row 1, column 2. Note that the wave does not propagate uniformly throughout the slide. Additionally, the wave appears to propagate much faster to the preferred areas as compared to the control slice.

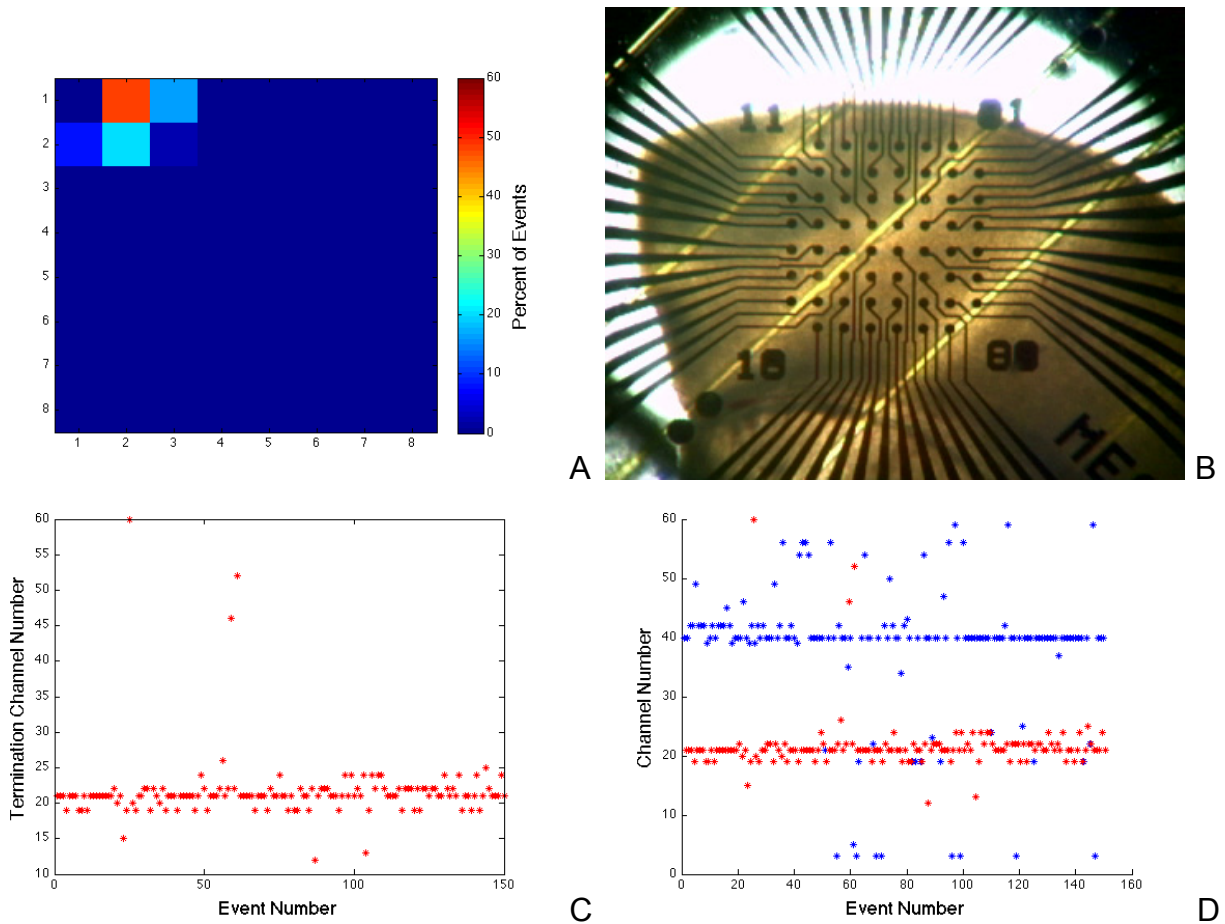


Figure 4-14. Analysis plots for a control subject displaying a dominant termination focus. A) Heat map of termination events showing that the electrode located at row 1, column 2 was dominant. B) Micrograph of the slice, using a Teflon harp to ensure good tissue-electrode contact. The dominant termination focus appears to arise from the supragranular layer. C) Plot of termination channel vs. event number illustrating that the termination focus was dominant throughout the recording. D) Plot of initiation (blue) and termination (red) locations as a function of event number. From this plot, the dominant termination focus appears to be strongly coupled to the initiation focus.

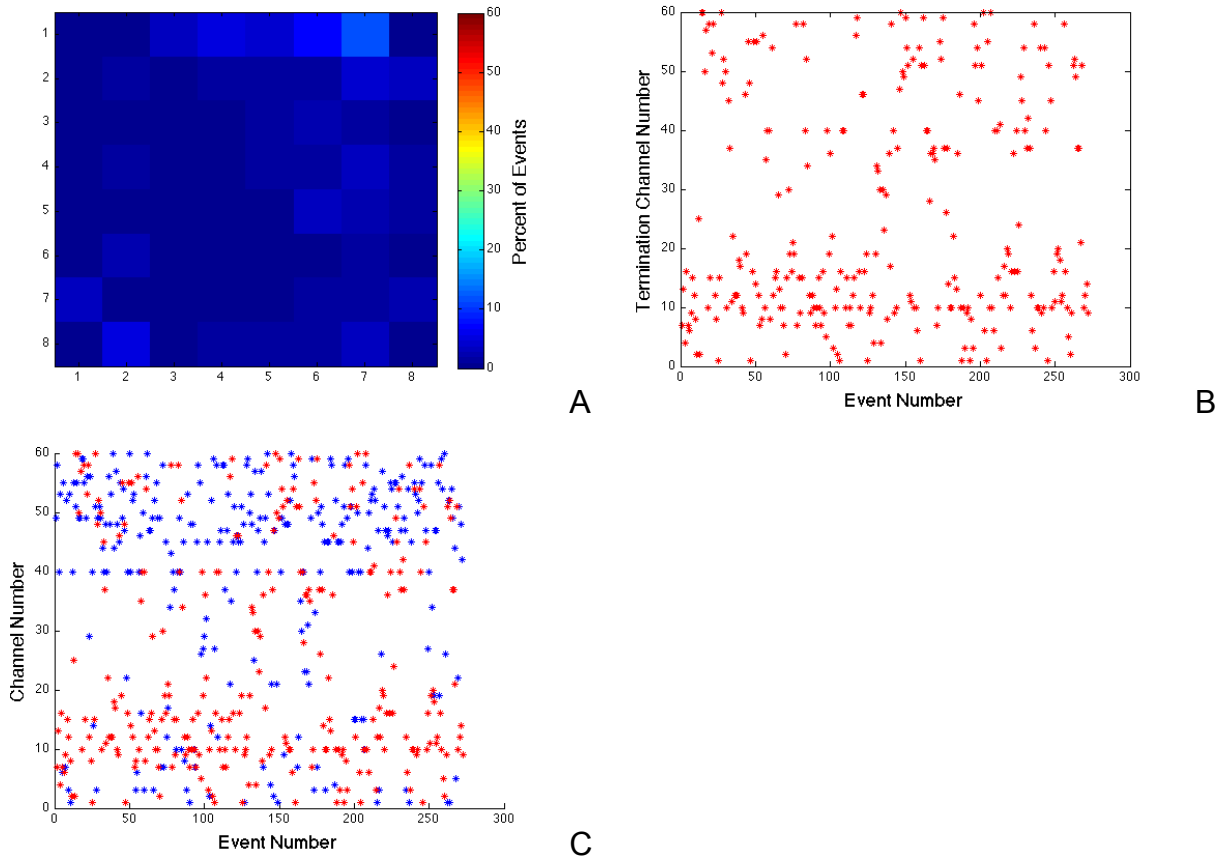


Figure 4-15. Analysis plots for a control subject displaying diffuse termination locations. A) Heat map of termination events showing that the absence of a dominant termination focus. B) Plot of termination channel vs. event number illustrating a lack of temporally dominant termination focus. C) Plot of initiation (blue) and termination (red) locations as a function of event number. From this plot, there appears to be no coupling between initiation and termination sites.

CHAPTER 5 GRANGER CAUSALITY RESULTS AND ANALYSIS

Results From Pairwise Granger Causality Analysis

In this section I present the results of pairwise Granger Causality analysis in an attempt to uncover previously unobserved localized driving regions within slice during ictal events. While these analysis techniques, originating in the economics field, have recently gained prominence in the neuroscience community, their application to acute slice data is novel. Both quantitative comparisons, such as differences in PWGC values and distributions between experimental groups and anatomical cell layers, and qualitative comparisons, such as the spatial locations of driving PWGC sites, are made.

Analysis Methods

Pairwise Granger causality was calculated using a custom program written in our laboratory using the C programming language. The recorded data, which were post-processed with custom automated tools I wrote and visually verified as discussed in Chapter 2, were used. In order to reduce computation time, data were first down-sampled from 25 kHz to 250 Hz. Pairwise Granger causality then was calculated using a moving window of 200 ms with a 50% overlap.

The output of pairwise Granger causality produces a single complex-valued spectral matrix based upon the total number of trials, or in this case ictal events. Three steps were taken to simplify analysis. First, the magnitudes of the complex values were taken to provide real number values. Second, spectral information was collapsed through summation to provide the total PWGC values across all frequencies. Finally, since events could have varying lengths, all events were at least one second in duration, and previous literature reports that the first part of an ictal event is the most

reliable and repeatable (Pinto et al., 2005), only the first 1000 ms of time windows were used in the analysis. Subsequent calculations were then performed using custom programs I wrote in MATLAB.

PWGC Mean Values and Distributions

The mean PWGC source value for each group was calculated by first averaging over the first 1000 ms of time windows and all channels then truncating the top and bottom 2.5% of values. Results are shown in Table 5-1. PWGC sink mean values were not calculated separately since the total PWGC source and sink values are equal.

Differing from the trend of control and high dose subjects being functionally similar using classic and spatial metrics, I found that control and low dose subjects have similar PWGC values, differing by less than 0.5%, while high dose subjects were found to have an approximately 9% decrease.

Next, probability density estimates of PWGC source and sink values by group were generated and are shown in Figure 5-1. Two-sample Kolmogorov-Smirnov tests were performed on the total PWGC source and sink distributions. Results are presented in Table 5-2. Significant differences exist between both the PWGC source and sink distributions generated by control and high dose subjects and low dose and high dose subjects. However, the distributions of PWGC source values generated from the control and low dose subjects are far more similar in comparison (source $p_{\text{control, low dose}} = 0.0335$) and that the PWGC distribution of sink values among these two groups is not statistically significant (sink $p_{\text{control, low dose}} = 0.0694$).

Although these results initially suggest a greater functional similarity between the control and low dose groups, a marked departure from the results of both classic and spatial metrics discussed previously, careful examination indicates that these findings

are not unexpected. As previously discussed, a greater degree of cortical dysplasia is generated in high dose subjects than in low dose subjects. Therefore, the morphology of low dose subjects is more similar to the control subjects and more “organized” compared to the high dose subjects. Since PWGC provides a measure of the causality between the neuron ensembles (more precisely the causality of the voltages recorded at the electrodes which are generated by neuron ensemble activity), higher mean PWGC values can be interpreted as the occurrence of a more ordered system. This is because a system that is more organized, with units that deliberately cause the activity of other units, produces a higher mean PWGC value, while a more random system, where no units exert influence over the activity of other units, produces a low mean PWGC value. Thus, the mean PWGC values verify that the control subjects exhibit the most organized structure, the high dose subjects exhibit the most random, and the low dose subjects are structurally far more similar to the controls. These findings are reinforced by the results of the two-sample Kolmogorov-Smirnov tests and visual inspection of the PWGC source and sink probability density estimates presented Figure 5-1.

Mean PWGC Values by Cell Layer

As set forth in Chapter 1, literature suggests that the infragranular layers are the site of initiation and driving force behind ictal events, while the supragranular layers are thought to mitigate epileptic activity. In order to examine this notion further, the PWGC source and sink values of each of the gross cell layers across all groups were calculated and are presented in Table 5-3. Next, probability density estimates based on these distributions were plotted and two-sample Kolmogorov-Smirnov tests were

performed on the distributions. Results are presented in Figure 5-2 and Table 5-4, respectively.

While the magnitude of the PWGC values varies among groups, four trends are maintained across all groups. First, the supragranular layers have the lowest PWGC source values. Second, the infragranular layers have the highest PWGC source values. Third, the infragranular layers have the lowest PWGC sink values. Finally, the granular layers have the highest PWGC sink values. While these trends hold for all groups, results from the two-sample Kolmogorov-Smirnov tests show that the PWGC sink distributions are not statistically significant among any cell layers in low dose subjects or between the supragranular and infragranular layers in high dose subjects. Additionally, the PWGC source distributions are not statistically significant.

The first three observed trends were expected from previous reports. As discussed earlier, literature indicates that the infragranular layers are necessary for ictal event propagation. Thus, it was expected that the infragranular layers would act as both the chief PWGC source and weakest PWGC sink. Similarly, since the supragranular layers are thought to mitigate ictal activity once it has begun and only the first 1000 ms of the ictal events were included in this analysis, it was unsurprising that supragranular layers served as the weakest PWGC source. Had a later or longer time segment of ictal activity been included in the analysis, it may have been shown that the supragranular layers were activated to a greater extent and acted as a stronger PWGC source.

While it was initially surprising that the granular layers served as the site of strongest PWGC sink values, closer analysis provides a reasonable rationale. It was

expected that the supragranular layers would be the site of greatest PWGC source values for three main reasons. First, as presented in the overview of PWGC, mediated connections generate an artificial increase in PWGC values. Second, literature reports that ictal waves propagate from the infragranular layers to the supragranular layers through the granular layers. Third, experimental results in this work discussed in Chapter 4 confirm the literature and demonstrate that ictal waves propagate from the infragranular layers to the supragranular layers through a connection mediated by the granular layers. One possibility for the apparent discrepancy may be that while the infragranular layers exert an ictal-prone effect to the granular layers, the supragranular layers simultaneously exert a controlling signal. Thus, the granular layers are effectively caught in the “crossfire” between ictal-inducing and ictal-controlling regions and their associated signals.

Finally, results from the two-sample Kolomogorov-Smirnov tests performed on the PWGC distributions by cell layer further corroborate anatomical and functional differences between the three groups. In control slices, both source and sink distributions for all cell layers are significantly different, suggesting that these three regions are anatomically and functionally distinct. Meanwhile, the two irradiated groups show a loss of significance in some PWGC distributions, indicating that some areas are affected, both anatomically and functionally, by the protocol. This is expected due to the loss of regular cortical morphology. Further leading credence to the notion of a “Goldilocks” principle applying to the amount of cortical dysplasia necessary to cause differences leading to epilepsy, low dose subjects, which exhibit less cortical dysplasia, had more distributions become homogeneous than high dose subjects, which exhibit

greater cortical dysplasia. This loss of significance in experimental groups is seen almost exclusively among PWGC sink distributions, which may arise from literature reports that the model preferentially induces changes in the inhibitory network.

PWGC Changes Over Time

Finally, since ictal events are dynamic processes, I examined changes in PWGC driving regions over time. In order to simplify analysis, I compared between PWGC source values between the supragranular and infragranular layer. This was done by plotting the ratio of the mean PWGC source values of the supragranular layers divided by the sum of the PWGC source values of infragranular layers and the PWGC source values of the supragranular layers for each time window. Thus, a value greater than 0.5 means that the supragranular layers were exerting greater control on activity than the infragranular layers and a value less than 0.5 means that the infragranular layers were dominant over the supragranular layers. A combined plot was generated for all three groups and is shown in Figure 5-4.

As shown from the graph, control and high dose subjects do not have a change in dominant driving region during the first 1000 ms of ictal activity, but differ in the layer of dominance. Infragranular layers serve as the dominant driving region in control subjects, while supragranular layers serve as the dominant driving region in high dose subjects. Low dose subjects, on the other hand begin being driven by the infragranular layers and at some point between 400 and 600 ms transition to being driven by the supragranular layers.

All three of these results were unanticipated. In the case of control subjects, and to a lesser extent the high dose subjects, it was expected that the infragranular layers, known to be necessary for ictal event propagation, to drive activity early in the event.

As the event progressed in time, it was expected that the supragranular layers, thought to mitigate ictal activity, would activate and contribute a greater role in driving the event. Since low dose subjects are the only ones to exhibit epilepsy *in vivo* and only the first 1000 ms was included in the analysis, it was expected that the supragranular layers would be the chief driving force throughout. A possible explanation for these aberrations may be due to the aforementioned errors in PWGC analysis.

Initiation Site vs. PWGC Source Focus

One of the prime questions I seek to answer through the use of Granger causality analysis is whether the observed initiation sites and dominant foci, if present, correspond to areas of maximum source values of Granger causality. To perform this analysis, total PWGC source was calculated at each electrode for the first 1000 ms of time windows and averaged together. Data were normalized and used to generate “PWGC source value heat maps”. These images were then compared to the plots used to ascertain if and where dominant initiation foci existed.

In total, eight control slices, five low dose slices, and five high dose slices exhibited PWGC source foci. Of these, one control and one low dose slice had their dominant PWGC source in the upper layers, each of the three groups had one PWGC in the middle layers, and the rest of were in the deep layers. Further, all but one low dose slice displaying a single dominant initiation focus also displayed a localized PWGC source focus. However, in the two control slices displaying two dominant initiation foci, a more diffuse PWGC source pattern was seen. It is possible that, in these slices, two separate processes generated the distinct foci, thus confounding the PWGC source image analysis.

In support of my central hypothesis that ictal driving regions do not coincide spatially with ictal initiation sites, two interesting phenomena were observed and are illustrated in Figure 5-3. First, the PWGC source foci do not correspond to the dominant initiation focus. Second, slices without dominant initiation foci often have concentrated PWGC source foci. These findings may hold significant importance in a clinical setting when resorting to surgical resection of brain tissue to deal with intractable epilepsy. Specifically, if applicable *in vivo*, localization and removal of Granger source areas, which may not correspond to seizure epicenters residing within dysplastic regions, may mitigate the loss of brain tissue while simultaneously improving surgical outcomes. Further, the finding that a localized ictal driving region can exist in tissue without a dominant initiation focus may be beneficial at targeting cortical areas for surgical resection in patients who present with cortical epilepsy in the absence of an area of dysplastic tissue.

Results From Conditional Granger Causality Analysis

Finally, conditional Granger causality analysis was performed on the ictal event data. The main goal of incorporating CGC analysis was an attempt to remove mediated connections that could have confounded the aforementioned PWGC analysis. In this section I apply the same techniques performed on PWGC data to CGC data, report the results, and note salient differences between Granger causality methods.

Analysis Methods

The same post-processed and manually verified data were used for CGC analysis. Processing methods and parameters similar to those described above with PWGC was performed with some modifications. As with PWGC, data were first down-sampled from 25 kHz to 250 and then processed through the CGC algorithms using a custom program

written in the C programming language. Again, a 200 ms window with 50% overlap parameter was used. However, CGC is a more complex analysis technique than PWGC and requires a far greater number of calculations to tease out mediated connections. Due to its intensive computational requirements, spectral information was not computed using CGC. Even omitting spectral calculations, the custom CGC program took over a week to finish processing the data on a 24-node computing cluster. Again, only the first 1000 ms of time windows were used in the analysis.

Differing from PWGC, the output of the conditional Granger causality program produces only real values and additionally generates an accompanying matrix indicating the statistical p-values of the corresponding CGC value obtained. For analysis, only CGC values with associated p-values less than 0.001 were used. Subsequent calculations were performed using custom programs I wrote in MATLAB.

CGC Mean Values and Distributions

The mean CGC value for each group was calculated by averaging over the first 1000 ms of time windows and all channels, then truncating the top and bottom 2.5% of values. Results are shown in Table 5-5. Next probability density estimates of CGC source and sink values by group were generated and are shown in Figure 5-5. Finally, two-sample Kolmogorov-Smirnov tests were performed on the total CGC source and sink distributions. Results from the statistical tests are shown in Table 5-6.

The mean CGC values show three marked differences when compared to the mean PWGC using the same data. First, the overall mean CGC values are dramatically smaller, over four orders of magnitude, than the mean PWGC values. Second, instead of the control and high dose groups being similar to one another, the two dysplastic groups have much greater commonality with each other. Specifically, the mean CGC

values of the low dose and high dose subjects are within approximately 30% of each other, while the control group mean CGC value is over 226% times larger. Third, the low dose group has the lowest mean CGC value while the high dose group had the lowest mean PWGC value.

The departures from the earlier discussed PWGC values may be the result of the removal of CGC values having an associated p-value of greater than 0.001, differences between CGC and PWGC processing (such as the removal of confounding mediating connections generating erroneous values), or a combination of the two. Thus, CGC may be giving a more accurate result of mean causality in the groups.

Mean CGC Values by Cell Layer

The mean CGC source and sink values of each gross cell layer of all groups were calculated and results are presented in Table 5-7. Probability density estimates based on the CGC value distributions of each cell layer were plotted and two-sample Kolmogorov-Smirnov tests were performed on the distributions. Results are presented in Figure 5-6 and Table 5-8, respectively.

The trends observed in the results from PWGC were not preserved. Instead, the infragranular layers exhibit both the lowest mean CGC source and sink values, and with the exception of the low dose source group, the greatest mean CGC values are found in the supragranular layer. The statistical tests indicate that the CGC source value distributions are not significantly different between the infragranular and granular layers in low dose and high dose groups and the granular and infragranular layers in the high dose group. Similarly, the CGC sink value distributions are not significantly different between the supragranular and granular control group and granular and infragranular layers in the high dose group.

Thus, CGC results differ greatly from the PWGC results and suggest that the supragranular layer is the chief driving region of activity during ictal the early phase of ictal events, rather than the infragranular layer. Although appearing to directly defy both literature and PWGC results indicating that the infragranular layers are necessary for ictal event propagation, there are at least two possible reasons the CGC results may be complimentary, rather than conflicting. First, it is possible that the infragranular layers trigger a region in the supragranular layers that then continue to drive the event. Second, the supragranular layers may be responding to ictal activity in an attempt to abate the event. Additionally, the differences in observed dominant source values with CGC may be attributable to the fact that the process successfully removed the influence of the mediated connections that were artificially inflating the infragranular layer source values in PWGC analysis.

CGC Changes Over Time

Finally, the changes in dominant CGC driving layers over time were assessed. As with PWGC, analysis was simplified by comparing the ratio of the mean CGC source values of the supragranular layers divided by the sum of the CGC source values of infragranular layers and the CGC source values of the supragranular layers for each time window. A combined plot was generated for all three groups and is shown in Figure 5-8.

Likely due to CGC removing the confounding effects of mediated connections, the CGC changes over time more closely follows the expected pattern previously discussed. The control and high dose subjects exhibit a functionally similar pattern, with the high dose subjects displaying an apparent lag. In these groups, the supragranular layer appears to be the driving region early during the ictal events, however as time

progressed, processes shift and the infragranular layers serves as the dominant region before being once again usurped by the infragranular layers. Meanwhile, the low dose subjects began ictal events with a slight bias towards the supragranular layers as the driving region. Dominance quickly shifts to the infragranular layers and continues throughout the analyzed time window. This functional difference in the low dose group is also expected, since it suggests that the supragranular layers, thought to suppress ictal activity, are unable to sufficiently activate and thus abate the event.

Initiation Site vs. CGC Source Focus

In order to provide deeper investigation into whether dominant driving regions within slice correspond to dominant initiation foci, heat maps were generated from total CGC source values in the first 1000 ms of time windows and compared to initiation plots. In total, four control subjects, two low dose subjects, and four high dose subjects demonstrated strong localized CGC driving foci. Again, as with PWGC, CGC shows strong driving foci in locations other than the dominant initiation focus and localized driving foci in slices that do not have a dominant initiation focus. Figure 5-7 provides two such examples. Two expected differences are observed between the CGC analysis and the PWGC analysis. First, some slices do not display dominant driving CGC foci, but do display dominant driving PWGC foci. Second, some slices absent of dominant PWGC foci display strong CGC driving foci. Additionally, an unexpected change from the PWGC also is noted. PWGC driving regions often appeared to be located towards the middle of the electrode array, while CGC driving regions were not restricted to the center region of the array. This discrepancy may arise due to two possible mechanisms. First, mediating connections may confound PWGC analysis. Since waves propagate from the lower layers to the upper layers through the middle layers,

PWGC may erroneously over estimate the causal values of the center layers. Second, CGC may be able to successfully remove the over estimated value of the mediated connections towards the center of the array, while electrodes on the border of the array have less possible connections to remove. As with PWGC analysis, results from CGC analysis provide further evidence that the central hypothesis is correct.

Summary of Granger Causality Analysis

Pairwise and Conditional Granger Causality were used to analyze spontaneous epileptiform activity recorded from both normally laminated and dysplastic cortical acute rat cortical slices. Some conflicting results arose from the two techniques, but were likely due to known shortcomings with PWGC. Both techniques provided evidence suggesting key functional differences, almost certainly arising from morphological changes, between normally laminated and dysplastic slices. Most importantly, the findings from this analysis suggest that the central hypothesis was confirmed.

Table 5-1. Mean pairwise Granger Causality values of each group

	Mean PWGC Value
Control	344.4622
Low dose	342.9090
High dose	311.3465

Table 5-2. Results of two-sample Kolmogorov-Smirnov tests on pairwise Granger Causality distributions between groups

	PWGC Source Values	PWGC Sink Values
Control vs. Low dose	0.0335	0.0694
Control vs. High dose	2.4679×10^{-79}	1.4588×10^{-64}
Low Dose vs. High dose	1.8455×10^{-81}	1.1910×10^{-51}

Table 5-3. Mean PWGC in each cell layer

	Mean supragranular PWGC Value	Mean granular layer PWGC Value	Mean infragranular PWGC Value
Control source	295.9778	344.6329	370.4592
Control sink	352.3007	372.7259	318.5575
Low dose source	266.6269	326.1246	351.9793
Low dose sink	328.2719	334.2669	317.7433
High dose source	274.0517	327.9370	405.4087
High dose sink	354.9639	409.3771	326.6135

Table 5-4. Results of two-sample Kolmogorov-Smirnov tests on pairwise Granger Causality distributions between cell layers

	PWGC Source Values	PWGC Sink Values
Control supragranular vs. Control granular	0.0140	0.0300
Control supragranular vs. Control infragranular	4.1510×10^{-6}	0.0224
Control granular vs. Control infragranular	0.0068	0.0018
Low dose supragranular vs. Low dose granular	0.0290	0.0875
Low dose supragranular vs. Low dose infragranular	2.3955×10^{-6}	0.2163
Low dose granular vs. Low dose infragranular	0.2704	0.0825
High dose supragranular vs. High dose granular	0.0187	0.0364
High dose supragranular vs. High dose infragranular	1.6708×10^{-9}	0.0754
High dose granular vs. High dose infragranular	0.0064	0.0045

Table 5-5. Mean conditional Granger Causality values of each group

Mean CGC Value	
Control	0.1764
Low dose	0.0538
High dose	0.0778

Table 5-6. Results of two-sample Kolmogorov-Smirnov tests on conditional Granger Causality values between groups

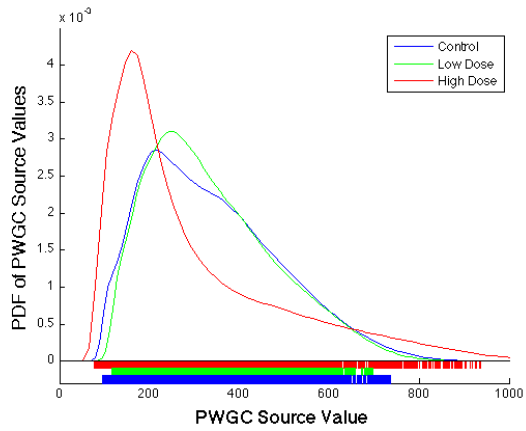
	CGC Source Values	CGC Sink Values
Control vs. Low dose	2.6076×10^{-20}	7.9976×10^{-23}
Control vs. High dose	7.6837×10^{-5}	0.0023
Low Dose vs. High dose	3.2594×10^{-33}	3.0699×10^{-13}

Table 5-7. Mean CGC in each cell layer

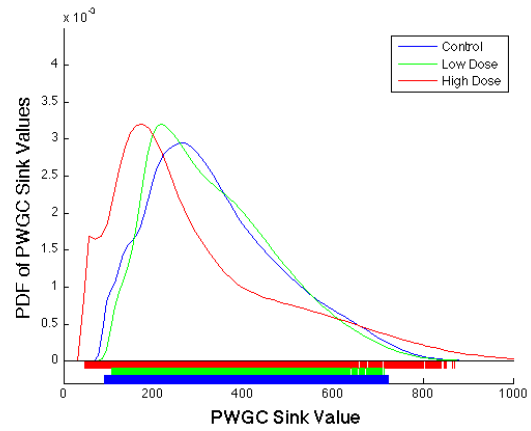
	Mean supragranular CGC Value	Mean granular layer CGC Value	Mean infragranular CGC Value
Control source	0.1519	0.1343	0.1118
Control sink	0.1475	0.1422	0.1190
Low dose source	0.0775	0.0815	0.0592
Low dose sink	0.0993	0.0569	0.0418
High dose source	0.1088	0.1080	0.0921
High dose sink	0.1287	0.0992	0.0957

Table 5-8. Results of two-sample Kolmogorov-Smirnov tests on conditional Granger Causality values between cell layers

	CGC Source Values	CGC Sink Values
Control supragranular vs. Control granular	0.0160	0.0908
Control supragranular vs. Control infragranular	2.0765×10^{-4}	0.0211
Control granular vs. Control infragranular	0.0331	0.0310
Low dose supragranular vs. Low dose granular	0.5618	0.0033
Low dose supragranular vs. Low dose infragranular	3.8213×10^{-4}	4.0837×10^{-10}
Low dose granular vs. Low dose infragranular	0.0198	0.0406
High dose supragranular vs. High dose granular	0.9427	0.0044
High dose supragranular vs. High dose infragranular	0.0075	0.0012
High dose granular vs. High dose infragranular	0.0533	0.5434



A



B

Figure 5-1. Probability density estimates of pairwise Granger Causality values by group. A) Probability density estimate of PWGC source values. B) Probability density estimate of PWGC sink values.

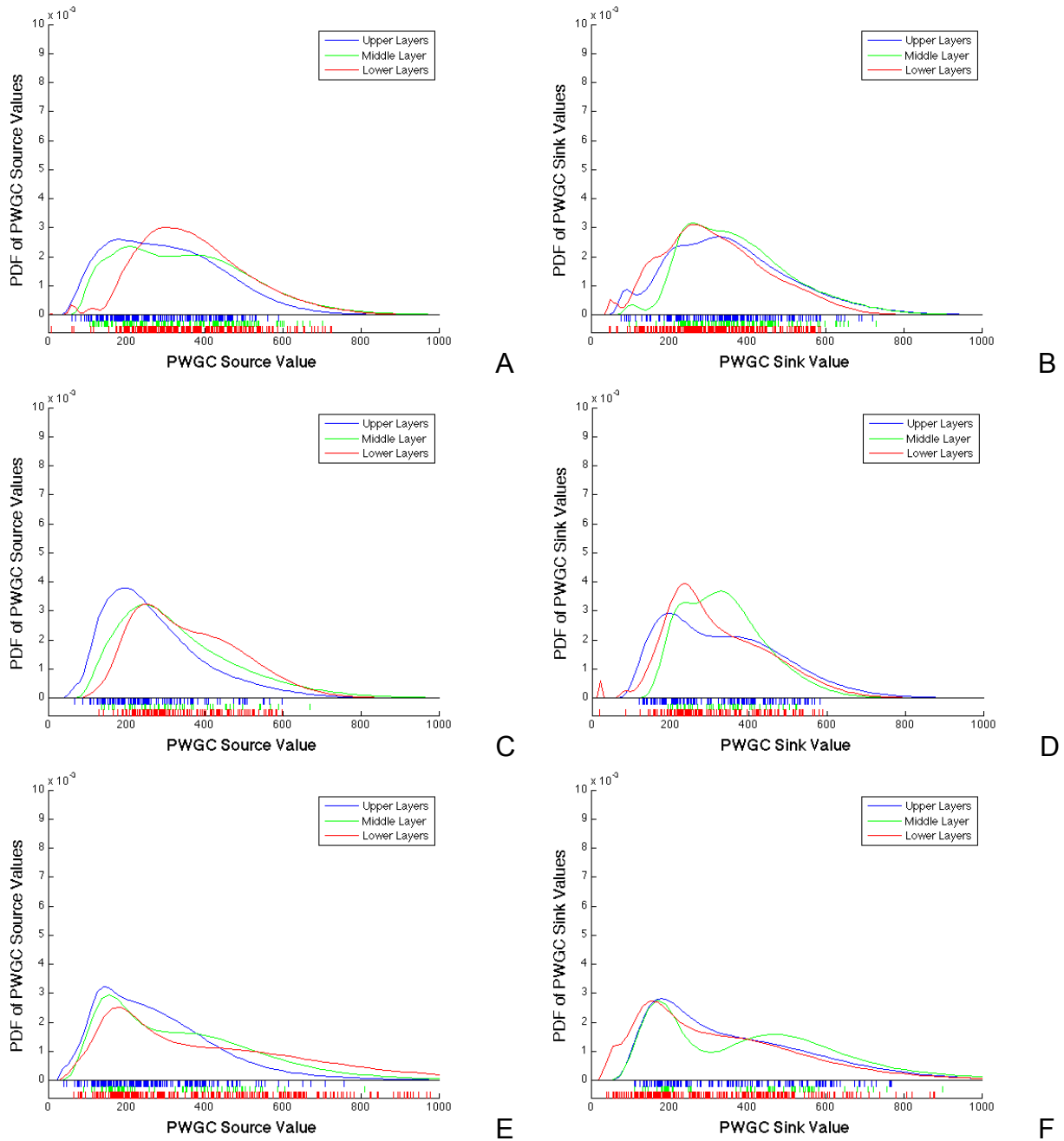


Figure 5-2. Probability density estimates of pairwise Granger source and sink values among groups by cell layer. A) Probability density estimates of PWGC source values in control subjects. B) Probability density estimates of PWGC sink values in control subjects. C) Probability density estimates of PWGC source values in low dose subjects. D) Probability density estimates of PWGC sink values in low dose subjects. E) Probability density estimates of PWGC source values in high dose subjects. F) Probability density estimates of PWGC sink values in high dose subjects.

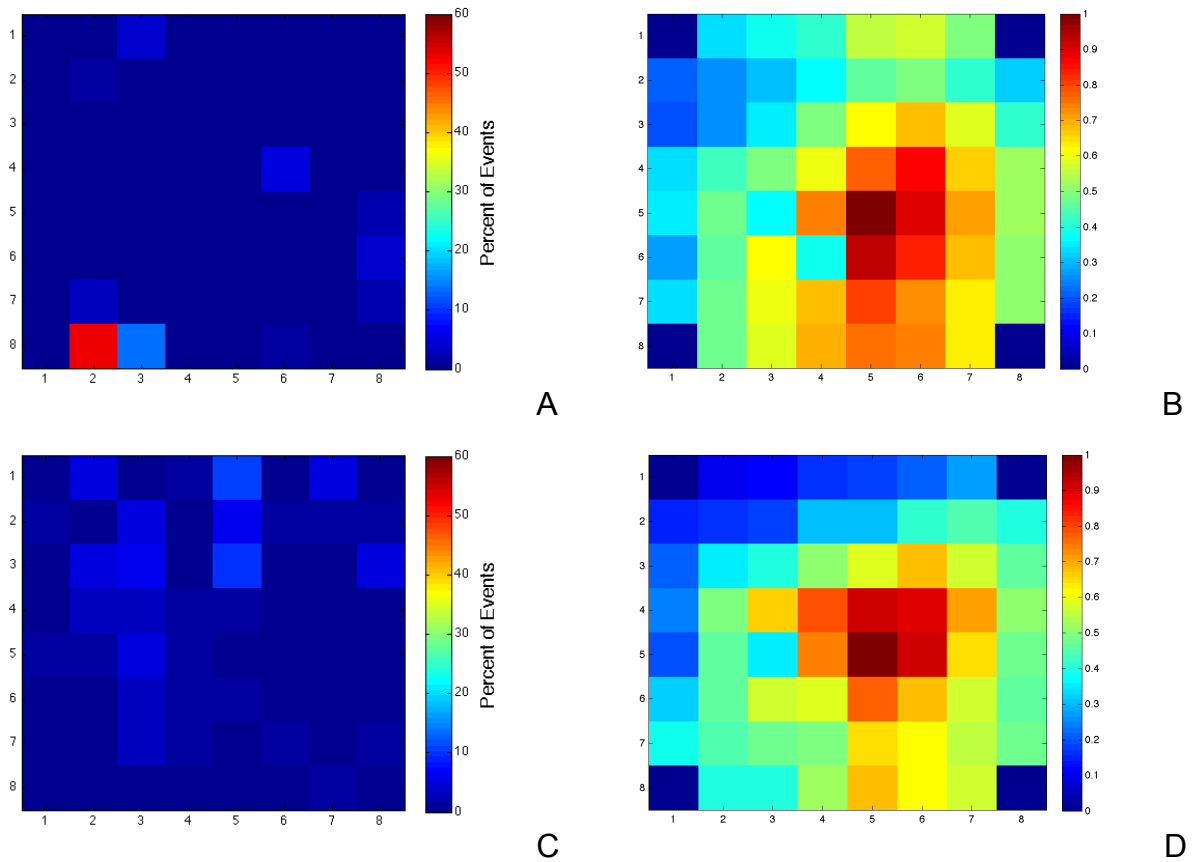


Figure 5-3. Comparison between initiation focus and PWGC source. A) Initiation site heat map of a control slice exhibiting strongly dominant initiation focus in the infragranular layer. B) Normalized total PWGC source plot of slice in A demonstrating that the causal driving focus is separate from the dominant initiation site. C) Initiation site heat map of a control slice showing a diffuse initiation pattern. D) Normalized total PWGC source plot of slice in C demonstrating that even though a dominant initiation site is absent, a strongly localized PWGC source is present.

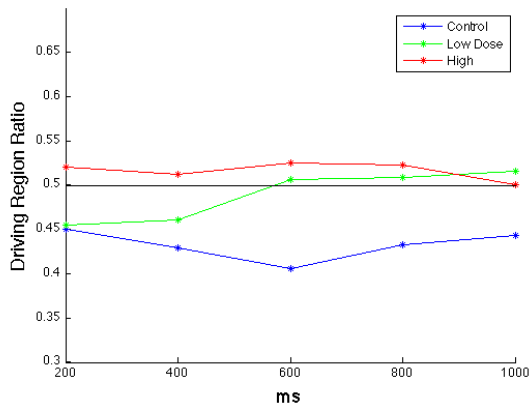


Figure 5-4. PWGC driving region over time. Values greater than 0.5 indicate that the supragranular layers are driving the ictal event while values less than 0.5 indicate that the infragranular layers are driving the event.

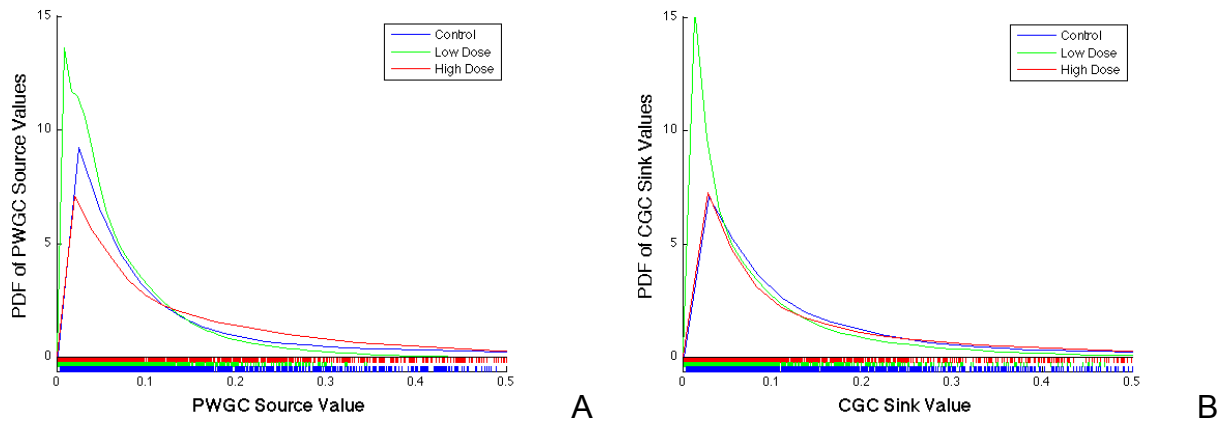


Figure 5-5. Probability density estimates of conditional Granger Causality values by group. A) Probability density estimate of CGC source values. B) Probability density estimate of CGC sink values.

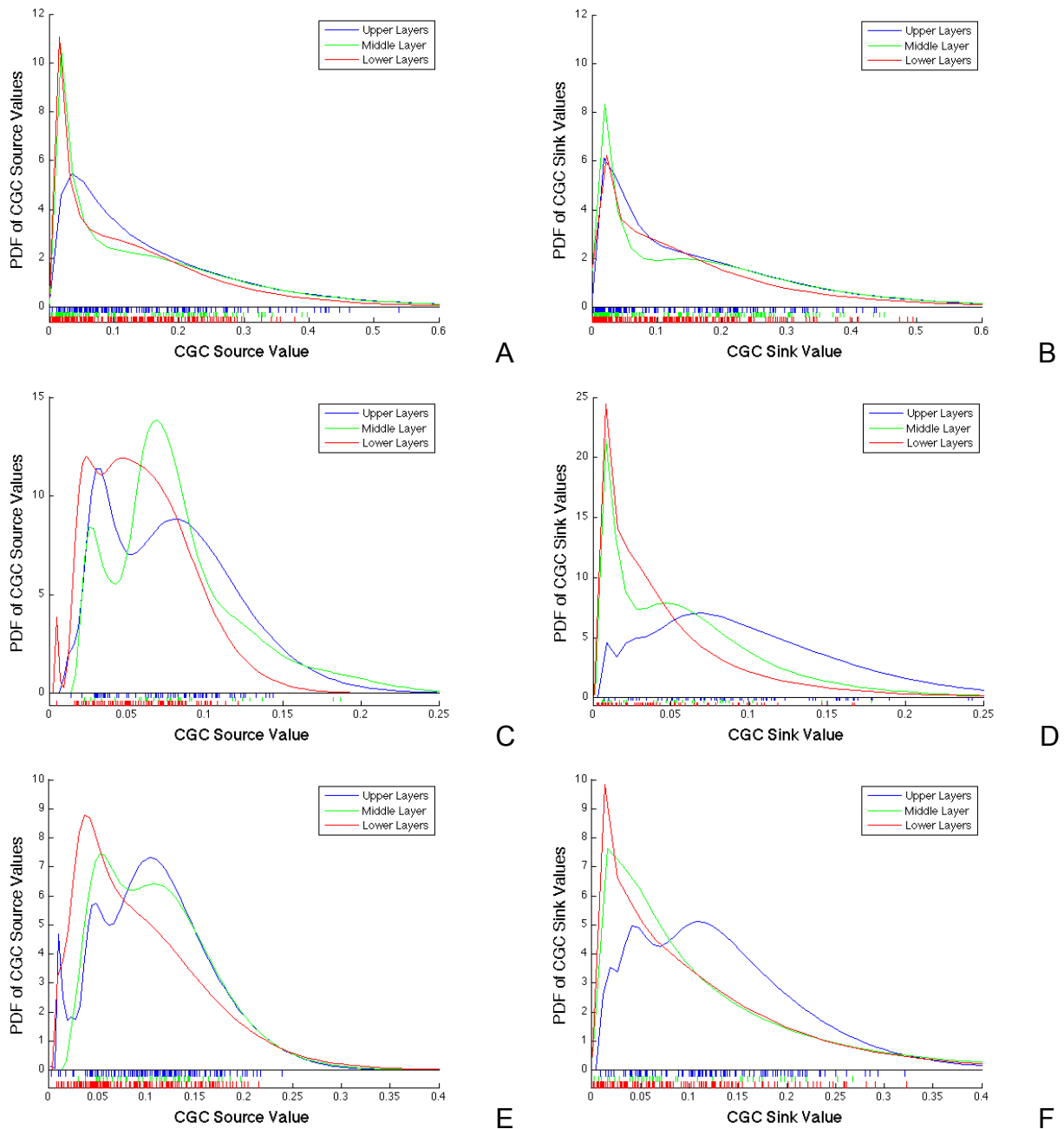


Figure 5-6. CGC Source and Sink values by layer. A) Probability density estimates of CGC source values in control subjects. B) Probability density estimates of CGC sink values in control subjects. C) Probability density estimates of CGC source values in low dose subjects. D) Probability density estimates of CGC sink values in low dose subjects. E) Probability density estimates of CGC source values in high dose subjects. F) Probability density estimates of CGC sink values in high dose subjects.

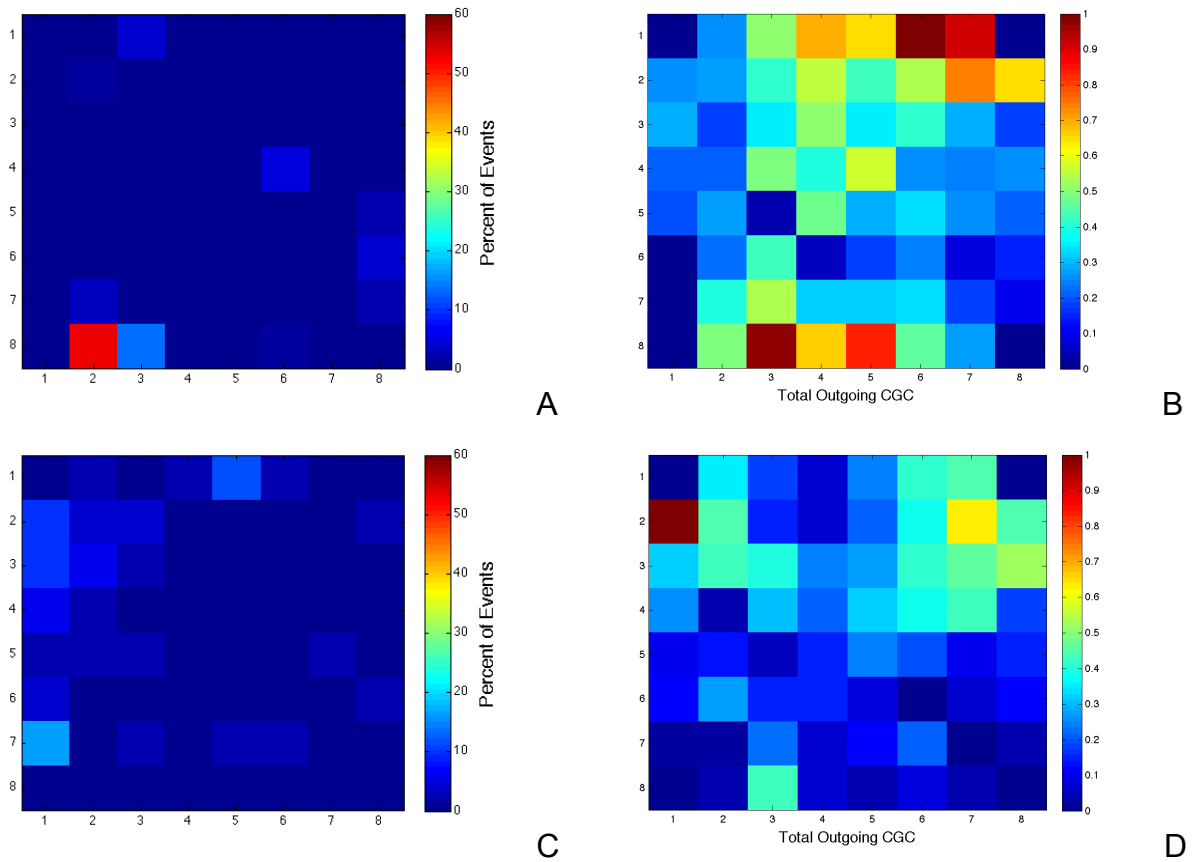


Figure 5-7. Comparison between initiation focus and CGC source. A) Initiation site heat map of a control slice exhibiting strongly dominant initiation focus in the infragranular layer. B) Normalized total CGC source plot of slice in A demonstrating that the CG driving focus is may be a diffuse process even if a dominant initiation site is present. C) Initiation site heat map of a control slice showing a diffuse initiation pattern. D) Normalized total CGC source plot of slice in C demonstrating that strongly localized CGC sources may be present, even though a dominant initiation site is absent.

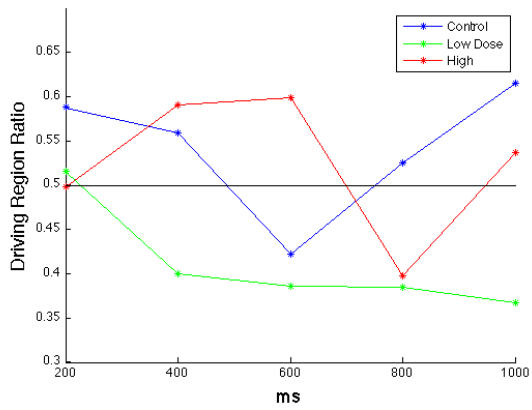


Figure 5-8. CGC driving region over time. Values greater than 0.5 indicate that the supragranular layers are driving the ictal event while values less than 0.5 indicate that the infragranular layers are driving the event.

CHAPTER 6 CONCLUSIONS

Conclusions

This work provides a detailed analysis and comparison of electrophysiological activity during seizure-like events in normally laminated and *in utero* irradiation induced dysplastic acute rat cortical slices. Novel application of spatial metrics were performed on dysplastic tissue and compared with normally laminated controls. Further, pairwise Granger causality and conditional Granger causality analysis were applied to data collected using MEAs from both normally laminated and dysplastic cortical slices.

In general, the results indicate that the activity from low dose irradiated subjects, or mildly dysplastic tissue, is functionally more dissimilar from controls than from high dose irradiated subjects, or severely dysplastic tissue. This was observed particularly with classic metrics, such as the mean number of ictal events per recording time, mean event length, mean inter-event interval, bias in LFP extrema peaks during events, and spatial metrics, such as wave speed propagation through cortical layers. These results are consistent with previous reports that *in utero* exposure to lower doses of radiation generates spontaneously epileptic animals, while higher doses of radiation, although generating more severe dysplasia does not.

A number of novel contributions to the field were provided, including providing wave speed calculations and qualitative comparisons of wave propagation in dysplastic cortical tissue to that of normally laminated. Most notable was the application of Granger causality analysis to acute *in vitro* slice recordings. Holding the most promise for potential clinical applications were the findings suggesting that the central hypothesis: that localized areas may serve to drive ictal events in the absence of a well

defined dominant ictal initiation focus and that even if a well defined dominant initiation focus exists, its location does not necessarily coincide with the location of the driving region—is true.

Future Work

The focus of this work was to further characterize differences in seizure-like activity in normally laminated and dysplastic cortical slices caused by *in utero* irradiation, which has been demonstrated to generate epileptic animals *in vivo*. These techniques could be employed to compare other current models of epilepsy, including those that have also been observed to generate epileptic animals, such as *in utero* application of MAM and kindling, and those that have not, such as neonatal freeze lesioning model, to one another.

Additionally, this body of work has produced a rich source of data that can later be mined. A number of other data analysis methods could easily be applied to this data set. Recommendations include using principle component analysis coupled with clustering algorithms to characterize and compare individual ictal events between one another and experimental groups, spectral analysis of the ictal events using power spectral density or spectrograms, and finally PWGC and CGC spectral analysis to see if causality measures differ at known brain oscillations frequencies (e.g.: the alpha, beta, and gamma rhythms).

Expanding on the theme of using MEAs to examine hyperexcitable cortical tissue, additional experiments could be performed on neural tissue. Recommendations include comparing electrophysiological activity in control, *in utero* irradiated, and “second-hit” animals, or animals which have suffered two distinct insults and has been demonstrated

to have a higher success rate at generating spontaneously epileptic animals than singular insults.

Finally, future work should focus on if the central hypothesis holds for *in vivo* animals and whether or not the distances separating ictal initiation site and driving region are clinically significant. This should be approached on three fronts. First, more detailed and computationally intensive Granger Causality analysis of the present data set should be performed. This includes the aforementioned spectral analysis, as well as processing the data with less (or no) downsampling and a finer temporal resolution. Second, *in vivo* studies on animal models should be performed. Finally, analysis of electrophysiological data from human patients should be analyzed with these techniques.

LIST OF REFERENCES

- Abdel Razek AA, Kandell AY, Elsorogy LG, Elmongy A, Basett AA (2009) Disorders of cortical formation: MR imaging features. *AJNR Am J Neuroradiol* 30:4-11.
- Albensi BC, Ata G, Schmidt E, Waterman JD, Janigro D (2004) Activation of long-term synaptic plasticity causes suppression of epileptiform activity in rat hippocampal slices. *Brain Res* 998:56-64.
- Altman J, Anderson WJ, Wright KA (1968) Differential radiosensitivity of stationary and migratory primitive cells in the brains of infant rats. *Exp Neurol* 22:52-74.
- Altman J, Bayer SA (1995) *Atlas of Prenatal Rat Brain Development*. Boca Raton, FL: CRC Press, Inc..
- Amano S, Ihara N, Uemura S, Yokoyama M, Ikeda M, Serikawa T, Sasahara M, Kataoka H, Hayase Y, Hazama F (1996) Development of a novel rat mutant with spontaneous limbic-like seizures. *Am J Pathol* 149:329-336.
- Amitai Y (1994) Membrane potential oscillations underlying firing patterns in neocortical neurons. *Neuroscience* 63:151-161.
- (2009) *Animal Models of Epilepsy* (Baraban SC, eds). New York, NY: Humana Press.
- Ashwell KWS, Paxinos G (2008) *Atlas of the Developing Rat Nervous System*. San Diego, CA: Academic Press.
- Aykut-Bingol C, Bronen RA, Kim JH, Spencer DD, Spencer SS (1998) Surgical outcome in occipital lobe epilepsy: implications for pathophysiology. *Ann Neurol* 44:60-69.
- Bai L, Huang X, Yang Q, Wu JY (2006) Spatiotemporal patterns of an evoked network oscillation in neocortical slices: coupled local oscillators. *J Neurophysiol* 96:2528-2538.
- Baker BJ, Kosmidis EK, Vucinic D, Falk CX, Cohen LB, Djuricic M, Zecevic D (2005) Imaging brain activity with voltage- and calcium-sensitive dyes. *Cell Mol Neurobiol* 25:245-282.
- Bakker R, Schubert D, Levels K, Bezgin G, Bojak I, Kötter R (2009) Classification of cortical microcircuits based on micro-electrode-array data from slices of rat barrel cortex. *Neural Netw* 22:1159-1168.
- Baraban SC, Wenzel HJ, Hochman DW, Schwartzkroin PA (2000) Characterization of heterotopic cell clusters in the hippocampus of rats exposed to methylazoxymethanol in utero. *Epilepsy Res* 39:87-102.

- Barkai E, Friedman A, Grossman Y, Gutnick MJ (1995) Laminar pattern of synaptic inhibition during convulsive activity induced by 4-aminopyridine in neocortical slices. *J Neurophysiol* 73:1462-1467.
- Barkovich AJ (2005) Malformations of cortical development. In: *Magnetic Resonance in Epilepsy* (Ruben RI, Jackson GD, eds), pp221-248. Burlington, MA: Elsevier Academic Press.
- Barkovich AJ, Kuzniecky RI, Dobyns WB, Jackson GD, Becker LE, Evrard P (1996) A classification scheme for malformations of cortical development. *Neuropediatrics* 27:59-63.
- Barkovich AJ, Kuzniecky RI, Jackson GD, Guerrini R, Dobyns WB (2001) Classification system for malformations of cortical development: update 2001. *Neurology* 57:2168-2178.
- Bayer SA, Altman J (1991) *Neocortical Development*. New York, NY: Raven Press.
- Beggs JM, Plenz D (2004) Neuronal avalanches are diverse and precise activity patterns that are stable for many hours in cortical slice cultures. *J Neurosci* 24:5216-5229.
- Begley CE, Famulari M, Annegers JF, Lairson DR, Reynolds TF, Coan S, Dubinsky S, Newmark ME, Leibson C, So EL, Rocca WA (2000) The cost of epilepsy in the United States: an estimate from population-based clinical and survey data. *Epilepsia* 41:342-351.
- Benardete EA, Kriegstein AR (2002) Increased excitability and decreased sensitivity to GABA in an animal model of dysplastic cortex. *Epilepsia* 43:970-982.
- Bikson M, Hahn PJ, Fox JE, Jefferys JG (2003) Depolarization block of neurons during maintenance of electrographic seizures. *J Neurophysiol* 90:2402-2408.
- Bollimunta A, Chen Y, Schroeder CE, Ding M (2008) Neuronal mechanisms of cortical alpha oscillations in awake-behaving macaques. *J Neurosci* 28:9976-9988.
- Borbély S, Halasy K, Somogyvári Z, Détéri L, Világi I (2006) Laminar analysis of initiation and spread of epileptiform discharges in three in vitro models. *Brain Res Bull* 69:161-167.
- Bressloff PC (2001) Traveling fronts and wave propagation failure in an inhomogeneous neural network. *PHYSICA D* 155:83-100.
- Brodmann K (1909) *Vergleichende Lokalisationslehre der Großhirnrinde in ihren Prinzipien dargestellt auf Grund des Zellenbaues*. Leipzig: JA Barth.

- Canepari M, Bove M, Maeda E, Cappello M, Kawana A (1997) Experimental analysis of neuronal dynamics in cultured cortical networks and transitions between different patterns of activity. *Biol Cybern* 77:153-162.
- (1990) *The Cerebral Cortex of the Rat* (Kolb B, Tees RC, eds). Cambridge, MA: MIT Press.
- Chae T, Kwon YT, Bronson R, Dikkes P, Li E, Tsai LH (1997) Mice lacking p35, a neuronal specific activator of Cdk5, display cortical lamination defects, seizures, and adult lethality. *Neuron* 18:29-42.
- Chagnac-Amitai Y, Connors BW (1989a) Horizontal spread of synchronized activity in neocortex and its control by GABA-mediated inhibition. *J Neurophysiol* 61:747-758.
- Chagnac-Amitai Y, Connors BW (1989b) Synchronized excitation and inhibition driven by intrinsically bursting neurons in neocortex. *J Neurophysiol* 62:1149-1162.
- Chagnac-Amitai Y, Luhmann HJ, Prince DA (1990) Burst generating and regular spiking layer 5 pyramidal neurons of rat neocortex have different morphological features. *J Comp Neurol* 296:598-613.
- Chen HX, Roper SN (2003) Reduction of spontaneous inhibitory synaptic activity in experimental heterotopic gray matter. *J Neurophysiol* 89:150-158.
- Chen HX, Xiang H, Roper SN (2007) Impaired developmental switch of short-term plasticity in pyramidal cells of dysplastic cortex. *Epilepsia* 48:141-148.
- Chervin RD, Pierce PA, Connors BW (1988) Periodicity and directionality in the propagation of epileptiform discharges across neocortex. *J Neurophysiol* 60:1695-1713.
- Chiappalone M, Bove M, Vato A, Tedesco M, Martinoia S (2006) Dissociated cortical networks show spontaneously correlated activity patterns during in vitro development. *Brain Res* 1093:41-53.
- Chiappalone M, Vato A, Tedesco MB, Marcoli M, Davide F, Martinoia S (2003) Networks of neurons coupled to microelectrode arrays: a neuronal sensory system for pharmacological applications. *Biosens Bioelectron* 18:627-634.
- Chisholm D, WHO-CHOICE (2005) Cost-effectiveness of first-line antiepileptic drug treatments in the developing world: a population-level analysis. *Epilepsia* 46:751-759.
- Cohen LB, Leshner S (1986) Optical monitoring of membrane potential: methods of multisite optical measurement. *Soc Gen Physiol Ser* 40:71-99.

- Connolly P, Clark P, Curtis AS, Dow JA, Wilkinson CD (1990) An extracellular microelectrode array for monitoring electrogenic cells in culture. *Biosens Bioelectron* 5:223-234.
- Connors BW (1984) Initiation of synchronized neuronal bursting in neocortex. *Nature* 310:685-687.
- Connors BW, Amitai Y (1993) Generation of Epileptiform Discharge by Local Circuits of the Neocortex. In: *Epilepsy* (Schwartzkroin PA, eds), pp388-423. Cambridge, UK: Cambridge University Press.
- Connors BW, Gutnick MJ, Prince DA (1982) Electrophysiological properties of neocortical neurons in vitro. *J Neurophysiol* 48:1302-1320.
- Contreras D, Destexhe A, Sejnowski TJ, Steriade M (1996) Control of spatiotemporal coherence of a thalamic oscillation by corticothalamic feedback. *Science* 274:771-774.
- Contreras D, Destexhe A, Sejnowski TJ, Steriade M (1997) Spatiotemporal patterns of spindle oscillations in cortex and thalamus. *J Neurosci* 17:1179-1196.
- Contreras D, Llinás R (2001) Voltage-sensitive dye imaging of neocortical spatiotemporal dynamics to afferent activation frequency. *J Neurosci* 21:9403-9413.
- Cooley RK (2005) *Stereotaxic Surgery in the Rat*. London, Ontario: A J Kirby Company.
- Cowen D, Geller LM, Wolf A (1970) Healing in the cerebral cortex of the infant rat after closed-head focal injury. *J Neuropathol Exp Neurol* 29:21-42.
- D'Antuono M, Benini R, Biagini G, D'Arcangelo G, Barbarosie M, Tancredi V, Avoli M (2002) Limbic network interactions leading to hyperexcitability in a model of temporal lobe epilepsy. *J Neurophysiol* 87:634-639.
- D'Arcangelo G, Panuccio G, Tancredi V, Avoli M (2005) Repetitive low-frequency stimulation reduces epileptiform synchronization in limbic neuronal networks. *Neurobiol Dis* 19:119-128.
- D'Arcangelo G, Tancredi V, Avoli M (2001) Intrinsic optical signals and electrographic seizures in the rat limbic system. *Neurobiol Dis* 8:993-1005.
- Demir R, Haberly LB, Jackson MB (1999) Sustained and accelerating activity at two discrete sites generate epileptiform discharges in slices of piriform cortex. *J Neurosci* 19:1294-1306.
- Destexhe A, Contreras D, Steriade M (1999) Spatiotemporal analysis of local field potentials and unit discharges in cat cerebral cortex during natural wake and sleep states. *J Neurosci* 19:4595-4608.

- Deukmedjian AJ, King MA, Cuda C, Roper SN (2004) The GABAergic system of the developing neocortex has a reduced capacity to recover from in utero injury in experimental cortical dysplasia. *J Neuropathol Exp Neurol* 63:1265-1273.
- Dhillon A, Jones RS (2000) Laminar differences in recurrent excitatory transmission in the rat entorhinal cortex in vitro. *Neuroscience* 99:413-422.
- Ding M, Chen Y, Bressler SL (2006) Granger Causality: Basic Theory and Application to Neuroscience. In: *Handbook of Time Series Analysis: Recent Theoretical Developments and Applications* (Schelter B, Winterhalder M, Timmer J, eds), pp437-460. Berlin: Wiley-VCH Verlag GMBh & Co.
- Dudek EE, Clark S, Williams PA, Grabenstatter HL (2006) Kainate-Induced Status Epilepticus: a Chronic Model of Acquired Epilepsy. In: *Models of Seizure and Epilepsy* (Pitkänen A, Schwartzkroin PA, Moshé SL, eds), pp415-432. Burlington, MA: Elsevier Academic Press.
- Duffy S, MacVicar BA (1999) Modulation of neuronal excitability by astrocytes. *Adv Neurol* 79:573-581.
- Egert U, Heck D, Aertsen A (2002) Two-dimensional monitoring of spiking networks in acute brain slices. *Exp Brain Res* 142:268-274.
- Egert U, Schlosshauer B, Fennrich S, Nisch W, Fejtli M, Knott T, Müller T, Hammerle H (1998) A novel organotypic long-term culture of the rat hippocampus on substrate-integrated multielectrode arrays. *Brain Res Brain Res Protoc* 2:229-242.
- Engel J (1992) Experimental animal models of epilepsy: classification and relevance to human epileptic phenomena. *Epilepsy Res Suppl* 8:9-20.
- Ermentrout B (1998) Neural networks as spatio-temporal pattern-forming systems. *REP PROG PHYS* 61:353-430.
- Farrell MA, DeRosa MJ, Curran JG, Secor DL, Cornford ME, Comair YG, Peacock WJ, Shields WD, Vinters HV (1992) Neuropathologic findings in cortical resections (including hemispherectomies) performed for the treatment of intractable childhood epilepsy. *Acta Neuropathol* 83:246-259.
- Ferrer I, Pineda M, Tallada M, Oliver B, Russi A, Oller L, Noboa R, Zújar MJ, Alcántara S (1992) Abnormal local-circuit neurons in epilepsia partialis continua associated with focal cortical dysplasia. *Acta Neuropathol* 83:647-652.
- Ferrer I, Santamaría J, Alcántara S, Zújar MJ, Cinós C (1993a) Neuronal ectopic masses induced by prenatal irradiation in the rat. *Virchows Arch A Pathol Anat Histopathol* 422:1-6.

- Ferrer I, Serrano T, Alcantara S, Tortosa A, Graus F (1993b) X-ray-induced cell death in the developing hippocampal complex involves neurons and requires protein synthesis. *J Neuropathol Exp Neurol* 52:370-378.
- Fisher RS, van Emde Boas W, Blume W, Elger C, Genton P, Lee P, Engel J (2005) Epileptic seizures and epilepsy: definitions proposed by the International League Against Epilepsy (ILAE) and the International Bureau for Epilepsy (IBE). *Epilepsia* 46:470-472.
- Flint AC, Connors BW (1996) Two types of network oscillations in neocortex mediated by distinct glutamate receptor subtypes and neuronal populations. *J Neurophysiol* 75:951-957.
- Foster GA (1998) *Chemical Neuroanatomy of the Prenatal Rat Brain*. New York, NY: Oxford University Press.
- Fox JW, Lamperti ED, Ekşioğlu YZ, Hong SE, Feng Y, Graham DA, Scheffer IE, Dobyns WB, Hirsch BA, Radtke RA, Berkovic SF, Huttenlocher PR, Walsh CA (1998) Mutations in filamin 1 prevent migration of cerebral cortical neurons in human periventricular heterotopia. *Neuron* 21:1315-1325.
- French JA, Kanner AM, Bautista J, Abou-Khalil B, Browne T, Harden CL, Theodore WH, Bazil C, Stern J, Schachter SC, Bergen D, Hirtz D, Montouris GD, Nespeca M, Gidal B, Marks WJ, Turk WR, Fischer JH, Bourgeois B, Wilner A, Faught RE, Sachdeo RC, Beydoun A, Glauser TA, American Academy of Neurology Therapeutics and Technology Assessment Subcommittee, American Academy of Neurology Quality Standards Subcommittee, American Epilepsy Society Quality Standards Subcommittee, American Epilepsy Society Therapeutics and Technology Assessment Subcommittee (2004) Efficacy and tolerability of the new antiepileptic drugs, I: Treatment of new-onset epilepsy: report of the TTA and QSS Subcommittees of the American Academy of Neurology and the American Epilepsy Society. *Epilepsia* 45:401-409.
- Fukui Y, Hoshino K, Hayasaka I, Inouye M, Kameyama Y (1991) Developmental disturbance of rat cerebral cortex following prenatal low-dose gamma-irradiation: a quantitative study. *Exp Neurol* 112:292-298.
- Fushiki S, Matsushita K, Yoshioka H, Schull WJ (1996) In utero exposure to low-doses of ionizing radiation decelerates neuronal migration in the developing rat brain. *Int J Radiat Biol* 70:53-60.
- Garnett WR (2000) Antiepileptic drug treatment: outcomes and adherence. *Pharmacotherapy* 20:191S-199S.
- Geweke J (1982) Measurement of Linear-Dependence and Feedback between Multiple Time-Series. *Journal of the American Statistical Association* 77:304-313.

- Geweke JF (1984) Measures of Conditional Linear-Dependence and Feedback between Time-Series. *Journal of the American Statistical Association* 79:907-915.
- Gleeson JG, Allen KM, Fox JW, Lamperti ED, Berkovic S, Scheffer I, Cooper EC, Dobyns WB, Minnerath SR, Ross ME, Walsh CA (1998) Doublecortin, a brain-specific gene mutated in human X-linked lissencephaly and double cortex syndrome, encodes a putative signaling protein. *Cell* 92:63-72.
- Goddard GV (1967) Development of epileptic seizures through brain stimulation at low intensity. *Nature* 214:1020-1021.
- Goebel R, Roebroeck A, Kim DS, Formisano E (2003) Investigating directed cortical interactions in time-resolved fMRI data using vector autoregressive modeling and Granger causality mapping. *Magn Reson Imaging* 21:1251-1261.
- Golomb D, Amitai Y (1997) Propagating neuronal discharges in neocortical slices: computational and experimental study. *J Neurophysiol* 78:1199-1211.
- Gottlieb JP, Keller A (1997) Intrinsic circuitry and physiological properties of pyramidal neurons in rat barrel cortex. *Exp Brain Res* 115:47-60.
- Granata T, Farina L, Faiella A, Cardini R, D'Incerti L, Boncinelli E, Battaglia G (1997) Familial schizencephaly associated with EMX2 mutation. *Neurology* 48:1403-1406.
- Granger CWJ (1969) Investigating causal relations by econometric models and cross-spectral methods. *Econometrica* 37:424-438.
- Greenwood RS (2000) Adverse effects of antiepileptic drugs. *Epilepsia* 41 Suppl 2:S42-S52.
- Grinvald A, Anglister L, Freeman JA, Hildesheim R, Manker A (1984) Real-time optical imaging of naturally evoked electrical activity in intact frog brain. *Nature* 308:848-850.
- Gross GW, Rieske E, Kreutzberg GW, Meyer A (1977) A new fixed-array multielectrode system designed for long-term monitoring of extracellular single unit neuronal activity in vitro. *Neurosci Lett* 6:101-105.
- Grumet AE, Wyatt JL, Rizzo JF (2000) Multi-electrode stimulation and recording in the isolated retina. *J Neurosci Methods* 101:31-42.
- Guerrini R, Holthausen H, Parmeggiani L, Chiron C (2002) Epilepsy and malformations of the cerebral cortex. In: *Epileptic Syndromes in Infancy, Childhood and Adolescence* (Roger, eds), pp457-479. London, UK: John Libbeyerd.

- Gulyás-Kovács A, Dóczy J, Tarnawa I, Détári L, Banczerowski-Pelyhe I, Világi I (2002) Comparison of spontaneous and evoked epileptiform activity in three in vitro epilepsy models. *Brain Res* 945:174-180.
- Gutnick MJ, Prince DA (1972) Thalamocortical relay neurons: antidromic invasion of spikes from a cortical epileptogenic focus. *Science* 176:424-426.
- de Guzman P, Inaba Y, Baldelli E, de Curtis M, Biagini G, Avoli M (2008) Network hyperexcitability within the deep layers of the pilocarpine-treated rat entorhinal cortex. *J Physiol* 586:1867-1883.
- Hardiman O, Burke T, Phillips J, Murphy S, O'Moore B, Staunton H, Farrell MA (1988) Microdysgenesis in resected temporal neocortex: incidence and clinical significance in focal epilepsy. *Neurology* 38:1041-1047.
- Harrington EP, Möddel G, Najm IM, Baraban SC (2007) Altered glutamate receptor - transporter expression and spontaneous seizures in rats exposed to methylazoxymethanol in utero. *Epilepsia* 48:158-168.
- Hauser WA, Hesdorffer DC (1990) *Epilepsy: Frequency, Causes and Consequences*. Demos Medical Pub.
- Hefti BJ, Smith PH (2000) Anatomy, physiology, and synaptic responses of rat layer V auditory cortical cells and effects of intracellular GABA(A) blockade. *J Neurophysiol* 83:2626-2638.
- Hesse W, Möller E, Arnold M, Schack B (2003) The use of time-variant EEG Granger causality for inspecting directed interdependencies of neural assemblies. *J Neurosci Methods* 124:27-44.
- Heuschkel MO, Fejtli M, Raggenbass M, Bertrand D, Renaud P (2002) A three-dimensional multi-electrode array for multi-site stimulation and recording in acute brain slices. *J Neurosci Methods* 114:135-148.
- Hicks SP, D'AMATO CJ, LOWE MJ (1959) The development of the mammalian nervous system. I. Malformations of the brain, especially the cerebral cortex, induced in rats by radiation. II. Some mechanisms of the malformations of the cortex. *J Comp Neurol* 113:435-469.
- Hirtz D, Thurman DJ, Gwinn-Hardy K, Mohamed M, Chaudhuri AR, Zalutsky R (2007) How common are the "common" neurologic disorders? *Neurology* 68:326-337.
- Hoffman SN, Prince DA (1995) Epileptogenesis in immature neocortical slices induced by 4-aminopyridine. *Brain Res Dev Brain Res* 85:64-70.
- Holmes GL, Sarkisian M, Ben-Ari Y, Liu Z, Chevassus-Au-Louis N (1999) Consequences of cortical dysplasia during development in rats. *Epilepsia* 40:537-544.

- Israel DA, Barry WH, Edell DJ, Mark RG (1984) An array of microelectrodes to stimulate and record from cardiac cells in culture. *Am J Physiol* 247:H669-H674.
- Jacobs KM, Gutnick MJ, Prince DA (1996) Hyperexcitability in a model of cortical maldevelopment. *Cereb Cortex* 6:514-523.
- Jacobs KM, Hwang BJ, Prince DA (1999a) Focal epileptogenesis in a rat model of polymicrogyria. *J Neurophysiol* 81:159-173.
- Jacobs KM, Kharazia VN, Prince DA (1999b) Mechanisms underlying epileptogenesis in cortical malformations. *Epilepsy Res* 36:165-188.
- Jensh RP, Brent RL (1987) The effect of low-level prenatal X-irradiation on postnatal development in the Wistar rat. *Proc Soc Exp Biol Med* 184:256-263.
- Jimbo Y, Robinson HP (2000) Propagation of spontaneous synchronized activity in cortical slice cultures recorded by planar electrode arrays. *Bioelectrochemistry* 51:107-115.
- Kandel ER, Schwartz JH, Jessell TM (2000) *Principles of Neural Science*. New York : McGraw-Hill, Health Professions Division.
- Kasper EM, Larkman AU, Lübke J, Blakemore C (1994) Pyramidal neurons in layer 5 of the rat visual cortex. I. Correlation among cell morphology, intrinsic electrophysiological properties, and axon targets. *J Comp Neurol* 339:459-474.
- Kato M, Kimura T, Lin C, Ito A, Kodama S, Morikawa T, Soga T, Hayasaka K (1999) A novel mutation of the doublecortin gene in Japanese patients with X-linked lissencephaly and subcortical band heterotopia. *Hum Genet* 104:341-344.
- Kellinghaus C, Kunieda T, Ying Z, Pan A, Lüders HO, Najm IM (2004) Severity of histopathologic abnormalities and in vivo epileptogenicity in the in utero radiation model of rats is dose dependent. *Epilepsia* 45:583-591.
- Kellinghaus C, Möddel G, Shigeto H, Ying Z, Jacobsson B, Gonzalez-Martinez J, Burrier C, Janigro D, Najm IM (2007) Dissociation between in vitro and in vivo epileptogenicity in a rat model of cortical dysplasia. *Epileptic Disord* 9:11-19.
- Kettenmann H (1999) Physiology of glial cells. *Adv Neurol* 79:565-571.
- Kleinfeld D, Delaney KR (1996) Distributed representation of vibrissa movement in the upper layers of somatosensory cortex revealed with voltage-sensitive dyes. *J Comp Neurol* 375:89-108.
- Kondo S, Najm I, Kunieda T, Perryman S, Yacubova K, Lüders HO (2001) Electroencephalographic characterization of an adult rat model of radiation-induced cortical dysplasia. *Epilepsia* 42:1221-1227.

- Krsek P, Maton B, Jayakar P, Dean P, Korman B, Rey G, Dunoyer C, Pacheco-Jacome E, Morrison G, Ragheb J, Vinters HV, Resnick T, Duchowny M (2009) Incomplete resection of focal cortical dysplasia is the main predictor of poor postsurgical outcome. *Neurology* 72:217-223.
- Kwan P, Brodie MJ (2000) Early identification of refractory epilepsy. *N Engl J Med* 342:314-319.
- Larkman A, Mason A (1990) Correlations between morphology and electrophysiology of pyramidal neurons in slices of rat visual cortex. I. Establishment of cell classes. *J Neurosci* 10:1407-1414.
- Lee KS, Schottler F, Collins JL, Lanzino G, Couture D, Rao A, Hiramatsu K, Goto Y, Hong SC, Caner H, Yamamoto H, Chen ZF, Bertram E, Berr S, Omary R, Scrable H, Jackson T, Goble J, Eisenman L (1997) A genetic animal model of human neocortical heterotopia associated with seizures. *J Neurosci* 17:6236-6242.
- Lee WL, Hablitz JJ (1991) Initiation of epileptiform activity by excitatory amino acid receptors in the disinhibited rat neocortex. *J Neurophysiol* 65:87-95.
- Lehohla M, Russell V, Kellaway L, Govender A (2000) Development of a method to evaluate glutamate receptor function in rat barrel cortex slices. *Metab Brain Dis* 15:305-314.
- Leppik IE (1992) Intractable Epilepsy in Adults. In: *Surgical Treatment of Epilepsy* (Theodore WH, eds), pp7-11. Amsterdam: Elsevier.
- Leventer RJ, Guerrini R, Dobyns WB (2008) Malformations of cortical development and epilepsy. *Dialogues Clin Neurosci* 10:47-62.
- Leventer RJ, Phelan EM, Coleman LT, Kean MJ, Jackson GD, Harvey AS (1999) Clinical and imaging features of cortical malformations in childhood. *Neurology* 53:715-722.
- Lin DD, Roper SN (2006) In Utero Irradiation as a Model of Cortical Dysplasia. In: *Models of Seizure and Epilepsy* (Pitkänen A, Schwartzkroin PA, Moshé SL, eds), pp315-321. Burlington, MA: Elsevier Academic Press.
- Lombroso CT (2000) Can early postnatal closed head injury induce cortical dysplasia. *Epilepsia* 41:245-253.
- Lopantsev V, Avoli M (1998) Laminar organization of epileptiform discharges in the rat entorhinal cortex in vitro. *J Physiol* 509 (Pt 3):785-796.
- Lynch JC (1997) The Cerebral Cortex. In: *Fundamental Neuroscience* (Haines DE, eds), pp455-470. Singapore: Churchill Livingstone Inc.

- Marín-Padilla M, Tsai RJ, King MA, Roper SN (2003) Altered corticogenesis and neuronal morphology in irradiation-induced cortical dysplasia: a Golgi-Cox study. *J Neuropathol Exp Neurol* 62:1129-1143.
- Marret S, Mukendi R, Gadisseux JF, Gressens P, Evrard P (1995) Effect of ibotenate on brain development: an excitotoxic mouse model of microgyria and posthypoxic-like lesions. *J Neuropathol Exp Neurol* 54:358-370.
- McCormick DA, Connors BW, Lighthall JW, Prince DA (1985) Comparative electrophysiology of pyramidal and sparsely spiny stellate neurons of the neocortex. *J Neurophysiol* 54:782-806.
- McGrath JJ, Riggs HE, SCHWARZ HP (1956) Malformation of the adult brain (albino rat) resulting from prenatal irradiation. *J Neuropathol Exp Neurol* 15:432-46; discussion, 446-7.
- McIntyre DC (2006) The Kindling Phenomenon. In: *Models of Seizure and Epilepsy* (Pitkänen A, Schwartzkroin PA, Moshé SL, eds), pp351-363. Burlington, MA: Elsevier Academic Press.
- McNamara JO, Huang YZ, Leonard AS (2006) Molecular signaling mechanisms underlying epileptogenesis. *Sci STKE* 2006:re12.
- Meencke HJ, Veith G (1992) Migration disturbances in epilepsy. *Epilepsy Res Suppl* 9:31-9; discussion 39-40.
- Meierkord H, Schuchmann S, Buchheim K, Heinemann U (1997) Optical imaging of low Mg(2+)-induced spontaneous epileptiform activity in combined rat entorhinal cortex-hippocampal slices. *Neuroreport* 8:1857-1861.
- Meister M, Pine J, Baylor DA (1994) Multi-neuronal signals from the retina: acquisition and analysis. *J Neurosci Methods* 51:95-106.
- Miki T, Sawada K, Sun XZ, Hisano S, Takeuchi Y, Fukui Y (1999) Abnormal distribution of hippocampal mossy fibers in rats exposed to X-irradiation in utero. *Brain Res Dev Brain Res* 112:275-280.
- Miles R, Wong RK, Traub RD (1984) Synchronized afterdischarges in the hippocampus: contribution of local synaptic interactions. *Neuroscience* 12:1179-1189.
- Mischel PS, Nguyen LP, Vinters HV (1995) Cerebral cortical dysplasia associated with pediatric epilepsy. Review of neuropathologic features and proposal for a grading system. *J Neuropathol Exp Neurol* 54:137-153.
- (2006) *Models of Seizure and Epilepsy* (Pitkänen A, Schwartzkroin PA, Moshé SL, eds). Burlington, MA: Isevier Academic Press.

- Mody I, Schwartzkroin PA (1997) Acute Seizure Models (intact animals). In: *Epilepsy: A Comprehensive Textbook* (Engel J, Pedley TA, eds), pp397-404. Philadelphia, PA: Lippincott-Raven.
- Momose-Sato Y, Sato K, Sakai T, Hirota A, Matsutani K, Kamino K (1995) Evaluation of optimal voltage-sensitive dyes for optical monitoring of embryonic neural activity. *J Membr Biol* 144:167-176.
- Mosewich RK, So EL, O'Brien TJ, Cascino GD, Sharbrough FW, Marsh WR, Meyer FB, Jack CR, O'Brien PC (2000) Factors predictive of the outcome of frontal lobe epilepsy surgery. *Epilepsia* 41:843-849.
- Mountcastle VB (1978) An Organizing Principle for Cerebral Function. In: *The Mindful Brain* (Edelman GM, Mountcastle VB, eds), pp7-50. Cambridge MA: MIT Press.
- Möddel G, Jacobson B, Ying Z, Janigro D, Bingaman W, González-Martínez J, Kellinghaus C, Prayson RA, Najm IM (2005) The NMDA receptor NR2B subunit contributes to epileptogenesis in human cortical dysplasia. *Brain Res* 1046:10-23.
- Najm IM, Tilelli CQ, Oghlakan R (2007) Pathophysiological mechanisms of focal cortical dysplasia: a critical review of human tissue studies and animal models. *Epilepsia* 48 Suppl 2:21-32.
- Natarajan A, Molnar P, Sieverdes K, Jamshidi A, Hickman JJ (2006) Microelectrode array recordings of cardiac action potentials as a high throughput method to evaluate pesticide toxicity. *Toxicol In Vitro* 20:375-381.
- Nieuwenhuys R, Voogd J, van Huijzen C (2008) In: *The Human Central Nervous System*, pp491-679. New York: Springer.
- Noebels JL, Prince DA (1978) Development of focal seizures in cerebral cortex: role of axon terminal bursting. *J Neurophysiol* 41:1267-1281.
- Novak JL, Wheeler BC (1988) Multisite hippocampal slice recording and stimulation using a 32 element microelectrode array. *J Neurosci Methods* 23:149-159.
- Oka H, Shimono K, Ogawa R, Sugihara H, Taketani M (1999) A new planar multielectrode array for extracellular recording: application to hippocampal acute slice. *J Neurosci Methods* 93:61-67.
- Palmini A, Andermann E, Andermann F (1994) Prenatal events and genetic factors in epileptic patients with neuronal migration disorders. *Epilepsia* 35:965-973.
- Paxinos G (2004) *The Rat Nervous System*. San Diego, CA: Academic Press.
- Paxinos G, Kus L, Ashwell KWS, Watson C (1999) *Chemoarchitectonic Atlas of The Rat Forebrain*. San Diego, CA: Academic Press.

- Paxinos G, Watson C (1997) *The Rat Brain in Stereotaxic Coordinates*. San Diego, CA: Academic Press.
- Petersen CC, Grinvald A, Sakmann B (2003) Spatiotemporal dynamics of sensory responses in layer 2/3 of rat barrel cortex measured in vivo by voltage-sensitive dye imaging combined with whole-cell voltage recordings and neuron reconstructions. *J Neurosci* 23:1298-1309.
- Pine J (1980) Recording action potentials from cultured neurons with extracellular microcircuit electrodes. *J Neurosci Methods* 2:19-31.
- Pinto DJ, Patrick SL, Huang WC, Connors BW (2005) Initiation, propagation, and termination of epileptiform activity in rodent neocortex in vitro involve distinct mechanisms. *J Neurosci* 25:8131-8140.
- Rakic P (1972) Mode of cell migration to the superficial layers of fetal monkey neocortex. *J Comp Neurol* 145:61-83.
- Rakic P (1988) Specification of cerebral cortical areas. *Science* 241:170-176.
- Redecker C, Hagemann G, Köhling R, Straub H, Witte OW, Speckmann EJ (2005) Optical imaging of epileptiform activity in experimentally induced cortical malformations. *Exp Neurol* 192:288-298.
- Redecker C, Hagemann G, Witte OW, Marret S, Evrard P, Gressens P (1998a) Long-term evolution of excitotoxic cortical dysgenesis induced in the developing rat brain. *Brain Res Dev Brain Res* 109:109-113.
- Redecker C, Lutzenburg M, Gressens P, Evrard P, Witte OW, Hagemann G (1998b) Excitability changes and glucose metabolism in experimentally induced focal cortical dysplasias. *Cereb Cortex* 8:623-634.
- Roebroeck A, Formisano E, Goebel R (2005) Mapping directed influence over the brain using Granger causality and fMRI. *Neuroimage* 25:230-242.
- Roebroeck A, Formisano E, Goebel R (2009) The identification of interacting networks in the brain using fMRI: Model selection, causality and deconvolution. *Neuroimage*.
- Roper SN (1998) In utero irradiation of rats as a model of human cerebrocortical dysgenesis: a review. *Epilepsy Res* 32:63-74.
- Roper SN, Abraham LA, Streit WJ (1997) Exposure to in utero irradiation produces disruption of radial glia in rats. *Dev Neurosci* 19:521-528.
- Roper SN, Eisenschenk S, King MA (1999) Reduced density of parvalbumin- and calbindin D28-immunoreactive neurons in experimental cortical dysplasia. *Epilepsy Res* 37:63-71.

- Roper SN, Gilmore RL, Houser CR (1995) Experimentally induced disorders of neuronal migration produce an increased propensity for electrographic seizures in rats. *Epilepsy Res* 21:205-219.
- Roper SN, King MA, Abraham LA, Boillot MA (1997) Disinhibited in vitro neocortical slices containing experimentally induced cortical dysplasia demonstrate hyperexcitability. *Epilepsy Res* 26:443-449.
- Rothermel A, Nieber M, Müller J, Wolf P, Schmidt M, Robitzki AA (2006) Real-time measurement of PMA-induced cellular alterations by microelectrode array-based impedance spectroscopy. *Biotechniques* 41:445-450.
- Sarkisian MR (2001) Overview of the Current Animal Models for Human Seizure and Epileptic Disorders. *Epilepsy Behav* 2:201-216.
- Sarnat HB (1987) Disturbances of late neuronal migrations in the perinatal period. *Am J Dis Child* 141:969-980.
- Schousboe A (2003) Role of astrocytes in the maintenance and modulation of glutamatergic and GABAergic neurotransmission. *Neurochem Res* 28:347-352.
- Schubert D, Staiger JF, Cho N, Kötter R, Zilles K, Luhmann HJ (2001) Layer-specific intracolumnar and transcolumnar functional connectivity of layer V pyramidal cells in rat barrel cortex. *J Neurosci* 21:3580-3592.
- Schwartzkroin PA, Walsh CA (2000) Cortical malformations and epilepsy. *Ment Retard Dev Disabil Res Rev* 6:268-280.
- Scott RA, Lhatoo SD, Sander JW (2001) The treatment of epilepsy in developing countries: where do we go from here? *Bull World Health Organ* 79:344-351.
- Seino M, Williamson PD, Inoue Y, Mihara T, Matsuda K, Tottori T (2000) Classification of Neocortical Epilepsies. In: *Neocortical Epilepsies* (Williamson PD, Siegel AM, Roberts DW, Thadani VM, Gazzaniga MS, eds), pp125-139. Philadelphia, PA: Lippincott Williams & Wilkins.
- Shepherd GM, Koch C (1998) Introduction to Synaptic Circuits. In: *The Synaptic Organization of the Brain* (Shepherd, eds), pp1-36. New York, NY: Oxford University Press.
- Silva LR, Amitai Y, Connors BW (1991) Intrinsic oscillations of neocortex generated by layer 5 pyramidal neurons. *Science* 251:432-435.
- Sisodiya SM (2000) Surgery for malformations of cortical development causing epilepsy. *Brain* 123 (Pt 6):1075-1091.

- Slutzky MW, Cvitanovic P, Mogul DJ (2003) Manipulating epileptiform bursting in the rat hippocampus using chaos control and adaptive techniques. *IEEE Trans Biomed Eng* 50:559-570.
- Slutzky MW, Cvitanović P, Mogul DJ (2001) Deterministic chaos and noise in three in vitro hippocampal models of epilepsy. *Ann Biomed Eng* 29:607-618.
- Steriade M, McCormick DA, Sejnowski TJ (1993) Thalamocortical oscillations in the sleeping and aroused brain. *Science* 262:679-685.
- Stett A, Barth W, Weiss S, Haemmerle H, Zrenner E (2000) Electrical multisite stimulation of the isolated chicken retina. *Vision Res* 40:1785-1795.
- Swanson LW (1998) *Brain Maps: Structure of the Rat Brain*. New York, NY: Elsevier.
- Tanifuji M, Sugiyama T, Murase K (1994) Horizontal propagation of excitation in rat visual cortical slices revealed by optical imaging. *Science* 266:1057-1059.
- Taylor DC, Falconer MA, Bruton CJ, Corsellis JA (1971) Focal dysplasia of the cerebral cortex in epilepsy. *J Neurol Neurosurg Psychiatry* 34:369-387.
- Telfeian AE, Connors BW (1998) Layer-specific pathways for the horizontal propagation of epileptiform discharges in neocortex. *Epilepsia* 39:700-708.
- Telfeian AE, Connors BW (1999) Epileptiform propagation patterns mediated by NMDA and non-NMDA receptors in rat neocortex. *Epilepsia* 40:1499-1506.
- Thomas CA (1972) A miniature microelectrode array to monitor the bioelectric activity of cultured cells. *Exp. Cell Res.* 74:61-66.
- Traub RD, Miles R, Jefferys JG (1993) Synaptic and intrinsic conductances shape picrotoxin-induced synchronized after-discharges in the guinea-pig hippocampal slice. *J Physiol* 461:525-547.
- Trevelyan AJ, Yuste R (2009) In: *Animal Models of Epilepsy* (Baraban SC, eds), pp141-161. New York, NY: Humana Press.
- Tsau Y, Guan L, Wu JY (1998) Initiation of spontaneous epileptiform activity in the neocortical slice. *J Neurophysiol* 80:978-982.
- Tsau Y, Guan L, Wu JY (1999) Epileptiform activity can be initiated in various neocortical layers: an optical imaging study. *J Neurophysiol* 82:1965-1973.
- van Brederode JF, Spain WJ (1995) Differences in inhibitory synaptic input between layer II-III and layer V neurons of the cat neocortex. *J Neurophysiol* 74:1149-1166.

- van Putten MJ, van Putten MH (2007) Discovery of recurrent multiple brain states in non-convulsive status epilepticus. *Clin Neurophysiol* 118:2798-2804.
- Wadman WJ, Gutnick MJ (1993) Non-uniform propagation of epileptiform discharge in brain slices of rat neocortex. *Neuroscience* 52:255-262.
- Wagenaar DA, Madhavan R, Pine J, Potter SM (2005) Controlling bursting in cortical cultures with closed-loop multi-electrode stimulation. *J Neurosci* 25:680-688.
- Walsh CA (1999) Genetic malformations of the human cerebral cortex. *Neuron* 23:19-29.
- Wenzel HJ, Robbins CA, Tsai LH, Schwartzkroin PA (2001) Abnormal morphological and functional organization of the hippocampus in a p35 mutant model of cortical dysplasia associated with spontaneous seizures. *J Neurosci* 21:983-998.
- Wiener N (1956) The theory of prediction. In: *Modern Mathematics for the engineer* (Beckenback EF, eds). New York: McGraw-Hill.
- Williams SR, Stuart GJ (1999) Mechanisms and consequences of action potential burst firing in rat neocortical pyramidal neurons. *J Physiol* 521 Pt 2:467-482.
- Wolf P, Rothermel A, Beck-Sickingler AG, Robitzki AA (2008) Microelectrode chip based real time monitoring of vital MCF-7 mamma carcinoma cells by impedance spectroscopy. *Biosens Bioelectron* 24:253-259.
- Wong M (2009) Mammalian target of rapamycin (mTOR) inhibition as a potential antiepileptogenic therapy: From tuberous sclerosis to common acquired epilepsies. *Epilepsia*.
- Wong RO, Meister M, Shatz CJ (1993) Transient period of correlated bursting activity during development of the mammalian retina. *Neuron* 11:923-938.
- Woolsey TA, Van der Loos H (1970) The structural organization of layer IV in the somatosensory region (SI) of mouse cerebral cortex. The description of a cortical field composed of discrete cytoarchitectonic units. *Brain Res* 17:205-242.
- Wu JY, Falk CX, Cohen L, Tsau Y, Zecevic D (1993) Optical measurement of action potential activity in invertebrate ganglia. *Jpn J Physiol* 43 Suppl 1:S21-S29.
- Wu JY, Guan L, Bai L, Yang Q (2001) Spatiotemporal properties of an evoked population activity in rat sensory cortical slices. *J Neurophysiol* 86:2461-2474.
- Xiang H, Chen HX, Yu XX, King MA, Roper SN (2006) Reduced excitatory drive in interneurons in an animal model of cortical dysplasia. *J Neurophysiol* 96:569-578.

- Yang L, Benardo LS (1997) Epileptogenesis following neocortical trauma from two sources of disinhibition. *J Neurophysiol* 78:2804-2810.
- Yang L, Benardo LS (2000) Valproate prevents epileptiform activity after trauma in an in vitro model in neocortical slices. *Epilepsia* 41:1507-1513.
- Yang L, Benardo LS (2002) Laminar properties of 4-aminopyridine-induced synchronous network activities in rat neocortex. *Neuroscience* 111:303-313.
- Yang Y, Tandon P, Liu Z, Sarkisian MR, Stafstrom CE, Holmes GL (1998) Synaptic reorganization following kainic acid-induced seizures during development. *Brain Res Dev Brain Res* 107:169-177.
- Yuste R, Katz LC (1991) Control of postsynaptic Ca²⁺ influx in developing neocortex by excitatory and inhibitory neurotransmitters. *Neuron* 6:333-344.
- Zhou FW, Chen HX, Roper SN (2009) Balance of inhibitory and excitatory synaptic activity is altered in fast-spiking interneurons in experimental cortical dysplasia. *J Neurophysiol* 102:2514-2525.
- Zhu WJ, Roper SN (2000) Reduced inhibition in an animal model of cortical dysplasia. *J Neurosci* 20:8925-8931.
- Zilles K (1985) *The Cortex of the Rat*. Berlin: Springer-Verlag.

BIOGRAPHICAL SKETCH

Born in Pensacola, Florida, John Nicholas Grimes moved to Crestview, Florida when he was adopted at 5 months of age into a home by his loving family: parents, Tom and LeViniua; brother, Ricky; and sister, Vicki. Grimes graduated from Crestview High School in 1999 and moved to Gainesville, Florida to attend the University of Florida where he graduated cum laude with a Bachelor of Science in Computer Engineering in 2004. After a stint working for the United States Department of Defense, he enrolled in graduate school to pursue a Ph.D. in Biomedical Engineering, also at the University of Florida. Grimes received his Master of Engineering in 2009 and his Ph.D. in 2011.